Simulation of a solar-assisted $LiBr/H_2O$ cooling system

by

Bagas Wardono

A Thesis Submitted to the

Graduate Faculty in Partial Fulfillment of the

Requirements for the Degree of

MASTER OF SCIENCE

Department: Mechanical Engineering
Major: Mechanical Engineering

Iowa State University
Ames, Iowa
1994

TABLE OF CONTENTS

LIST OF TABLES

LIST OF FIGURES

NOMENCLATURE

AR	heat exchanger area, m^2.
Ac	collector area, m^2.
COP	Coefficient of Performance.
CR	capacity ratio of heat exchangers.
C_{ref}	cost of the known equipment, \$.
Cap	capacity of the desired equipment, m^2.
Cap_{ref}	capacity of the known equipment, m^2.
Cp	specific heat, J/ kg K.
Cp_s	specific heat of storage tank working fluid, J/ kg K.
D	tube outside diameter, m.
D_R	daily temperature range, ^{o} C.
F_R	collector heat removal factor.
F'_R	modified collector heat removal factor accounts for the presence of the heat exchanger.
F_S	fraction of solar energy contribution in supplying energy to the cooling system.
HR	hour (in 24-hour basis).
HX_{cost}	initial cost of the cooling system, \$.

I	price indices of the desired equipment.
I_T	total solar radiation on the tilted surface, J/m^2 hr.
I_{ref}	price indices of the known equipment.
L	storage tank load, W.
Ln	nominal capacity of the cooling machine, ton.
M_T	storage tank capacity, kg.
N	Number of tubes.
NTU	Number of Transfer Unit.
Nu	Nusselt number.
Nu_l	Nusselt number for laminar flow.
Nu_t	Nusselt number for turbulent flow.
Opr_{cost}	operating cost of the cooling system, \$.
P	operating pressure, Pa.
P_S	standard atmospheric pressure, Pa.
Pr	Prandtl number.
Q_c	heat rejected from the condenser, W.
Q_e	cooling load, W.
Q_s	heat input to Carnot cooling cycle, W.
Q_u	useful energy received by the collector, W.
Q_{1g}	heat input to the first-stage generator, W.
Q_{2g}	heat recovery in the second-stage generator, W.
R_i	tube inner radius, m.
R_o	tube outer radius, m.
Re	Reynolds number.
Re_{tr}	transition Reynolds number.

T	temperature, ^{o} C.
T_C	cooling effect temperature at Carnot cooling cycle, ^{o} C.
T_H	heat supply temperature to Carnot cycle, ^{o} C.
T_0	heat rejection temperature from Carnot cooling system, ^{o} C.
T_a	ambient temperature, ^{o} C.
T_i	inlet temperature to the collector, ^{o} C.
T_o	outlet temperature from the collector, ^{o} C.
T_r	modified temperature incorporating subcooling effect, ^{o} C.
T_s	storage tank temperature at time t, ^{o} C.
T_s^+	storage tank temperature at time $t + \Delta t$, ^{o} C.
T_{sat}	saturated liquid temperature, ^{o} C.
T_w	tube wall temperature, ^{o} C.
T_{ave}	monthly average temperature, ^{o} C.
T_{room}	room temperature, ^{o} C.
UA	total heat transfer coefficient, W/K.
UA_{loss}	total heat transfer coefficient from the storage tank, W/K.
U_L	total heat transfer coefficient from the collector, W/K.
XW	LiBr/H_2O solution mass fraction.
f	friction factor inside the tube.
fr	hourly fraction of cooling demand.
g	gravitational acceleration, m/s^2.
h	enthalpy, J/kg.
h_f	enthalpy of liquid, J/kg.
h_g	enthalpy of vapor, J/kg.
h_{fg}	$h_g - h_f$, J/kg

hc_i convective coefficient inside the tube, W/m^2 K.

hc_o convective coefficient outside the tube, W/m^2 K.

k thermal conductivity, W/m K.

k_l thermal conductivity of liquid, W/m K.

kt sky clearness index.

$\dot{m}$ mass-flow rate, kg/s.

$\dot{m}_c$ collector mass-flow rate, kg/s.

q heat flux, W/m^2.

Ψ Wilkinson's degradation factor.

β slope of the collector, ^{o}.

ℓ tube length, m.

ϵ heat exchanger effectiveness.

η efficiency.

μ_l dynamic viscosity of liquid, kg/m s.

ν_l kinematic viscosity of liquid, m^2/s.

ϕ latitude, ^{o}.

ρ_g ground reflectance.

ρ_l specific weight of liquid, kg/m^3.

ρ_v specific weight of vapor, kg/m^3.

τ_l surface tension of liquid, N/m.

$(\tau\alpha)$ effective transmittance-absorptance product.

CHAPTER 1. INTRODUCTION

Basic Concept

The main energy sources for cooling systems are electricity or natural gas. But the increasing demand for air conditioning and the increasing cost of current energy sources have opened the possibility of using alternative energy sources. Over the past few years, solar energy has received increased interest as an alternative energy source for driving cooling systems. This is based on the fact that the need for energy to drive cooling systems usually occurs when solar energy is most available. The utilization of solar energy promises to reduce the energy use and peak demand on conventional energy sources.

Solar-powered cooling implies the utilization of solar energy through several mechanical components to produce a cooling effect (Figure 1.1). The solar energy flows from the sun to a solar collector where the energy is transferred to a flowing fluid, which is then stored in a hot storage reservoir. A cooling cycle uses this stored energy to produce a cooling effect by removing heat from the cold storage reservoir. The resulting energy is rejected through a heat rejector. It is to be recognized that solar energy utilization occurs only when the sun is radiating energy to the solar collector. Auxiliary heat from conventional energy sources is provided to supply energy to the cooling system when the solar energy storage is depleted.

Several types of solar systems are available for air conditioning applications. Figure 1.1 shows both the hot and cold storage reservoirs. But air conditioning systems usually involve only the sensible hot storage reservoir. The waste energy is usually rejected to the environment using a cooling tower. In some cooling systems, this heat rejection is accomplished in a condenser which is a part of the cooling cycle.

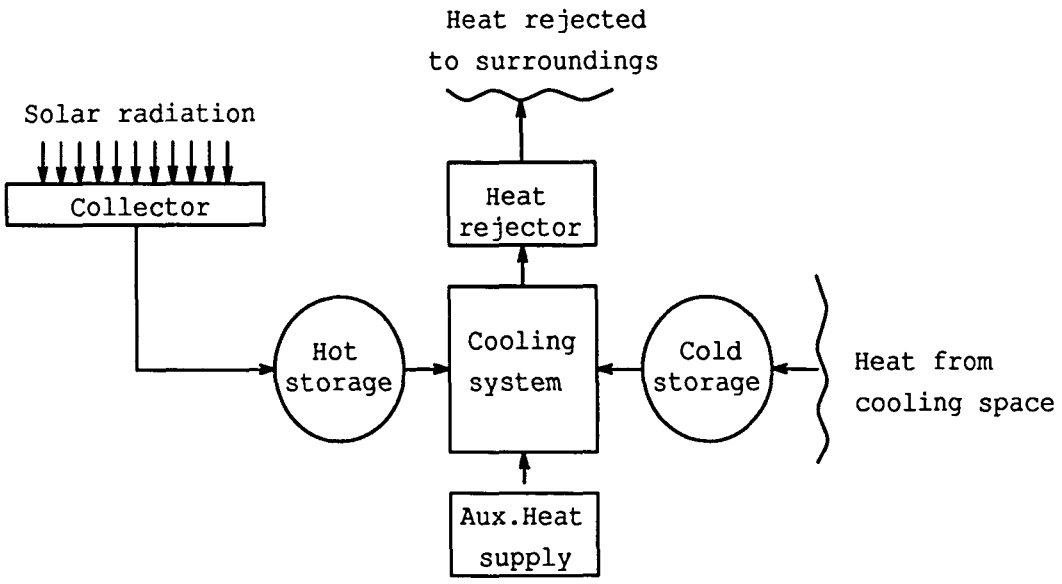

Figure 1.1: Heat flow diagram for solar cooling system.

The main technologies to utilize solar energy for cooling include vapor compression, photovoltaic, desiccant, and absorption cooling systems. Each of these systems will be discussed later in this chapter.

Theoretically, the maximum performance of any thermodynamic machine can be measured by applying the second law of thermodynamics. This law states that it is impossible to have heat flowing from a cold reservoir to a hot reservoir without

work being done on the system. When this law is applied to a cooling system, the result is a reversed Carnot cycle (Figure 1.2). The heat is supplied to the engine at temperature T_H, and the energy is rejected to the environment at temperature T_0. The cooling effect is at temperature T_C. The Coefficient of Performance (COP) of the Carnot cycle is defined as the ratio of the cooling effect (Q_e) to the heat supplied to the cooling engine (Q_s). When a Kelvin scale temperature is applied, the COP of the Carnot cooling system might be represented as

$$COP_{Carnot} = \frac{1 - \frac{T_0}{T_H}}{\frac{T_0}{T_C} - 1} \tag{1.1}$$

Figure 1.3 shows the performance of the Carnot cycle as a function of heat source temperature at given cooling and heat rejection temperatures. From the definition of Carnot COP, it can be seen that the performance of the Carnot cooling engine can be improved by increasing the temperature of the hot and cold reservoirs or by decreasing the heat rejection temperature. In general, the performance of a cooling system is also affected by the effectiveness of a component in transferring heat to other components. This involves the effectiveness of the solar collector as the first component to capture the solar energy.

Vapor Compression Cooling Systems

Solar-powered vapor compression systems use a Rankine heat engine cycle to generate mechanical work. In the Rankine engine, the solar collector supplies heat to a boiler to generate vapor from the compressed liquid. The high-pressure vapor

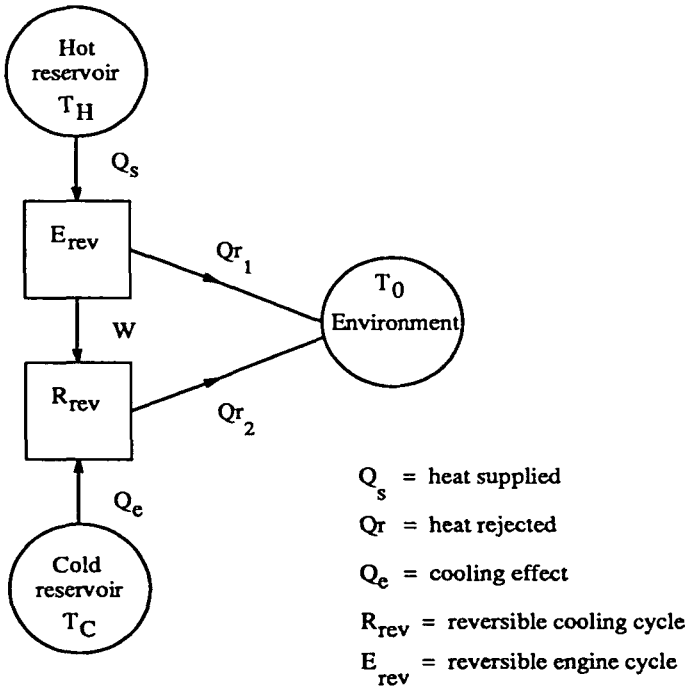

Figure 1.2: Schematic diagram of a possible Carnot cooling system.

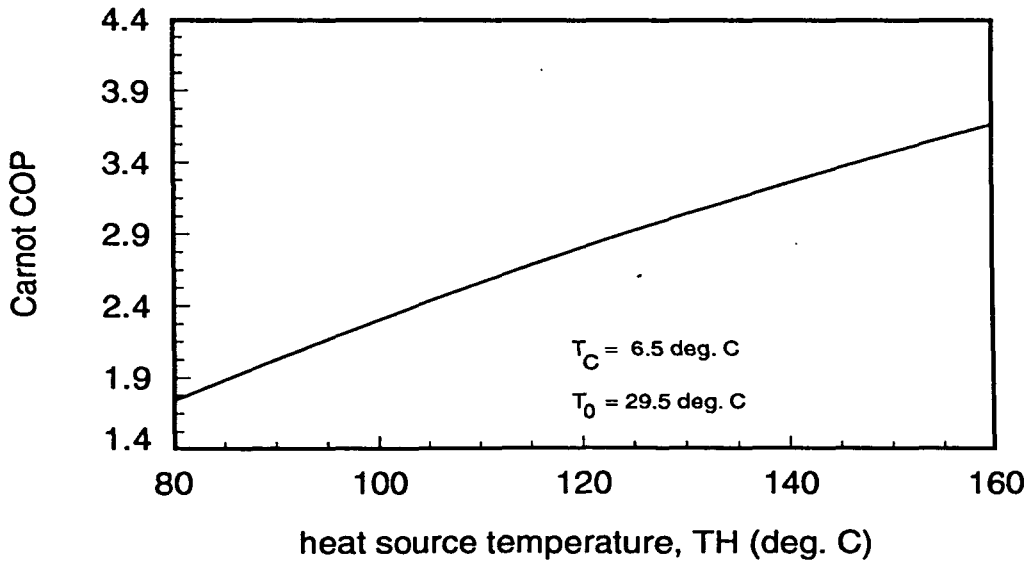

Figure 1.3: Performance of Carnot cooling system.

is then expanded in a turbine, and mechanical work is produced. Cooling water is used to condense the wet vapor so it can be used again through pumping to the boiler. The mechanical work output of the Rankine cycle is then used either directly or through an intermediate electric motor to drive the cooling system compressor.

Typically, vapor compression air conditioning has a maximum COP of approximately 4.5 [1] and a solar Rankine power cyle has an efficiency less than 6 % [2]. Based on these numbers, the COP of a solar-assisted vapor compression cooling system can be estimated to be around 0.28. This prediction agrees with the experimental results of R. E. Barber as cited in Reference [3]. This system was designed for 3 tons of capacity and used for space cooling. The Rankine cycle used R-113 as the working fluid, and the energy input to the Rankine cycle was supplied by solar-heated water. The mechanical work output, with a generator, was used to drive the electric motor of a vapor compression cooling system. When cooling water at 29.5^o C and various hot water supply temperatures between 76 to 100^o C were used, the system's COPs were between 0.25 to 0.5. The main reason for this relatively low COP is that vapor compression systems use more equipment than other systems, therefore there are more energy conversion processes involved. In this context, the efficiency of each component has an important role for the utilization of solar energy.

Photovoltaic Cooling Systems

Photovoltaic cooling systems use solar-generated electricity to run a vapor-compression system. In these systems, photovoltaic arrays capture the solar flux and convert it to direct-current (DC) electricity to charge a battery. The battery is then used to drive a DC compressor motor in a vapor compression cooling system.

The performance of a photovoltaic system is greatly influenced by the efficiency of photovoltaic arrays in converting the solar energy to electricity. Various available photovoltaic technologies typically have efficiencies in the range of 11-15 % [4].

Desiccant Cooling Systems

Desiccants have the potential to absorb water without chemical reactions. This potential is decreased as the desiccant absorbs more water. To regenerate its potential, a process requiring external energy is used to drive out the water in the desiccant so it can be recirculated and used to absorb more water vapor. In this context, solar energy may be used to regenerate the desiccant.

A liquid desiccant cooling system first dehumidifies warm, humid air by spraying a strong (dry) solution desiccant into the air and absorbing water vapor from the flowing air. This process is exothermic, so a cooling fluid is required to maintain the dehumidifier temperature, which in turn also maintains the absorption potential of the desiccant. The result is dry, warm air that can be spray cooled. From the dehumidifier, the desiccant is then recirculated to a solar-powered regenerator. This regenerator may use either a direct or an indirect regeneration process. A direct regeneration process puts the weak (wet) solution desiccant into direct contact with the solar heat source, while an indirect regeneration process requires another fluid to receive the solar heat and then transfer it to the weak solution desiccant.

A solid desiccant cooling system uses a porous rotating desiccant wheel as the dehumidifier. This rotating wheel is divided into two parts. In one part, the warm, humid air is passed through the wheel and dehumidified before being spray cooled. Through the other part of the wheel, regenerative air from a solar collector is passed

in the opposite direction to desorb the water vapor in the desiccant wheel so it can be used again for dehumidification.

A computer simulation to predict the performance of two liquid desiccant cooling systems, using solar energy as the external heat input, has been carried out [5]. Performance comparisons between direct and indirect systems show that under the same operating conditions, the direct regeneration process gives higher COPs in the range of 0.5. The COP of both systems increases with decreasing cooling water temperature. This agrees with the nature of desiccants to have larger absorption capacities at lower temperatures. The direct regenerative system has higher COPs than the indirect system. This is a result of the greater losses that occur in the indirect system because the desiccant is not in direct contact with the heat source.

Absorption System Configuration

Common absorption systems use either single- or double-stage cycles. The main components of a double-stage absorption cycle include the first-stage generator, the second-stage generator, an evaporator, an absorber, expansion orifices, a solution pump, and two recovery heat exchangers. This system is an enhancement of a single-stage system which utilizes only one generator and one recovery heat exchanger. The working fluid for absorption systems is a solution of refrigerant and absorbent. The most commonly used working fluids are $LiBr/H_2O$ and NH_3/H_2O pairs. The principal advantage of an absorption system over the more common vapor compression system is that the pressure is increased by a liquid pump that requires only a small fraction of the electrical energy required by a vapor compression system.

Literature Review of Absorption System Performance

The COP of an absorption cooling system is indicated by the ratio of the cooling capacity generated in the evaporator to the external heat input to the generator. Double-stage absorption systems using $LiBr/H_2O$ have been studied by several investigators [6, 7, 8, 9, 10]. For generator temperatures in the range of 300-400^o K, the COP of a double-stage absorption system varies from 1.2 to 1.6. This figure is about twice the single-stage generator performance. Simulations of double-stage systems using working fluids other than $LiBr/H_2O$ have also been done. When $LiCl/H_2O$ [10], H_2O-LiBr-LiSCn [9], and H_2O-LiCl-$CaCl_2$ $Zn(NO_3)_2$ (multi component salt) [6] are used as alternative working fluids, a double-effect system gives significantly higher COPs than a single-effect system.

Due to crystallization, there is a limitation on the generator temperatures that can be used with $LiBr/H_2O$. On the other hand, for multi-component salts, there is wider range of acceptable generator temperatures as crystallization is not a major problem. Although crystallization is not a major problem for NH_3/H_2O, it is not suitable for use as the working fluid in a double-stage system. The high temperature required in the first-stage generator is linked to the high condensation temperature of the refrigerant vapor in the second-stage generator. This high temperature is required to desorb the refrigerant from the solution in the second-stage generator. Thus, high pressures on the order of 75 atmospheres occur in the first-stage generator [11]. With these high temperatures and pressures, the critical point of ammonia is approached in the first-stage generator if NH_3/H_2O is being used as the working fluid.

A comparison of various absorption systems using $LiBr/H_2O$ and NH_3/H_2O can be seen in Table 1.1 [11]. In this table, the COP of a single-stage cycle using

NH_3/H_2O indicates a lower COP than that of the single-stage cycle using $LiBr/H_2O$. This is because, in the NH_3/H_2O cycle, the quality of the refrigerant leaving the generator is not pure refrigerant (NH_3): some fraction of the absorbent (H_2O) is also evaporated and flows together with the refrigerant. To avoid this problem, a rectifier condenser is utilized to decrease the fraction of absorbent that evaporates. Use of the rectifier condenser reduces the amount of refrigerant flowing to the evaporator and decreases the cooling effect. Furthermore, as mentioned earlier, a double-effect cooling system using NH_3/H_2O is not suitable for high pressure and temperature, thus the COP cannot be expected to have a competitive value compared to the COP of double-effect systems using $LiBr/H_2O$.

Table 1.1: Comparison of theoretical Coefficients of Performance [11].

Cycle	Evaporator temperature ^{o}C	Min. Heat rejection temperature ^{o}C	Max. Heat supply temperature ^{o}C	Theoretical COP
Single-stage $LiBr/H_2O$	5	30	77	0.81
Single-stage NH_3/H_2O	-10	30	94	0.45
Double-stage $LiBr/H_2O$	7.2	40.6	163	1.43
Double-stage NH_3/H_2O	7.13	30	94	1.06

Prediction of the Real Performance of a Double-Effect Absorption System

The performance of a real double-effect cycle is lower than that of an ideal cycle. Wilkinson [12] has introduced a degradation factor (Ψ) to help predict the real performance of a double-effect cycle.

Basically, a double-effect cycle is a combined construction of two separate cycles. One of these is a high-pressure cycle for which the heat input to the generator is obtained from the external solar heat source. This high-pressure cycle rejects heat to a condenser system, which provides the heat input to the generator of the low-pressure cycle. The COP of the high-pressure cycle (COP_{hi}) can be defined as the ratio of the cooling effect generated by the high-pressure cycle alone to the external heat input to the generator. Similarly, the COP of the low-pressure cycle (COP_{lo}) can be defined as the ratio of the cooling effect generated by the low-pressure cycle to the low-pressure cycle generator heat input (which is the heat rejected from the high-pressure cycle). For the combined construction, the COP is defined as the ratio of the combined cooling effect to the external heat input. The degradation factor (Ψ) is defined as the ratio of COP_{hi} to COP_{lo}. Using the above definitions, COP can then be expressed as

$$COP = COP_{lo}\left(\Psi + \frac{Q_{2g}}{Q_{1g}}\right) \tag{1.2}$$

To predict the real performance of a double-effect cycle, a knowledge of the applicable performance of a low-pressure cycle (COP_{lo}) and an optimum selection of the second-stage generator performance is very useful. Based on experience, Wilkinson [12] has suggested the degradation factor (Ψ) is about 0.85 to 0.95 and the ratio

of Q_{2g} to Q_{1g} is about 0.7. The COP_{lo} is within the range from 0.7 to 0.75. Thus, the COP of a double-effect cycle is typically in the range of 1.1 to 1.22.

Summary

Several technologies that can utilize solar energy as the main energy input for cooling systems have been presented. One consideration for the use of solar energy as the main energy input is the system COP. This is because a higher COP indicates lower collector areas for solar-assisted air conditioning. Among the technologies investigated, double-effect absorption cooling systems yield relatively high COPs. Also, the equipment needed for double-effect absorption cooling systems is much simpler than that required for vapor compression cooling systems.

The main focus of this study will be on the commonly used double-effect $LiBr/H_2O$ absorption cooling systems. The study of the performance of double-effect absorption systems will include assessing the effects of variations of available solar energy on the system performance. This will help predict the auxiliary energy input required from the utilities to drive the absorption system. The investigation of the double-effect $LiBr/H_2O$ absorption cooling system will also include the effects of heat exchanger areas and hot water, cooling water, and chilled water inlet temperatures on the system cost and performance. An optimization to determine the optimum heat transfer area for each heat exchanger which will give the minimum life cycle cost at nominal conditions was performed. To investigate the possibility of using solar energy as the main energy input, a collector model was developed and combined with the double-effect $LiBr/H_2O$ absorption cooling model. The study of the combined solar assisted cooling system includes the variation of solar energy contribution in supplying energy

throughout a one-year period.

CHAPTER 2. MODELING OF $LiBr/H_2O$ ABSORPTION COOLING SYSTEMS

System Modeling

A schematic diagram of a double-stage $LiBr/H_2O$ absorption cooling cycle is shown in Figure 2.1. The system includes heat exchangers, pump, valves, and piping. The first-stage generator receives input energy from a hot water source and generates superheated refrigerant steam (10). This steam condenses to a saturated liquid in the second-stage generator (11), which utilizes the heat of condensation to generate superheated refrigerant steam at a lower pressure (12). All of the refrigerant will then be condensed to a saturated liquid in the condenser utilizing cooling water output from the absorber (22). An expansion valve between the condenser and the evaporator is used to decrease the pressure of the refrigerant, which also decreases its temperature. This low temperature is used to cool the input chilled water (24) and produces low-pressure saturated steam (16). In the absorber, the steam is absorbed by the high concentration solution (9), so it can be pumped again to the first-stage generator. Two auxiliary heat exchangers are provided to utilize the heat from the high concentration solutions coming out of both generators (5,7).

The cooling water configuration as shown in Figure 2.1 is based on the standard configuration used by most commercial double-effect $LiBr/H_2O$ cooling systems. In

this study, different configurations of cooling water flows will be investigated. This includes both serial cooling water flowing from the condenser to absorber and parallel cooling water flow in which the condenser and the absorber are supplied with different sources of cooling water at the same cooling water inlet temperature and mass-flow rate.

In order to simplify the modeling of the system, several assumption were made, including:

1. The system operates in steady-state.
2. The system is perfectly insulated, so the heat exchange with the surroundings is only through the specified equipment.
3. Pressure drop along the fluid flow is negligible.
4. The pump work to drive the solution from the absorber is neglected.
5. In the shell side of the first-stage generator, the second-stage generator, and the absorber, the solution is in a saturated condition.
6. In the condenser the refrigerant condenses to a saturated liquid, while in the evaporator the refrigerant evaporates to a saturated vapor.
7. In evaluating the heat-transfer coefficients, the enthalpy of the steam generated in the first- and second-stage generators is taken to be the saturation enthalpy of vapor.
8. The steam generated in the first-stage generator condenses to a saturated liquid in the second-stage generator tube side.

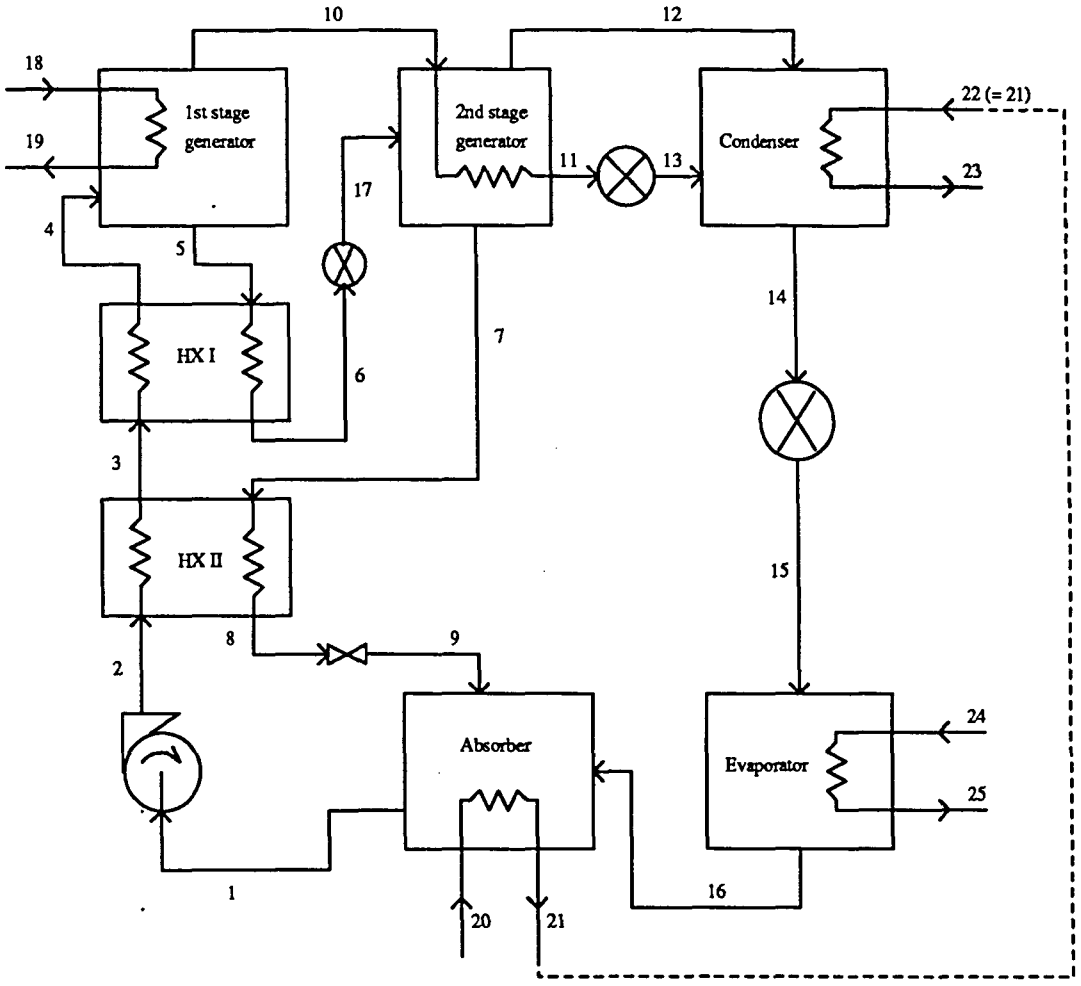

Figure 2.1: Schematic diagram of a double-effect $LiBr/H_2O$ absorption cooling system.

The First-Stage Generator

This heat exchanger is modeled as a shell and tube heat exchanger with hot water as the hot fluid flowing inside the tubes. High-pressure solution supplied by the pump comes through point (4) and develops a pool on the shell side. The heat transfer from the hot water to the the solution can be expressed in the following form:

$$Q_{1g} = \dot{m}_{10}h_{10} + \dot{m}_5 h_5 - \dot{m}_4 h_4 \tag{2.1}$$

$$Q_{1g} = \dot{m}_{18}\, Cp\, (T_{18} - T_{19}) \tag{2.2}$$

$$Q_{1g} = UA_{1g}\, \frac{(T_{18} - T_5) - (T_{19} - T_4)}{\ln \dfrac{(T_{18} - T_5)}{(T_{19} - T_4)}} \tag{2.3}$$

The total heat-transfer coefficient (UA) is obtained by the relation for tube configuration. For simplification of the model, the tube is presumably clean so that the effect of the fouling factor in both sides of the tube is neglected, giving the following relation:

$$UA = \frac{2\,\pi\, R_o\, \ell}{\dfrac{R_o}{R_i\, hc_i} + \dfrac{R_o \ln \dfrac{R_o}{R_i}}{k} + \dfrac{1}{hc_o}} \tag{2.4}$$

The heat transfer coefficient inside the tube is determined using the commonly available heat transfer correlation. To anticipate the possibility of varying the properties of the inlet hot water(18), it is worthwhile to write down the heat transfer correlation for both the laminar and turbulent flows. In the case of laminar flow, it is assumed that the heat flux through the tube wall is uniform. This assumption gives a constant Nusselt number [13].

$$Nu_l = 4.364 \tag{2.5}$$

For turbulent flow, A.F. Mills [13] recommended the Gnieleinski's formula for a more accurate result:

$$Nu_t = \frac{(f/8)\ (Re\ -\ 1000)\ Pr}{1\ +\ 12.7\ (f/8)^{1/2}\ \left(Pr^{2/3}\ -\ 1\right)} \tag{2.6}$$

where Pr is the Prandtl number and f is the friction factor of the tube. When a smooth tube is used in the system, Pethukov's formula, as mentioned in Reference [13] gives

$$f\ =\ (0.790\ \ln\ Re\ -\ 1.64)^{-2} \tag{2.7}$$

When the Reynolds number of the flow falls in the transition region, the Nusselt number is taken as the average of laminar and turbulent flows.

The purpose of the first-stage generator is to desorb the refrigerant out of the solution. This occurs if a sufficient amount of heat is transferred to the solution. The hot water is the heat source used to increase the solution temperature. As a result, the absorbency of the $LiBr/H_2O$ decreases, causing superheated refrigerant bubble development on the shell side surface of the tube. This process is enhanced at higher solution temperatures. However, the energy source temperature is limited by the possibility of crystallization of the solution. The algorithm for this process is adopted from the correlation developed by M. Hou and S. Tan [14]. In their study, they correlated the heat transfer coefficient as a function of various variables affecting the process. Their results also showed that the process might be enhanced if a low finned tube were used. This is because the grooved wall of a finned tube enlarges the evaporative area beneath the refrigerant bubble. However, the effect of finned tubes will not be included this study, so the tube is taken as a smooth tube. When the parameter containing the effect of the finned tube is specified as unity, the algorithm

for the process can be shown as

$$Nu = 0.16\left(\frac{qD}{\mu_l h_{fg}}\right)^{0.8588}\left(\frac{\rho_v}{\rho_l}\right)^{-0.7108}\left(\frac{q^2 D}{\tau_l \rho_v h_{fg}^2}\right)^{-0.2104} Pr^{0.2173} \left(\frac{P}{Ps}\right)^{0.3483} e^{-7.83610^{-2}XW} \tag{2.8}$$

In steady-state operation of the system, the mass balance requires that there be no mass accumulation in the heat exchanger. The mass balance for the first-stage generator can be expressed as

$$\dot{m}_4\, XW_4 = \dot{m}_5\, XW_5 \tag{2.9}$$

$$\dot{m}_4 = \dot{m}_5 + \dot{m}_{10} \tag{2.10}$$

The Second-Stage Generator

In a double-stage absorption cycle, a second-stage generator is added to utilize the heat of condensation of the refrigerant vapor generated in the first-stage generator. This condensation occurs in the tube side. As with the first-stage generator, the shell side heat-transfer processes are modeled as a pool of $LiBr/H_2O$ solution coming from the first-stage generator.

The refrigerant vapor generated from the first-stage generator is a superheated vapor. In the modeling of the second-stage generator, it is assumed that the steam is saturated and is condensed to a saturated liquid. The energy balances of this exchanger are

$$Q_{2g} = \dot{m}_{10} h_{10} - \dot{m}_{11} h_{11} \tag{2.11}$$

$$Q_{2g} = \dot{m}_{12}h_{12} + \dot{m}_7 h_7 - \dot{m}_{17}h_{17} \tag{2.12}$$

$$Q_{2g} = UA_{2g} \frac{(T_7 - T_{17})}{ln \frac{(T_{11} - T_{17})}{(T_{11} - T_7)}} \tag{2.13}$$

where UA_{2g} is the total heat transfer coefficient obtained using an equation similar to that for the first-stage generator (equation 2.4).

The inside convective coefficient for two-phase flow is obtained by using the correlation of W. H. Rohsenow [15], assuming 0.5 as the average quality of the condensing steam.

The mass balances in the second-stage generator can expressed as

$$\dot{m}_5 \, XW_5 = \dot{m}_7 \, XW_7 \tag{2.14}$$

$$\dot{m}_5 = \dot{m}_7 + \dot{m}_{12} \tag{2.15}$$

The Condenser

A horizontal shell and tube heat exchanger is used in modeling the condenser. The cooling water flows inside the condenser tubes and is supplied from the cooling water coming out from the absorber. For a two-phase flow heat exchanger, the capacity rate on the shell side is always greater than that on the tube side, which is a single-phase flow. When the ϵ-NTU method is used, the number of transfer units (NTU) and the effectiveness (ϵ) of the condenser are

$$NTU_C = \frac{UA_C}{\dot{m}_{22} \, Cp} \tag{2.16}$$

$$\epsilon_C = 1 - \exp(-NTU_C) \tag{2.17}$$

When a constant specific heat for the cooling water is assumed, the energy

balances in the condenser are

$$Q_c = \dot{m}_{22}\, Cp\, (T_{23} - T_{22}) \tag{2.18}$$

$$Q_c = \dot{m}_{12} h_{12} + \dot{m}_{13} h_{13} - \dot{m}_{14} h_{14} \tag{2.19}$$

$$Q_c = \dot{m}_{22}\, Cp\, \epsilon_c\, (T_{14} - T_{22}) \tag{2.20}$$

The total heat transfer coefficient for the condenser is determined using equation 2.4. In the condenser shell side, the refrigerant condenses on the horizontal tubes, forming saturated refrigerant leaving the condenser. However, a thorough study by A. F. Mill [13] shows that a subcooling effect in the condensate film on the tube side should be considered in determining the condensation convective coefficient. The subcooling effect may be incorporated by specifying the modified latent heat as

$$h_{fg} = \left(h_f - h_g\right) + \left(0.683 - \frac{0.228}{Pr_l}\right) Cp_l\,(T_{sat} - T_w) \tag{2.21}$$

where h_f and h_g are evaluated at the saturation temperature T_{sat} and all other properties are evaluated at T_r

$$T_r = T_w + 0.33\,(T_{sat} - T_w) \tag{2.22}$$

Following A. F. Mill [13], the algorithm for steam condensation on horizontal tubes is then

$$hc_o = 0.728 \left(\frac{\left(\rho_l - \rho_v\right)\, g\, h_{fg}\, k_l^3}{N\, \nu_l\, D\, (T_{sat} - T_w)} \right)^{0.25} \tag{2.23}$$

The steam coming in from the second-stage generator is assumed to be saturated vapor condensing into saturated liquid. The total refrigerant mass-flow rate is the sum of the steam mass-flow rate generated in both generators:

$$\dot{m}_{14} = \dot{m}_{13} + \dot{m}_{12} \tag{2.24}$$

The Evaporator

In the evaporator, the chilled water flows inside the tubes and rejects heat to the subcooled refrigerant coming from the condenser. The result is chilled water coming out, and saturated steam on the shell side.

The evaporation on the shell side is modeled as a falling film evaporation on a horizontal tube. The water film is generated by spraying the refrigerant on top of the tubes; the nonevaporated falling film is then recirculated to the refrigerant sprayer by a pump. Like the condenser, the evaporator gives the following number of transfer units (NTU) and effectiveness (ϵ):

$$NTU_e = \frac{UA_e}{\dot{m}_{24}\, Cp} \tag{2.25}$$

$$\epsilon_e = 1 - \exp(-NTU_e) \tag{2.26}$$

For a steady-state condition, the heat balances of the evaporator are

$$Q_e = \dot{m}_{24}\, Cp\, (T_{24} - T_{25}) \tag{2.27}$$

$$Q_e = \dot{m}_{15} h_{15} - \dot{m}_{16} h_{16} \tag{2.28}$$

$$Q_e = \dot{m}_{24}\, Cp\, \epsilon_e\, (T_{24} - T_{16}) \tag{2.29}$$

For falling film evaporation, Chun and Seban [16] have developed the heat transfer correlation. For laminar films

$$hc_o = 0.8221 \left(\frac{k_l^3 g}{\nu_l^2}\right)^{1/3} Re^{-0.22} \tag{2.30}$$

and for turbulent film evaporation

$$hc_o = 0.0038\, Re^{-0.4}\, Pr_l^{0.65} \left(\frac{k_l^3 g}{\nu_l^2}\right)^{1/3} \tag{2.31}$$

with the Reynolds number, Re, defined as

$$Re = \frac{4\,G}{\mu_l} \tag{2.32}$$

The transition of the falling film is determined by

$$Re_{tr} = 5800\ Pr_l^{-1.06} \tag{2.33}$$

The correlation developed by Chun and Seban [16] is based on falling film evaporation outside a vertical tube. For horizontal tubes, Kern [17] has specified that the load (G) can be empirically correlated as

$$G = \frac{\dot{m}}{\ell\ N^{2/3}} \tag{2.34}$$

Although the nonevaporated refrigerant is recirculated to the sprayer, the heat balance requires a constant mass-flow rate entering and leaving the evaporator shell side, so the mass balance in the evaporator becomes

$$\dot{m}_{14} = \dot{m}_{16} \tag{2.35}$$

The Absorber

The absorber in the system is modeled as a shell and tube heat exchanger. The saturated vapor generated in the evaporator is absorbed by the strong solution coming from the second-stage generator, resulting in a weak saturated solution leaving the absorber. The cooling water flowing in the tubes is used to enhance the refrigerant absorption because $LiBr/H_2O$ solution absorbs water better at lower temperatures. It is obvious that the cooling water supply has a significant effect on the system

performance. Under the first law of thermodynamics, at steady-state the energy balances in the absorber are as follows:

$$Q_a = \dot{m}_{20}\, Cp\, (T_{21} - T_{20}) \tag{2.36}$$

$$Q_a = \dot{m}_9 h_9 + \dot{m}_{16} h_{16} - \dot{m}_1 h_1 \tag{2.37}$$

$$Q_a = UA_a \frac{(T_9 - T_{21}) - (T_1 - T_{20})}{\ln \frac{(T_9 - T_{21})}{(T_1 - T_{20})}} \tag{2.38}$$

The total heat transfer coefficient (UA) is obtained in the same manner as for the first-stage generator. The convective coefficient inside the tubes is also obtained using equations which have been explained for the first-stage generator. The shell side heat transfer process involves heat and mass transfer of both the refrigerant and the solution. A study on this particular process by G. C. Vliet [7] shows that this process is too complicated to be expressed in a simple mathematic correlation. Following the study that has been conducted by G. C. Vliet [7], the convective coefficient in the shell side will be assumed constant at a value of 2268 W/m^2 C.

The mass balances in the absorber are obtained by assuming that there is no mass accumulation in the absorber, giving the following expressions:

$$\dot{m}_1\, XW_1 = \dot{m}_7\, XW_7 \tag{2.39}$$

$$\dot{m}_1 = \dot{m}_7 + \dot{m}_{16} \tag{2.40}$$

The Auxiliary Heat Exchangers

The auxiliary heat exchangers are used to recover the heat of the LiBr/H2O solution leaving both generators. The heat transfer processes involve single-phase

flow on both hot and cold sides. To simplify the solution of the system, the total heat transfer coefficient of both heat exchangers is taken at a constant value representing a typical value for a single-phase process at 800 W/m^2 C. The ϵ-NTU method gives the energy balance of each heat exchanger as a function requiring the inlet temperatures of the hot and cold sides:

$$\begin{aligned} CR &= \frac{(\dot{m}\ Cp)_{min}}{(\dot{m}\ Cp)_{max}} \\ NTU &= \frac{UA}{(\dot{m}\ Cp)_{min}} \\ \epsilon &= \frac{1\ -\ \exp(-NTU\,(1\ -\ CR))}{1\ -\ CR\ \exp(-NTU\,(1\ -\ CR))} \end{aligned} \tag{2.41}$$

The solution to the system as described in the next section will be arranged so the inlet temperatures of the hot and cold sides are available before the energy balance in the auxiliary heat exchanger is solved.

The Expansion Valves

Several expansion valves are used in the system. The purpose of these valves is to decrease the pressure of the flowing fluid. Under the general assumptions of no energy loss from the valves and steady-state operation, the energy balance requires that the incoming enthalpy should equal the outgoing enthalpy. Also at steady-state operation, the mass balance gives a constant mass-flow rate throughout each valve.

Method of Solution

In developing the computer code for simulation purposes, the cycle is modeled as a closed system with inputs and outputs as shown in Figure 2.2. The inputs of

the system include the flow rates and inlet temperatures of the hot water, cooling water, and chilled water. The outputs include the outlet temperatures of the hot water and the cooling water. As the cooling load is taken to be constant, the outlet temperature of the chilled water is predetermined to satisfy the given cooling load. The system model includes the characteristics for all of the heat exchangers, the pump, the expansion valves, and the piping. The heat transfer areas of the heat exchangers are design variable inputs. Property relations were also developed for both the refrigerant and $LiBr/H_2O$ solutions.

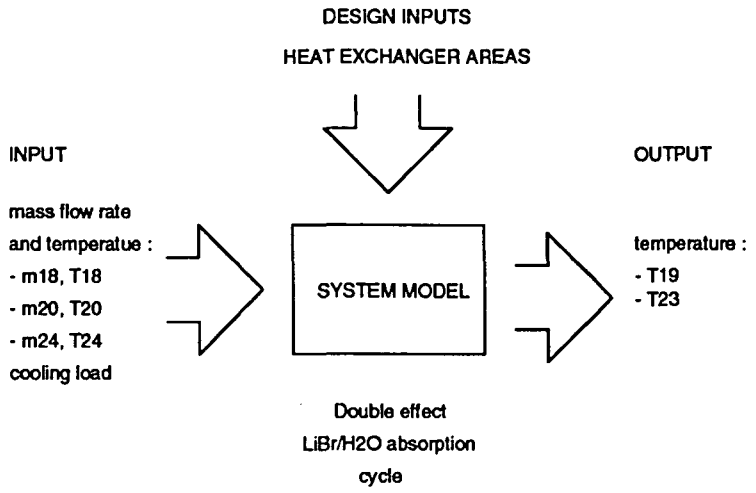

Figure 2.2: Schematic of the system model for developing computer code.

With the inputs specified in Figure 2.2, the solution of the system can be obtained by specifying a set of initial guesses of the properties of selected state points. The initial guesses were selected in such a way that with the input properties, the design criteria of the heat exchangers, the mass and energy balances, and the property relations, all other state point properties could be determined. The initial guesses

were then selected to be

- solution mass-flow rate leaving absorber ($\dot{m}_1$)
- absorber temperature (T_1)
- first-stage generator temperature (T_{10})
- condenser temperature (T_{14})
- evaporator temperature (T_{16})
- solution mass fraction leaving the first-stage generator (XW_5)

As will be described in the next section, the result of the initial guesses, the design inputs of heat exchanger, the mass and energy balances, and the property relations are a set of nonlinear equations with variables indicating the properties of each state point. Some of these variables are fixed by specifying them in the input part of the system model (Figure 2.2). The mass and energy balances of the system can be combined to give six nonlinear equations with six variables:

$$F_i\,(T_1, T_{10}, T_{14}, T_{16}, \dot{m}_1, XW_5) = 0 \tag{2.42}$$

where i = 1 to 6.

The Newton-Rhapson method was used to solved the set of nonlinear equations. This method requires an iterative calculation starting with the initial guesses. The correction factors for each variable (δx_i) were obtained by solving the Jacobian matrix. As the nonlinear equations are indirectly related to the variables, the Jacobian matrix was obtained numerically using the central difference method, giving a second-order truncation error.

$$\frac{dF_i}{dX} = \frac{F_i(X+\delta) - F_i(X-\delta)}{2\delta} \tag{2.43}$$

where

$$X = T_1, T_{10}, T_{14}, T_{16}, \dot{m}_1, XW_5$$
$$\delta = increment\ for\ X$$

The convergence of the calculation is achieved if the correction factor for each variable is less than the specified convergence criteria.

$$\delta x_i < convergence\ factor \tag{2.44}$$

where i = 1 to 6.

During the iteration, it is possible that the value of the new guesses may reach a point at which the properties at that condition are beyond the limits of the property relations which were obtained through curve fitting. To avoid this condition, the property routines were extrapolated, and the final results of the Newton-Rapshon method were then checked to see if any properties at the given condition lay beyond the limits of the property routines. Failing to follow the restriction results in no solution for the given inputs and characteristics of the heat exchangers (heat transfer area).

The initial guesses of the system solution include the solution mass-flow rate leaving the absorber ($\dot{m}_1$), the first-stage generator temperature (T_{18}), the condenser temperature (T_{14}), the evaporator temperature (T_{16}), the absorber temperature (T_1), and the solution mass fraction leaving the first-stage generator (XW_5). Based on these initial guesses, the properties of other state points were then calculated. The

total heat transfer coefficient for each heat exchanger is also specified as part of the initial guesses. At each iteration of the Newton-Rhapson procedure, new values for the total heat transfer coefficients are calculated based on the new set of state point properties.

In the condenser and evaporator, the refrigerant is pure water, so the saturation temperature of the heat exchanger corresponds with its saturation pressure. The pressure in the condenser and the evaporator can be determined by using the property relations. The property relations also give the relation between the saturation enthalpy for a given saturation pressure and temperature. As a result, the saturation enthalpies in the condenser and the evaporator can also be defined. In this study, the system simulation is based on constant load, so the cooling load is an input to the system. Once the enthalphies at the evaporator inlet and outlet are known, the refrigerant mass-flow rate in the evaporator is obtained by applying the energy balance in the evaporator.

For the $LiBr/H_2O$ solution, there is a property relation between the temperature, the pressure, and solution mass fraction in the saturated condition. It is assumed that effect of friction between the evaporator and absorber is negligible, so the absorber pressure is equivalent to the evaporator pressure. With this information and the initial guess of the absorber temperature(T_1), the solution mass fraction leaving the absorber (XW_1) can be obtained. The absorber solution enthalpy is obtained by employing the relation between solution temperature, mass fraction, and enthalpy. With the known initial guesses (T_5 and XW_5), the same procedure can also be used to determine the first-stage generator pressure and solution enthalpy. For pure refrigerant, the superheated enthalpy of the refrigerant leaving the first-stage generator

is related to its temperature and pressure, and this relation gives the enthalpy at the state point (10). Using the same property relations as in the condenser, one can obtain the saturation enthalpy of condensed steam in the second-stage generator.

Up to this point, most of the properties in the condenser, the evaporator, the absorber, and the first-stage generator have been solved. The next step is to apply the mass balances for the system. With the known refrigerant mass-flow rate in the evaporator and the solution mass fraction in the absorber and the first-stage generator, all mass-flow rates in the system can be solved. The solution mass fraction in the second-stage generator is determined by employing the energy balance in the second-stage generator. From the result of the previous calculation, the enthalphies in the second-stage generator have been defined. And with the tube side mass-flow rate and the total heat transfer coefficient, the second-stage generator temperature (T_7) is determined. As with the first-stage generator, the solution enthalpy and mass fraction as well as the enthalpy of the superheated refrigerant leaving the second-stage generator can be solved.

The last part is to determine properties around the auxiliary heat exchangers. These can be obtained by applying energy balances to the auxiliary heat exchangers. Finally, the variables at all state points, including the temperature, the pressure, the enthalpy, the mass-flow rate, and the solution mass fraction, are known.

Working Pairs Properties

The property relations for the $LiBr/H_2O$ solution and refrigerant were developed as part of the system modeling. For the $LiBr/H_2O$ solution, the available thermodynamic property relations can be obtained mostly through the curve fitting method

given in *ASHRAE Handbook Fundamentals Volume* [18]. However, to satisfy all required correlations, some modifications were performed on the available correlation, so it can be operated with the specified input variables.

The mass transport properties of the $LiBr/H_2O$ solution, including the solution specific heat, density, surface tension, thermal conductivity, and dynamic viscosity, were also developed using curve fitting methods. The curve fitting results are given in Appendix A.

The thermodynamic and mass-transport properties for water are more easily be obtained than those for the $LiBr/H_2O$ solution. For this study, these correlations for water were adopted from Toloukian [19, 20] and Irvine, J. R. [21].

Figures of Merit

For evaluating the system performance, figures of merit showing the performance of the system for a given set of design inputs were defined. The first figure of merit is the COP, which was previously defined as the ratio of the cooling load to the heat input to the first-stage generator. The second figure of merit is the life cycle system cost, which includes

- Initial cost of the heat exchanger (HX_{cost}).
- Operating cost (Opr_{cost}).

The initial cost of a heat exchanger is a function of the heat-transfer areas. This cost is obtained by assuming that the costs of other equipment are considered constant. For a given heat-transfer area, the cost of each heat exchanger is evaluated using an exponential scaling approach which is commonly used to estimate equipment

costs. This approach is based on a known cost for a type of equipment (C_{ref}), the ratio of the capacity of the desired equipment (Cap) to the capacity of the known equipment (Cap_{ref}) raised to a factor R_C, and the ratio of the price indices of the equipment in the current year (I) to the price indices of the known equipment (I_{ref}).

$$HX_{cost} = C_{ref} \left(\frac{Cap}{Cap_{ref}}\right)^{R_C} \left(\frac{I}{I_{ref}}\right) \tag{2.45}$$

In this study, the cost of each heat exchanger is obtained by correlating the specified heat exchanger to a heat exchanger with similar process characteristics. For heat exchangers, K. M. Guthrie [22] has developed charts showing typical costs to construct heat exchangers. The chart is based on the heat-transfer area of the heat exchanger for a given operating pressure and heat exchanger material and the exponential factor for cost scaling is given to be 0.68. Thus, after the reference cost and capacity have been selected and the price indices for the heat exchanger have been compared, the heat exchanger cost can be represented as a function of the heat-transfer area of the desired heat exchangers only.

The operating cost of the system refers to the system cost during its life cycle, which includes the cost of the heat input to the first-stage generator and also takes into account the hot water inlet temperature (T_{18}). In this study, other operating and maintenance costs are considered constant. In terms of the hot water inlet temperature, it is assumed that the higher the temperature, the higher the cost to supply this source of energy. The effect of the hot water inlet temperature is incorporated by multiplying the heat input cost by the ratio of the efficiency of a Carnot engine with energy supplied at temperature T_{18} to that of a Carnot engine with energy supplied

at the nominal temperature T_{18_n}. The Carnot engine is presumably rejecting heat at temperature T_{ref}. In other words, the effect of the hot water inlet temperature is incorporated by considering the ratio of its exergy when operating at temperature T_{18} to its exergy when operating at its nominal temperature (T_{18_n}).

The heat input cost is the cost to supply the energy to the first-stage generator. Although this energy is supplied by the hot water, in obtaining the cost of this energy, the heat input is correlated with the cost of producing the hot water with natural gas. If a 70 % operating time in a year (giving 6,132 working hours), a 20-year system life time, a 5.0 \$/GJ cost of natural gas, and a 90 % gas burner efficiency are assumed, the present worth of the heat input cost at 8 % interest rate may be represented as

$$Q_{1g}\ cost = 1202\ Q_{1g}\ \ \$/kW \tag{2.46}$$

When the effects of hot water inlet temperature are incorporated, the operating cost becomes (\$/kW)

$$Opr_{cost} = 1202\ Q_{1g} \left[\frac{1 - \frac{T_{ref}}{T_{18}}}{1 - \frac{T_{ref}}{T_{18_n}}} \right] \tag{2.47}$$

where T_{18n} is the nominal temperature (in absolute degrees) of the hot water inlet temperature. T_{ref} is taken to be the standard atmospheric temperature.

Finally, if the cost of other components such as the pump, piping systems, and valves is assumed to be constant, the second figure of merit (COST) is obtained as the sum of the operating cost and the initial exchangers cost.

$$COST = HX_{cost} + Opr_{cost} \tag{2.48}$$

Method of Optimization

The purpose of the heat-transfer area optimization is to determine the optimum area of each heat exchanger which will give the lowest relative system cost as defined in the previous section. For the number of heat exchangers included in the system, the optimization involves seven variables. Preliminary results of the simulation of the system show that increasing either one of the auxiliary heat exchanger areas increases the solution mass-flow rate leaving the absorber, and since the total heat-transfer coefficient is assumed constant for each auxiliary heat exchanger, the result will be the decreasing effectiveness of the other auxiliary heat exchanger. Therefore, the heat-transfer areas of the auxiliary heat exchangers are always kept equal. As a result, the optimization of the system involves only six variables.

There are several available optimization methods, including Newton's method, the steepest-descent method, the simplex method, and the lattice search method. Theoretically, Newton's method and the steepest-descent method could give an optimum result with a minimum number of iterations. But, as the procedure requires obtaining the Jacobian and/or Hessian matrices with six variables, these two procedures are considered inefficient in terms of calculation time. Besides, the iteration could end up with unreasonable values for the variables. This condition would cause problems for the next iteration.

The lattice search optimization method is performed by starting at a given initial point and checking the figures of merit at surrounding points. The next direction of the iteration is determined by comparing the figure of merit obtained from the surrounding point of each variable with the the figure of merit of the initial point. As the minimum point is the goal of the the optimization, the minimum figure of

merit is chosen to be the center of the next iteration. Convergence is obtained if the difference between the variables and their surrounding points reaches the given convergence factor.

The simplex method was also used to search the optimum figure of merit of the system. The results show agreement with the results of the lattice method. But, in terms of the number of iterations, in this particular study, the lattice search gives better results. So in the following study, the lattice search will be used as the optimization method.

CHAPTER 3. OPTIMIZATION AND SIMULATION OF $LiBr/H_2O$ ABSORPTION COOLING SYSTEMS

Nominal Design of the System

The nominal system is specified by the hot water, cooling water, and chilled water inlet temperatures and mass-flow rates, and by the heat-transfer areas of the system. For this study, a 20-ton cooling load is selected for the model of the nominal system. The sensitivity results are expected to be scalable to different cooling capacities. An optimization on the system configuration is used to determine the nominal system design.

The inlet temperatures of the hot water, cooling water, and chilled water depend on their availability from the environment, so these parameters will be used only as variables for the sensitivity study of the system. On the other hand, the mass-flow rates of hot water, cooling water, and chilled water might be considered as design variables. In this study, these values are based on standard rules-of-thumb used in commercial double-stage $LiBr/H_2O$ absorption cooling systems. The optimization is used to determine the optimum heat-transfer areas of each heat exchanger for the nominal system design.

In evaluation of the heat exchangers, the number of tubes is evaluated by specifying the fluid velocity inside each tube. It is obvious that this velocity has an effect on

the heat exchanger performance, since it affects the Reynolds number inside the tube. A high velocity causes a higher Reynolds number, and as a result the heat transfer coefficient inside the tube improves. On the other hand, higher velocity increases the pressure drop which also increases the pump work required to pump the fluid. Although the pump work is not evaluated in this study, the velocity inside the tube is selected following the commonly used value of 2 m/s. In the second-stage generator, the restricting point is also the pressure drop of the condensing steam inside the tube. But again, as assumed earlier, the pressure drop is neglected along the piping in the system and the steam velocity is taken at a value of 2 m/s. The tube dimensions, including the tube thickness and diameter, are also input variables. As with the hot water, cooling water, and chilled water mass-flow rate, the tube dimensions will be based on the standard used in commercial double-stage $LiBr/H_2O$ absorption cooling (Table 3.2). For the tube material, copper-brass is used in all heat exchangers except in the first-stage generator. To avoid tube corrosion due to high temperature fluid flowing in the tube, stainless-steel is used in the first-stage generator.

With the lattice search method, the nominal system design is obtained as shown in Table 3.1. As described earlier, the optimum condition of the variables is verified by checking the figure of merit of the surrounding points. Justification of whether or not this point is the global minimum of the objective function can be seen from the 3-D plots of the system cost as a function of several pairs of selected variables (Figures 3.1 to 3.6). These figures show an increasing figure of merit at a wide range of variables around the optimal point. For heat-transfer areas lower than those at the optimal point, the system requires higher energy input to the first-stage generator as the effectiveness of the heat exchanger decreases. Although the initial cost, which

is the cost of the heat exchanger, decreases, this decreasing cost is offset by the increasing operating costs of the system. On the other hand, at heat-transfer areas higher than those at the optimal point, the heat exchangers reach higher effectiveness, so the operating cost is minimized. Further increase of the heat-transfer areas causes an increase in overall system cost. Based on these results, it can be concluded that the optimum point obtained by the lattice search is the global minimum cost of the system for a given design of hot water, cooling water, and chilled water mass-flow rates and inlet temperatures.

Sensitivity Study of the System

The study of system performance at a constant cooling load is performed by determining the sensitivity of the system to each design variable. This determination is made by varying one of the variables over a given range (Table 3.1) while keeping the other variables at their nominal condition. The results show the sensitivity of the system performance, including the COP and the system cost, to each of the variables.

Figure 3.7 shows the effect of the heat exchanger areas on system COP. The trends show that the higher the heat-transfer area, the better the COP of the machine. The COP increases with increasing area and then levels off. The effect of changing the heat-transfer area of both auxiliary heat exchangers I and II was determined by simultaneously changing both areas. Increasing the auxiliary heat exchanger area also increases the mass-flow rate of the solution in the system. As a result, changing only one of these areas will decrease the effectiveness of the other heat exchanger.

Except for the absorber and the evaporator, the other heat exchangers reach their maximum effectiveness at heat-transfer areas of approximately 5 m^2, giving

Table 3.1: Nominal condition and simulation range for 20-ton cooling load capacity.

Variables	Nominal condition	Simulation range
Inlet temperature (^oC) :		
- Hot water , T_{18}	130.0	110 - 160
- Cooling water , T_{20}	29.5	22 - 32
- Chilled water , T_{24}	12.2	10 - 20
Mass-flow rate (kg/s) :		
- Hot water , $\dot{m}_{18}$	3.02	1.0 - 10.0
- Cooling water , $\dot{m}_{20}$	5.04	1.0 - 10.0
- Chilled water , $\dot{m}_{24}$	3.02	1.0 - 10.0
Heat-transfer area (m^2) :		
- 1st stage gen , AR_1	1.05	0.5 - 10.0
- absorber , AR_2	14.06	10.0 - 20.0
- condenser , AR_3	3.21	1.0 - 10.0
- evaporator , AR_4	9.74	5.0 - 15.0
- aux. HX I , AR_5	2.81	0.5 - 10.0
- aux. HX II , AR_6	2.81	0.5 - 10.0
- 2nd stage gen. , AR_7	2.23	0.5 - 10.0
Heat input required in the 1st stage gen., (kW)	49.45	
System COP	1.42	
System Cost, ($)	77527.50	

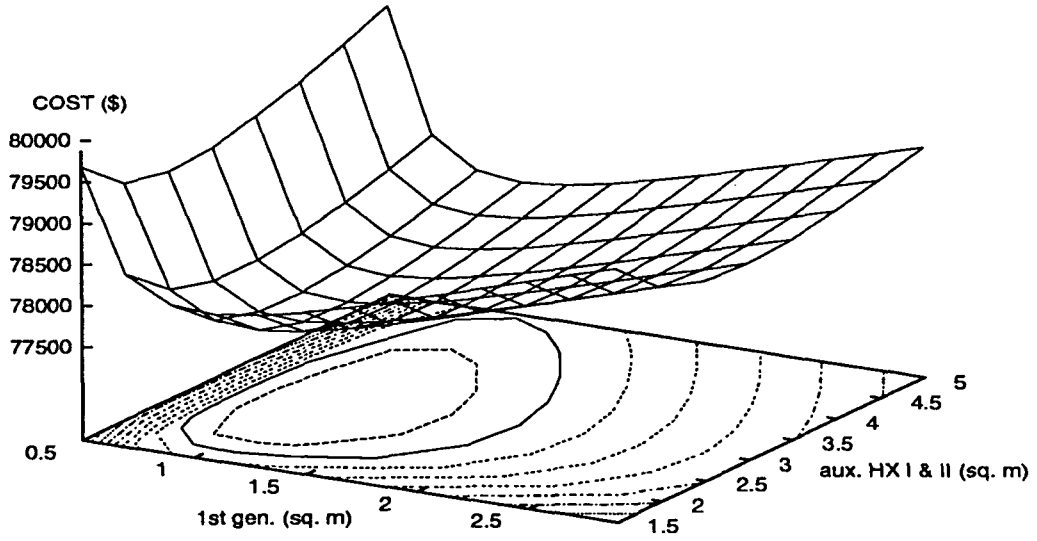

Figure 3.1: System cost as a function of the first-stage generator and the auxiliary HX areas.

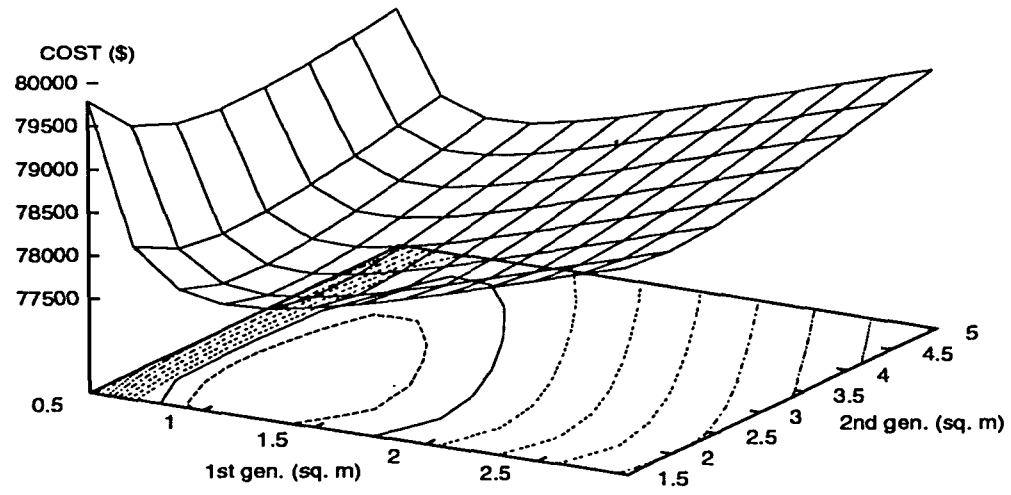

Figure 3.2: System cost as a function of the first-stage and the second-stage generator areas.

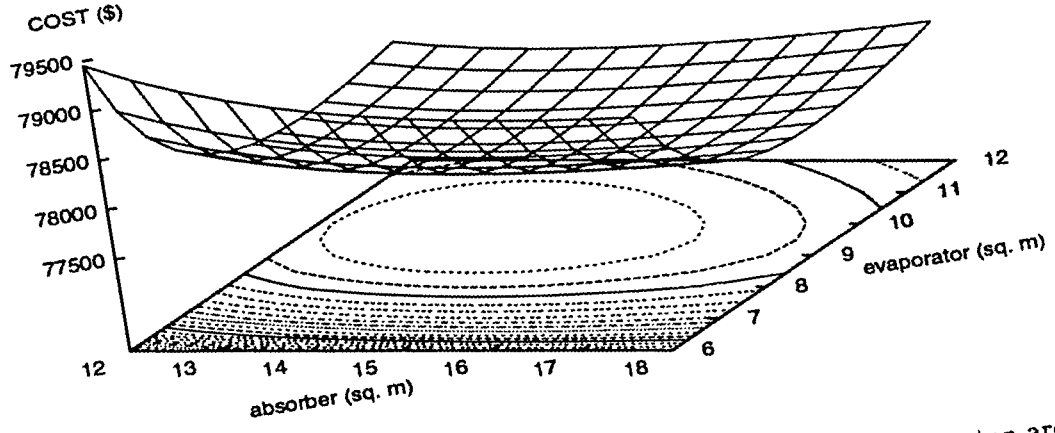

Figure 3.3: System cost as a function of the absorber and evaporator areas.

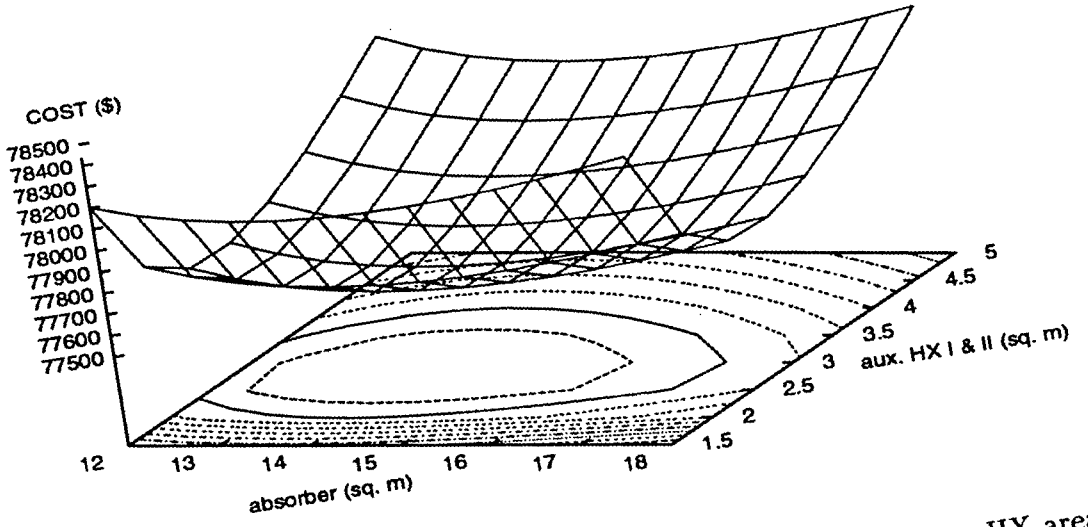

Figure 3.4: System cost as a function of the absorber and auxiliary HX areas.

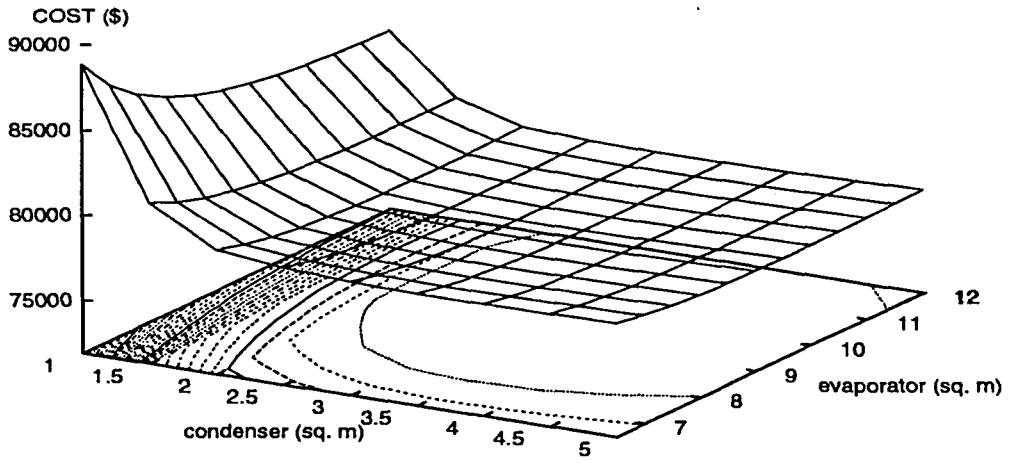

Figure 3.5: System cost as a function of the condenser and evaporator areas.

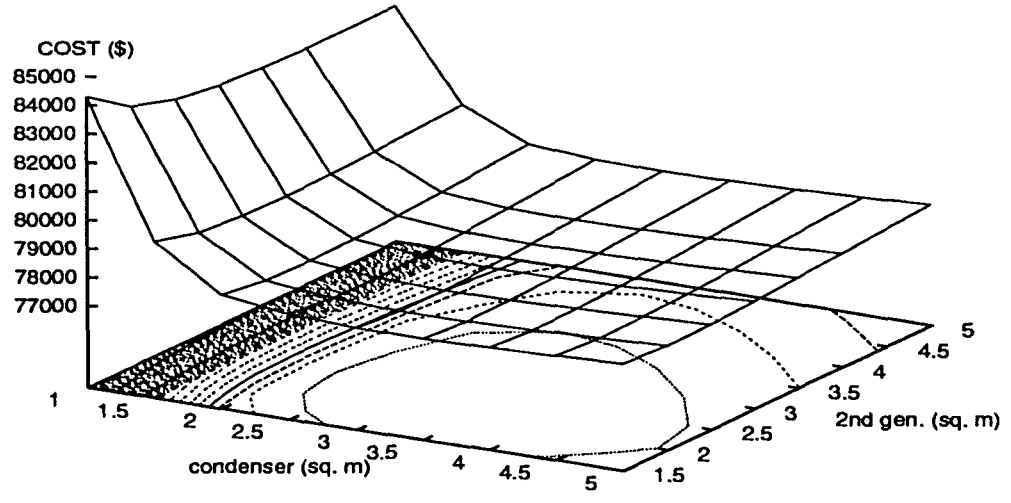

Figure 3.6: System cost as a function of the condenser and second-stage generator areas.

Table 3.2: Tube dimensions, properties, and velocity inside the tubes.

Equipment	Outside diameter (mm)	Thickness (mm)	Velocity inside the tubes (m/s)	Thermal conductivity (W/m K)
- 1st stage gen , AR_1	15.875	0.59944	2.0	15
- absorber , AR_2	15.875	0.59944	2.0	111
- condenser , AR_3	12.700	0.59944	2.0	111
- evaporator , AR_4	12.700	0.59944	2.0	111
- aux. HX I , AR_5	15.875	0.59944	2.0	111
- aux. HX II , AR_6	15.875	0.59944	2.0	111
- 2nd stage gen. , AR_7	12.700	0.59944	2.0	111

COPs between 1.4 and 1.5. For all heat exchangers, specifying a heat transfer area which is too small causes the COP to decrease quickly. Since the cooling load is kept constant, the decreasing COP indicates that the heat input to the first-stage generator increases. As a result, the operating cost increases. Figure 3.7 also shows that the absorber and evaporator are less sensitive than other heat exchangers. The COP increases slowly as the absorber and evaporator areas increase.

The effect of the heat-transfer area on the system cost can be seen in Figure 3.8. The trends show that the system cost decreases to an optimum point as the heat-transfer area increases because of an increase of the effectiveness of the heat exchanger. But further increases of the heat-transfer area increase the system cost more than they increase the heat exchanger's effectiveness. For this condition, the cost of the heat input to the first-stage generator is relatively low while the heat exchanger costs keep increasing.

Varying the hot water inlet temperature to the first-stage generator shows that for higher inlet temperatures, the system COP generally increases (Figure 3.9). The

COP increases steadily until the hot water inlet temperature reaches approximately 145^o C. Further increases in the hot water inlet temperature cause the COP to show a decreasing trend. This is due to the effect of the solution properties. A separate study shows that increasing the hot water inlet temperature increases the absorber temperature (T_1), while the cooling water coming out of the the absorber (T_{21}) is relatively constant. As a result, the absorber performance decreases, and this decreasing trend offsets the increasing trend due to higher hot water inlet temperatures. Increasing the hot water inlet temperature higher than 160^o C causes the system to not work properly. This is due the concentration of the solution leaving the second-stage generator increasing enough so that crystallization becomes a major problem. Increasing the chilled water inlet temperature also increases COP as expected (Figure 3.11). But, since the simulation was for constant load, higher chilled water inlet temperatures are not desirable for the cooling load.

Figure 3.10 shows the effect of hot water temperature on system cost. The curve has an optimal point. At higher hot water inlet temperatures, the increased cost is mainly due to the increased cost of high-temperature hot water. At temperatures below the optimal point, the unit cost of the hot water decreases, but the decreasing COP makes higher heat energy input necessary to keep the load constant.

Figure 3.12 shows the effect of the cooling water inlet temperature on COP. Unlike the effects caused by the variation of the hot water and the chilled water inlet temperatures, an increase in the cooling water temperature tends to decrease the system COP because of decreased absorber effectiveness. The absorption of the refrigerant vapor generated in the evaporator by the high concentration $LiBr/H_2O$ solution coming from the second-stage generator improves as the solution temperature

decreases. An increase in the cooling water temperature decreases the absorption of refrigerant vapor by the $LiBr/H_2O$ solution.

The effect of the hot water, cooling water, and chilled water mass-flow rates on the system's COP and cost are shown in Figures 3.13 and 3.14. The trend shows that the hot water mass-flow rate does not have an effect on the system performance. This is because for a constant load and a constant heat-transfer area, the system also requires constant heat input to the first-stage generator. Review of the heat balance equation in the first-stage generator shows that an increase in the hot water mass-flow rate ($\dot{m}_{18}$) causes a decrease in the temperature difference between the hot water inlet and outlet temperatures (T_{18}-T_{19}) for constant heat input (Q_{1g}). It may be concluded that the specification of the hot water mass-flow rate will depend on hot water availability. If solar energy is used as the main energy input, a smaller temperature difference between the inlet and outlet hot water temperatures will be an advantage, because smaller heat input is required if the outlet water flow rate is recirculated as the input for the solar collector system. On the other hand, pump work and mass-flow rate increase if a smaller temperature difference is used.

Unlike the hot water mass-flow rate, the cooling water and the chilled water mass-flow rates have a significant effect on the system performance. An increase in the cooling water and chilled water mass-flow rates increases the system COP. This effect is due to an improvement in the absorber and evaporator performances. As described earlier, the steam absorption by the $LiBr/H_2O$ solution is enhanced at a lower absorber temperature. Higher cooling water mass-flow rate increases the heat-transfer coefficient, and as a result the absorber performance is enhanced. The same phenomenon also occurs in the evaporator. Like the effect of the chilled water inlet

temperature (Figure 3.11), the effect of an increase in the chilled water mass-flow rate at a constant cooling load is to decrease the temperature difference between the chilled water inlet and outlet temperatures (T_{24}-T_{25}). For a cooling system, this trend is not desirable, so the chilled water mass-flow rate should be kept at a value which gives the desired outlet temperature for a specified cooling load.

The heat-transfer areas at the nominal condition are based on the commonly available standard configuration of a double effect LiBr/H_2O cooling system in which the cooling water flows in series from the absorber to the condenser (Figure 2.1). A study of the 20-ton cooling load with a different cooling water configuration has been investigated. This configuration has the cooling water flow to the condenser first and then in series to the the absorber (configuration C-to-A). Another possibility is to supply the absorber and condenser with separate cooling water supplies (configuration C-and-A). Figures 3.15 and 3.16 show the results of these various configuration. The results show that the C-and-A configuration gives the highest COP. It can also be seen that C-to-A and C-and-A configuration require smaller cooling water mass-flow rates before the COP curve levels off. In terms of the system cost, the C-to-A gives the lowest cost. Since the simulation was based on the same heat-transfer area for each heat exchanger, this trend also shows that the C-and-A configuration requires the smallest heat input to the first-stage generator compared with other cooling water configurations. However, a consideration to use the C-and-A configuration should also take into account the additional cost that has to be provided for additional pump and cooling water supply.

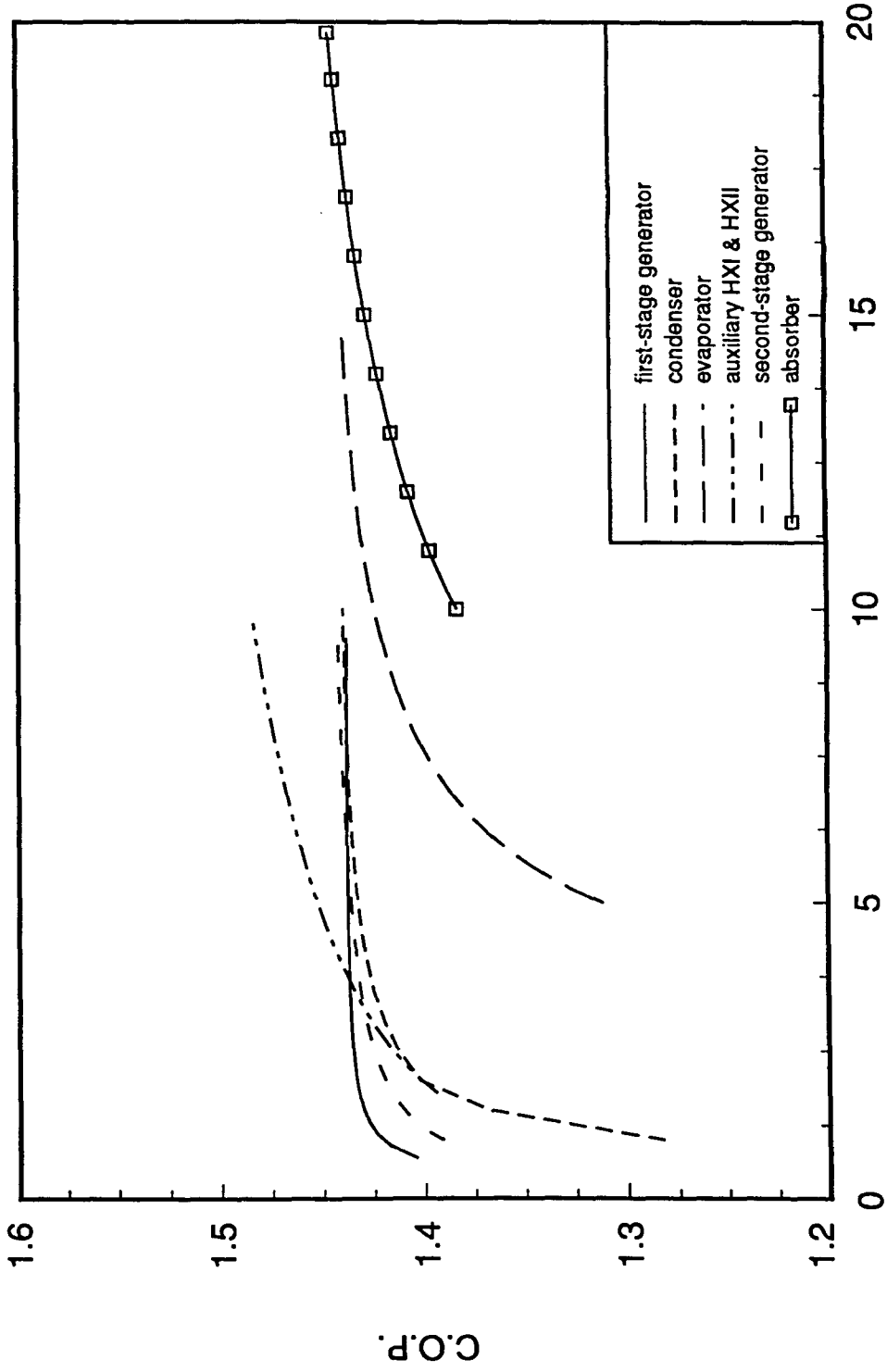

Figure 3.7: System performance as a function of heat-transfer areas.

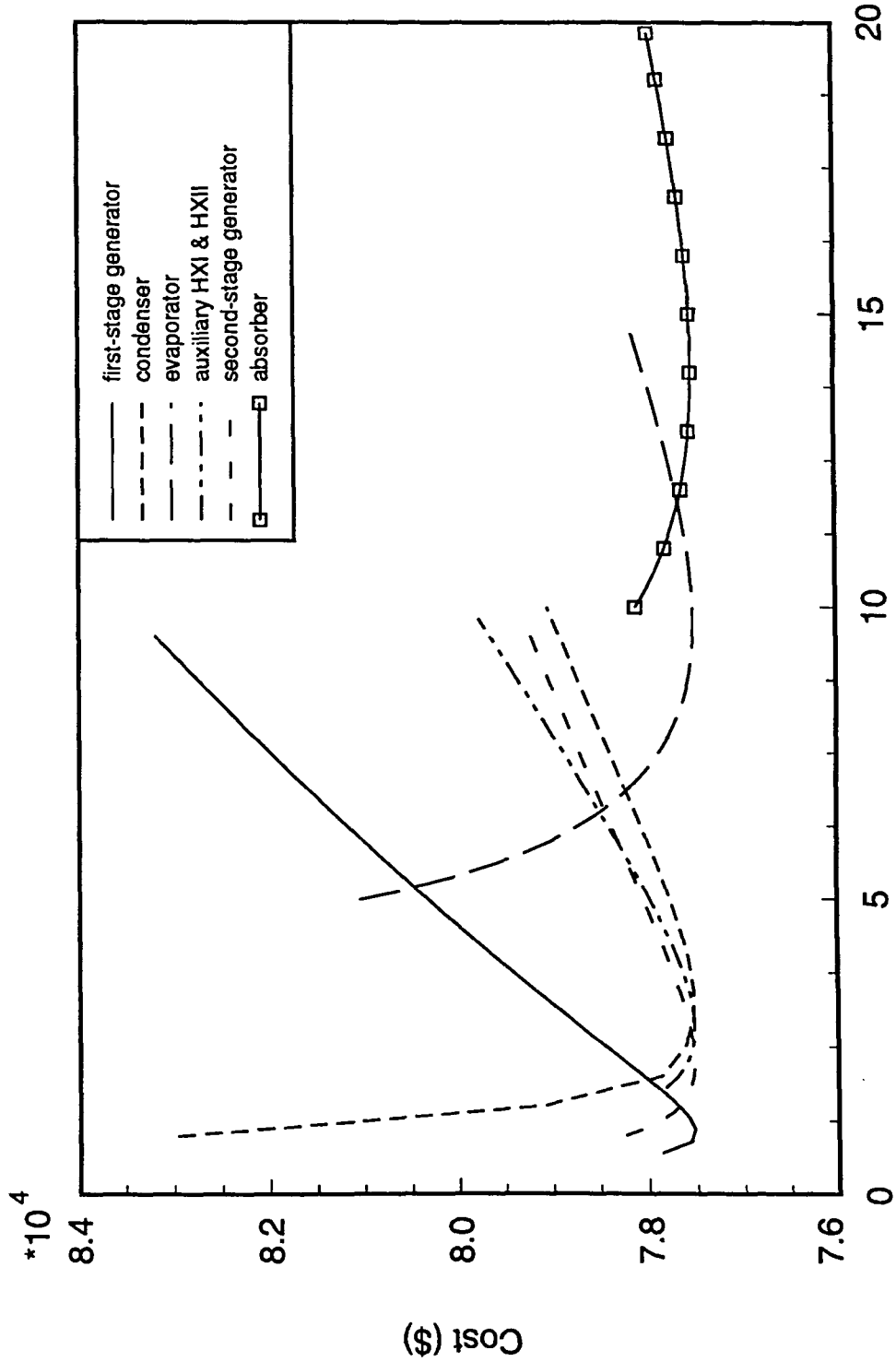

Figure 3.8: System cost as a function of heat-transfer areas.

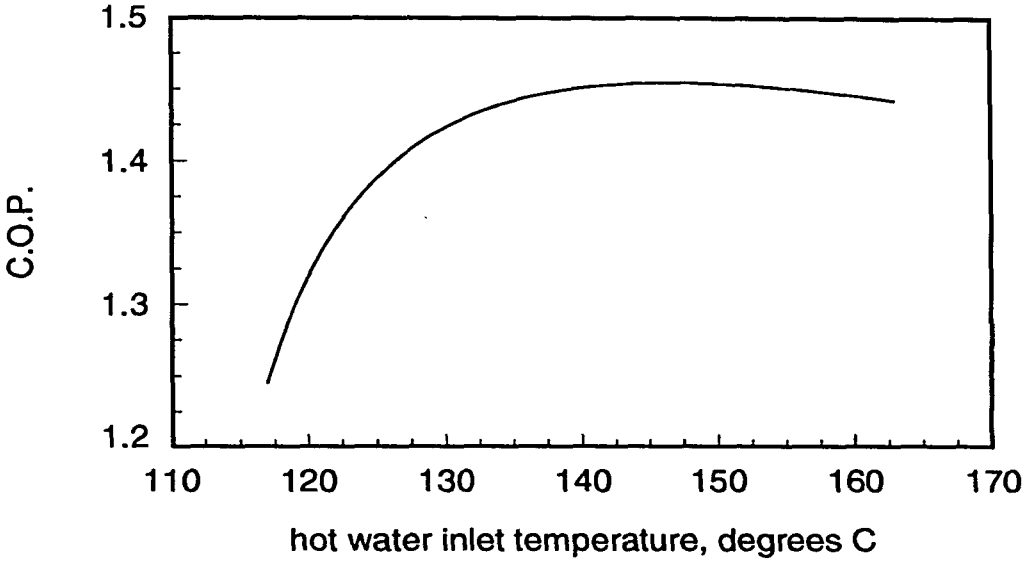

Figure 3.9: System performance as a function of hot water inlet temperature.

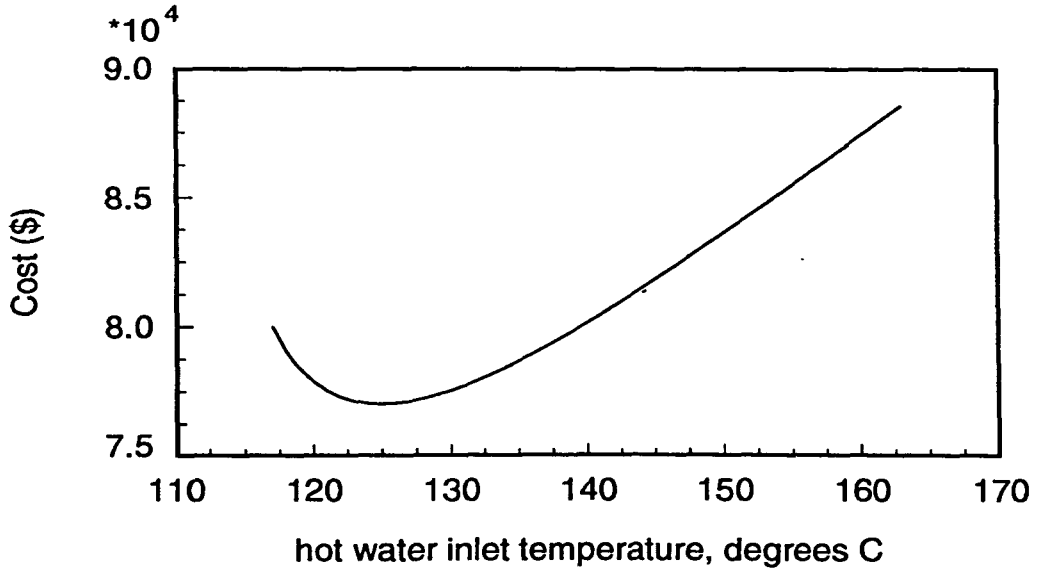

Figure 3.10: System cost as a function of hot water inlet temperature.

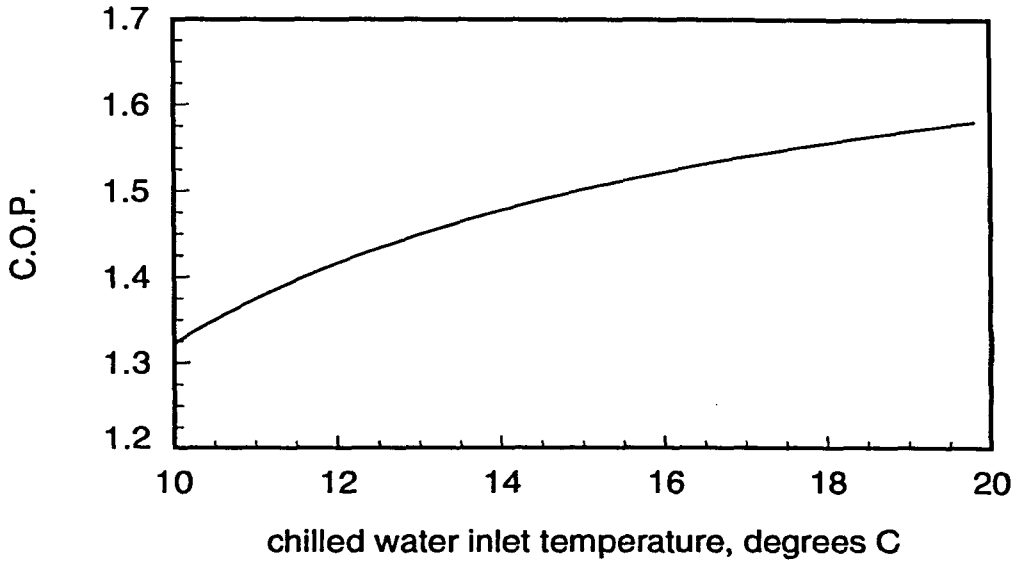

Figure 3.11: System performance as a function of chilled water inlet temperature.

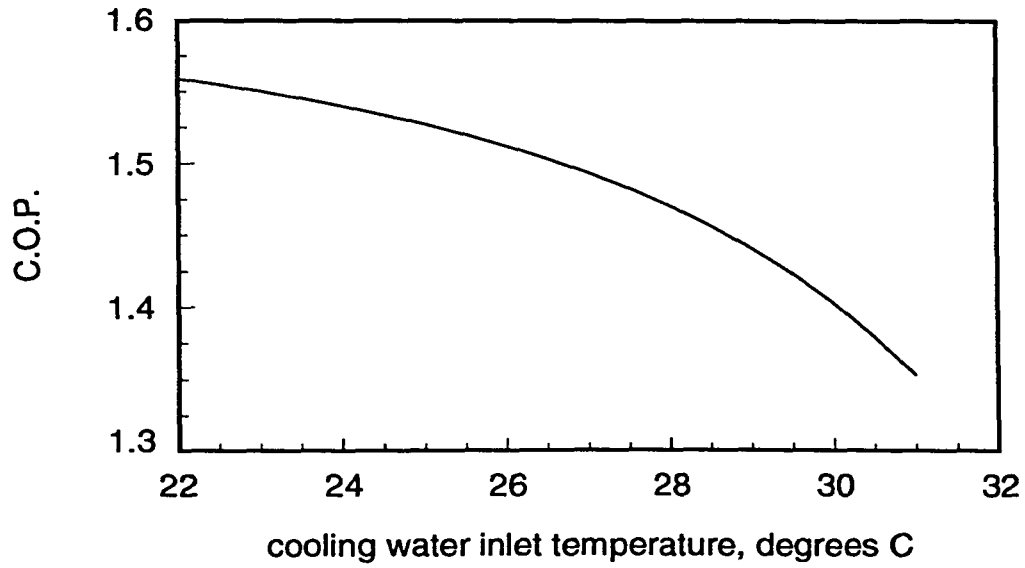

Figure 3.12: System performance as a function of cooling water inlet temperature.

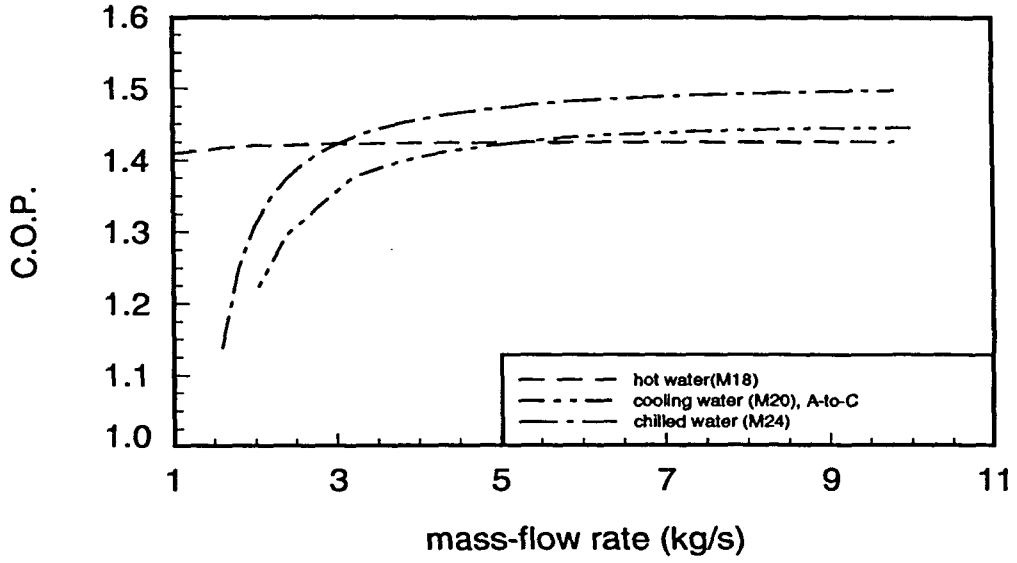

Figure 3.13: System performance as a function of variation on mass-flow rate.

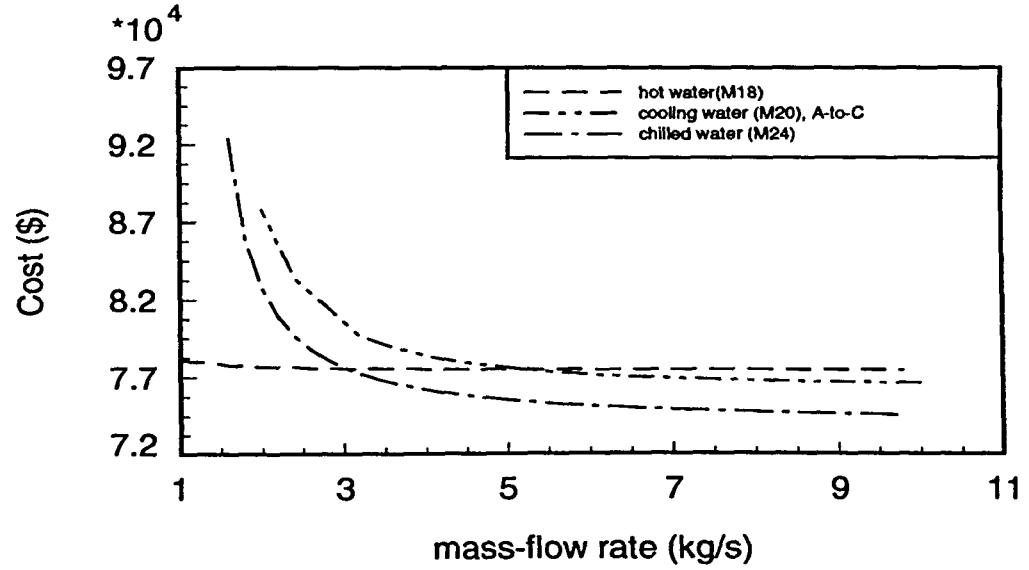

Figure 3.14: System cost as a function of variation on mass-flow rate.

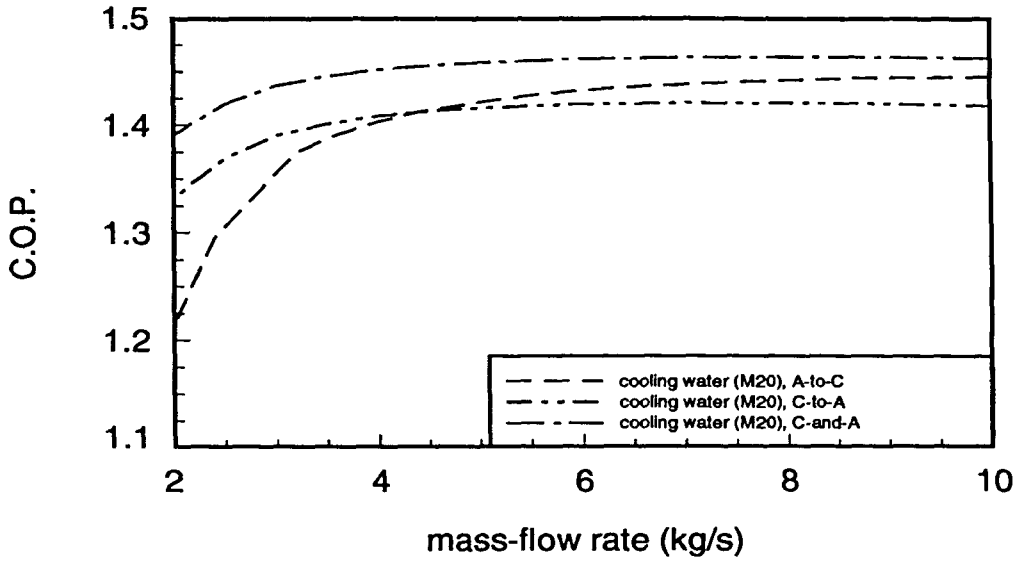

Figure 3.15: System performance as a function of variation on cooling water mass-flow rate with different cooling configuration.

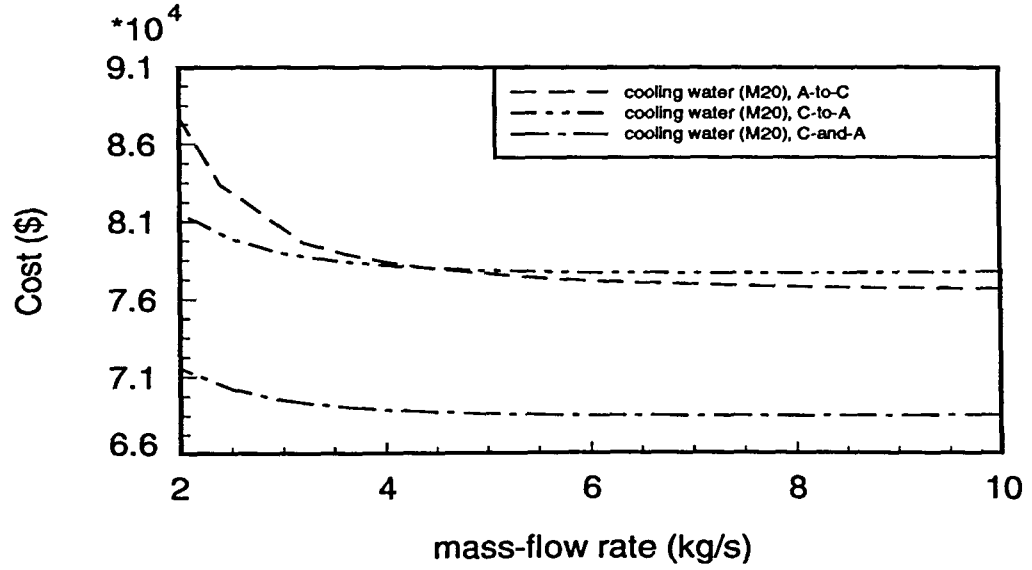

Figure 3.16: System cost as a function of variation on cooling water mass-flow rate with different cooling configuration.

CHAPTER 4. SOLAR ABSORPTION COOLING

The simulation and optimization of a double-effect $LiBr/H_2O$ cooling system has been described in the previous chapter. In that study, the energy input to the first-stage generator is obtained by supplying hot water to the tube side of the first-stage generator. The results show that for a 20-ton cooling load, the system works satisfactorily if the hot water inlet temperature is between 120^o C and 160^o C. The simulation results also show that the hot water mass-flow rate does not have a significant effect on the cooling system performance.

In the first chapter, the possibility of using solar energy as the energy supply to the first-stage generator was discussed. In order to predict the performance of a solar powered double-effect $LiBr/H_2O$ cooling system, a computer model for a solar collector has been developed. The model is coupled with the computer model for the double-effect $LiBr/H_2O$ cooling system. The simulation is then performed on an hourly basis for a day representing the average day of a specified month.

Solar Collector Modeling

The solar collector model is comprised of a solar collector to capture the solar energy, a storage tank, and piping systems. A combination with a heat exchanger between the collector and the storage tank allows the use of antifreeze solutions in the

collector loop. This helps prevent freezing during winter conditions. The schematic of the collector system that will be used in the computer model is shown in Figure 4.1. A water storage tank is used to store the solar energy received by the collector in the form of sensible heat.

During a typical day, the available solar energy varies. It is also affected by the declination of the sun, which varies over a year. In analyzing the energy balance of the storage tank, a nonsteady process is assumed. Considering the storage tank alone as the control volume, and assuming that there is no heat exchanger in the system, the energy balance gives

$$M_T Cp_s \frac{dT_s}{dt} = Qu - L - (UA)_{loss}(T_s - T_{room}) \tag{4.1}$$

In finite difference form, equation 4.1 can be represented as

$$T_s^+ = T_s + \frac{\Delta t}{M_T Cp_s}\left(Qu - L - (UA)_{loss}(T_s - T_{room})\right) \tag{4.2}$$

where L is the load supplied by the storage tank and Δt is the time interval for evaluating the temperature of the storage tank. Since the solar radiation is on an hourly basis, a one-hour interval was also used for Δt. The load supplied by the storage tank (L) is calculated when the storage tank is contributing energy to the cooling system and is evaluated as

$$L = \dot{m}_{18} Cp(T_s - T_{19}) \tag{4.3}$$

The useful energy gained by the solar collector (Q_u) can be obtained by measuring the inlet and outlet temperatures of the working fluid using

$$Q_u = \dot{m}_c Cp_c(T_o - T_i) \tag{4.4}$$

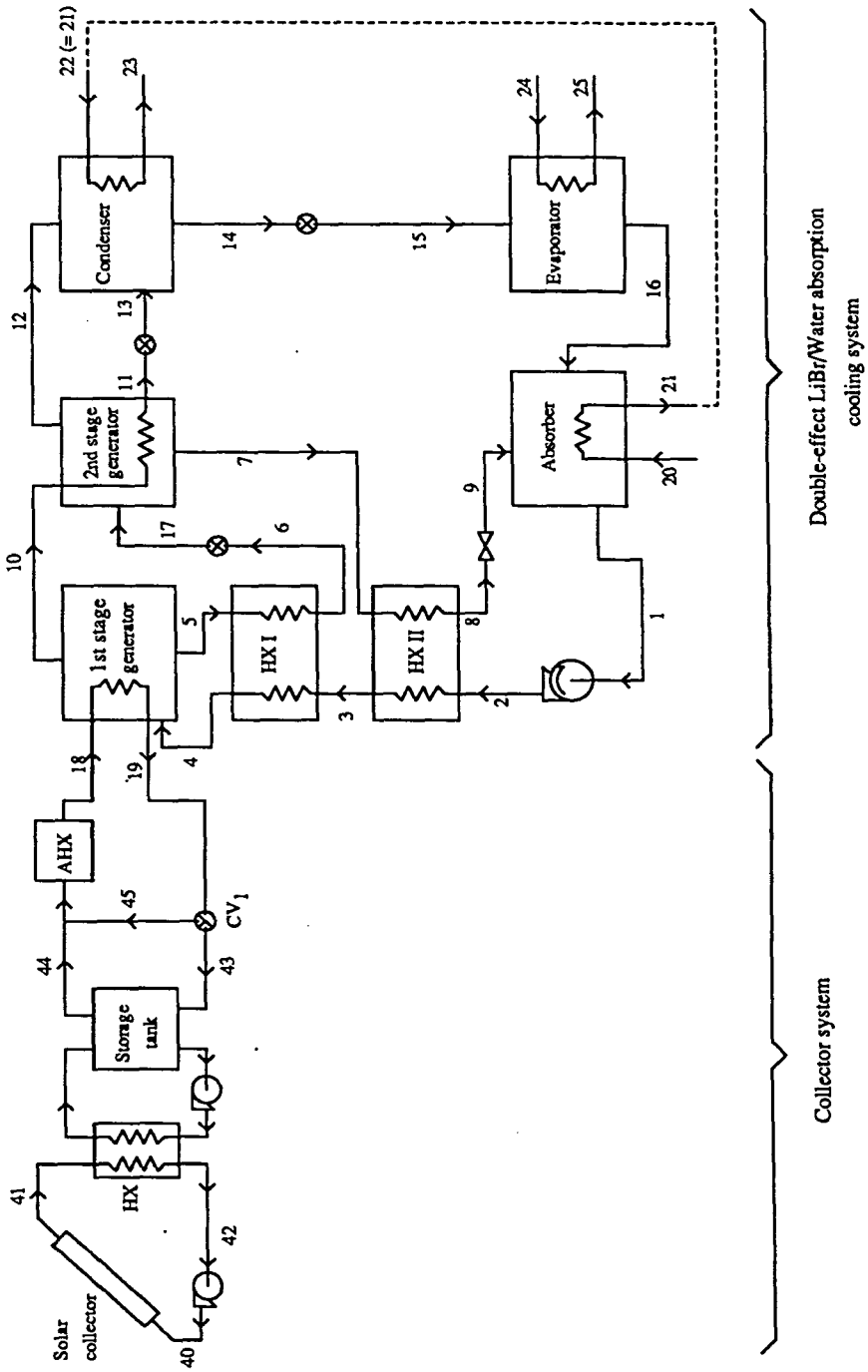

Figure 4.1: Schematic of a solar powered cooling system.

In addition, the useful gain (Q_u) can also be measured in terms of the collector performance. Using this method, the useful gain is a function of the collector area and other variables including the hourly solar radiation received by the collector (I_T).

$$Qu = AcF_R\left(I_T(\tau\alpha) - U_L(T_i - Ta)\right) \tag{4.5}$$

Using above procedures, the accuracy of the model will depend both on the accuracy of the parameters in the equations and on how quickly T_s varies. Review of equation 4.2 shows that the error in T_s^+ is partly due to evaluating the right-hand side of the equation at the storage tank temperature at the beginning of the hour (T_s) instead using an average temperature for the hour. Additional errors are due to the hourly averaged evaluation of the available solar energy (Q_u). Measurements show that the accuracy of this type of model should be within $\pm$ 20 % [2].

If there are no losses of solar radiation in the atmosphere, the collector will receive hourly radiation in an amount equal to the extraterrestrial radiation. In fact, the sky clearness will have a great effect on the transmission of the solar radiation, so in evaluating the hourly insolation, the extraterrestrial radiation is reduced by the sky clearness index k_t.

The useful gain received by the working fluid will then be evaluated by incorporating the losses due to the temperature difference between the collector and the ambient air (U_L) and to the optical losses from the collector material ($\tau\alpha$). The heat removal factor (F_R) is defined as the ratio of the actual useful gain of a collector to the useful gain if the collector surface is at the working fluid inlet temperature. This quantity is similar to heat exchanger effectiveness, which is defined as the ratio of the actual heat transfer to the maximum possible heat transfer, so F_R varies between 0 and 1. When equation 4.4 with equation 4.5 are equated, it can be seen that the

heat removal factor increases if the working fluid mass-flow rate is increased because the temperature rise through the collector decreases.

The addition of the collector heat exchanger allows the use of antifreeze solutions as the collector working fluid. On the other hand, it will decrease the useful gain received by storage tank because the solar collector will have to operate at a higher temperature and therefore have more losses. As mentioned in Reference [2], deWinter has studied the effect of the combination of a solar collector with a heat exchanger, and the result is given by replacing the heat removal factor with the modified heat removal factor (F_R'). The modified collector heat removal factor (F_R') accounts for the presence of the heat exchanger and is given by

$$\frac{F'_R}{F_R} = \frac{1}{1 + \left(\frac{AcF_RU_L}{(\dot{m}Cp)_c}\right)\left(\frac{(\dot{m}Cp)_c}{\epsilon(\dot{m}Cp)_{min}} - 1\right)} \tag{4.6}$$

where $(\dot{m}\ \mathrm{Cp})_{min}$ is the smallest product of mass-flow rate and fluid specific heat between the tube and shell side of the counterflow heat exchanger.

The collector efficiency is defined as the ratio of the useful gain to the actual solar incident on the collector surface.

$$\eta = \frac{Qu}{AcI_T} \tag{4.7}$$

It can also be expressed as

$$\eta = F_R(\tau\alpha) - F_RU_L\frac{(T_o - T_i)}{I_T} \tag{4.8}$$

Performance tests on several types of collectors show that if U_L, F_R, and $(\tau\alpha)$ are all constant, the plot of the collector efficiency (η) against $(T_i - T_a)/I_T$ is a straight line with intercept $\left[F_R(\tau\alpha)\right]$ and slope $\left[-F_RU_L\right]$. But actually, U_L is a weak

Table 4.1: Collector system specifications.

$F_R(\tau\alpha)$	0.76
$F_R(U_L)$, (W/m^2 C)	4.06
F'_R/F_R	0.95
Ground reflectance (ρ_g)	0.30
Tank capacity (M_T), (m^3/m^2)	0.10
Collector mass flow rate ($\dot{m}_C$), (kg/m^2 s)	0.015
Tank loss coefficient (U_{loss}), (W/m^2 C)	0.24
Collector working fluid	80 % ethylene glycol

function of temperature and wind speed, and F_R is a function of U_L. However, as is commonly done for collector model simplification, the collector will be characterized by constant intercept and slope.

Operation of Combined Collector and Cooling System

For the purpose of this study, a fixed flat plate collector oriented toward the equator and having the specifications given in Table 4.1 is used for the system. The collector is placed in Ames, Iowa, at latitude (ϕ) = 42.03^o N. The slope of the collector is arranged so that the collector is normal to the sun when the cooling load is the highest. A commonly used method is to tilt the collector at the latitude minus 20^o. Thus, the slope of the collector (β) can be determined as 22.03^o.

An auxiliary energy source is added to the collector system to supply energy when the solar energy is depleted. Review of the simulation results of the cooling system as a function of hot water inlet temperature (Figure 3.9) shows that if the hot water inlet temperature is too low, the cooling system will not work properly. To

keep the cooling system working, a minimum hot water inlet temperature (T_{18min}) of 120^o C is specified.

The result of the simulation as given in the previous chapter also shows that there is a possibility of crystallization of the working fluid in the generator if the hot water supply temperature is too high. To avoid this problem, a maximum temperature that can be supplied (T_{18max}) is specified at 160^o C. In case the storage tank temperature (T_s) is higher than 160^o C, the collector outlet working fluid is vented so the storage tank temperature can be kept at the maximum temperature allowed in the inlet of the first-stage generator (18).

In operating the collector system, the flow of hot water is controlled by the control valve (CV_1). This valve is operated so that the auxiliary heat exchanger is not used if the storage tank temperature is higher than the minimum required hot water inlet temperature (T_{18min}). At this stage, all of the heat input required by the first-stage generator is supplied by the collector system. When the storage tank temperature (T_s) is lower than the minimum hot water inlet temperature required (T_{18min}), which could happen if the solar energy is depleted, the auxiliary heat exchanger (AHX) is started to increase the temperature of the hot water supply to the minimum required hot water inlet temperature (T_{18min}), and the load on the storage tank is zero. However, to minimize the energy to be supplied by the auxiliary heat exchanger, the storage tank temperature (T_s) is compared with the hot water outlet temperature (T_{19}). In this way, the control valve (CV_1) is operated to choose the highest of these temperatures. If the hot water is supplied by the storage tank, the storage tank load (L) is then evaluated to determine the storage tank temperature for the next hour. On the other hand, when the hot water flow is supplied by the

outlet of the hot water from the first-stage generator using the bypass valve (CV_1), the collector system does not give any energy contribution to the cooling system (L = 0). During this period, the collector may keep on operating to increase the storage tank temperature.

A review of the availability of the solar energy in a day, and the high operating temperature of the collector working fluid indicates that continuous operation of the collector working fluid flow is not desirable, because energy losses from the collector to the environment could occur if there were no solar radiation. This could also happen if the available solar energy, especially early in the morning and late afternoon, were not high enough to raise the collector working fluid temperature. To avoid these losses, the operation of the collector pumps is controlled by the collector outlet temperature. These pumps are turned off at any time when the collector outlet temperature is equal to or lower than the collector inlet temperature.

To simulate the the collector system, an initial guess is given for the storage tank temperature (T_S). The useful gain and the storage tank load are calculated, and the new storage tank temperature (T_S^+) can be obtained for the next hour. This step is repeated for a 24-hour period, and convergence is obtained if the initial guess for the storage tank is equal to the new storage temperature after 24 hours of operation. Otherwise, the calculation is started again using the last new storage temperature for the initial guess of storage tank temperature for the next iteration.

To evaluate the monthly solar energy contribution to the cooling system, the monthly performance of the combined collector and absorption cooling is represented by the 24-hour operation on the average day of the month. At any time the cooling machine is working to supply the demanded cooling load, the total energy supply

to the cooling system which is shown by the required heat input to the first-stage generator (Q_{1g}) is obtained as the sum of the heat input supplied by the auxiliary heat exchanger (AHX) and that supplied by the storage tank (L). For the 24-hour period, the fraction of solar contribution (F_S) to the energy supplied to the cooling system is defined as the ratio of the daily storage tank load (L) to the daily heat input to the first-stage generator (Q_{1g}). However, to incorporate the cooling demand variation due to the variation of the ambient temperature in a day, for each hour, the storage tank load (L) and the heat input required in the first-stage generator (Q_{1g}) in a specific hour are evaluated by multiply them with the cooling demand fraction (f_r) for that hour. (For a discussion of the cooling demand fraction (f_r), see the following section.)

$$F_S = \frac{\sum^{day} (L\ f_r)}{\sum^{day} (Q_{1g}\ f_r)} \tag{4.9}$$

Cooling Demand Evaluation

From a Local Climatological Data Monthly Summary [23] for Des Moines, Iowa, which will be used as a reference for cooling demand, it can be seen that the cooling season is from May through September. Also, the average ambient temperatures during that cooling demand period vary (Table 4.2), so the cooling load also varies. Since the solar cooling is evaluated on an hourly basis, it is also necessary to establish an hourly ambient temperature based on the average ambient temperature. Assuming a constant 14^o C daily temperature range (D_R) and a peak cooling demand at

3:00 PM, we can express the hourly ambient temperature as a function of time (HR) and the average ambient temperature (T_{ave}):

$$T_a = T_{ave} + \frac{D_R}{2}\cos((HR - 15)15) \tag{4.10}$$

With respect to this condition, the hourly fraction of cooling demand is specified as the ratio of the cooling demand in that hour to the nominal capacity of the cooling machine. When a common total convective coefficient (UA_{load}) for a 20-ton nominal cooling load (Ln) and a 17^o C effective temperature that must be maintained by the cooling machine is specified, the hourly fraction of cooling demand (f_r) is given by

$$f_r = \frac{UA_{load}(T_a - 17)}{3,518Ln} \tag{4.11}$$

From equation 4.11, it can be seen that the cooling fraction (f_r) could be negative if the ambient temperature (T_a) were below 17^o C. In this case the cooling fraction is specified to be 0, which means that no cooling load is necessary and the cooling machine does not need energy. Review of equation 4.10 shows that this condition could occur at a time when the solar energy is minimum, so an evaluation in this way would be in line with the fact that cooling demand increases as the solar energy increases.

Table 4.2: Monthly average ambient temperature for Ames, IA, and Alburqueque, NM. (^{o} C).

Location	May	Jun	Jul	Aug	Sept
Ames, IA	15	20	23	22	17
Alburqueque, NM	17	22	25	23	20

Solar Assisted Cooling Simulation Result

Based on the collector model and the model of a double-effect $LiBr/H_2O$ absorption cooling system as given in the previous chapter, the solar cooling simulation was performed by assuming that the cooling machine is located in Ames, Iowa. The cooling demand occurs only from May until September, so the simulation was performed only for that period. In that period (May-September), the variation of the sky clearness index (kt) varies between 0.51 and 0.56 [2]. For an average sky clearness index of 0.54, the simulation result is plotted as solar fraction as a function of time (month).

Figure 4.2 shows the result of the simulation for various collector areas. From the figure, it can be seen that for each specified collector area, the solar fraction is the lowest in July. This is due to the average ambient temperature being higher, so the cooling demand increases in July. On the other hand, at a lower average ambient temperature, as in May and September, the cooling demand decreases. As a result, the demand for the energy input to the first-stage generator also decreases. Using a larger collector area gives a beneficial effect because higher temperatures can be supplied from the storage tank. As described earlier in the previous chapter, a higher hot water inlet temperature (T_{18}) supply increases the cooling systems' COPs. For a constant cooling load, the increasing COP is due to the decrease in the required heat input to the first-stage generator, so the increasing storage tank temperature contributes more energy to the cooling system.

Although the average sky clearness index varies between 0.51 and 0.56, the effect of a higher sky clearness index, which could happen on very clear days, has also been studied. In Figure 4.3, the effect of various sky clearness indices on the solar fraction

is shown for a given collector area of 150 m^2. The results agree with the expectation that at a higher sky clearness index, the solar radiation received by the collector increases, so the solar contribution to the energy supply increases.

So far, the study of solar-assisted absorption cooling has focused on a 20-ton cooling machine located in Ames, Iowa. For more general results, the model was also used to generalize the results for different cooling system capacities and different locations. For the following results, the collector tilt is fixed at $\beta = \phi$ - 20 toward equator, and the generation of the charts is based on latitude (ϕ) = 42.03^o N. Thus, the solar energy received will be the highest in June and July.

Figure 4.4 shows the monthly solar fraction for a constant sky clearness index, for a constant ratio of collector area (m^2) to the nominal capacity of the cooling system (ton), for various ambient temperatures. With these results, the solar fraction provided by a solar-assisted absorption cooling system located in the northern hemisphere can be predicted, provided that the average sky clearness index and the ratio of collector area to the nominal capacity of the cooling system are given. For example, suppose a 20-ton absorption cooling system is combined with 150 m^2 collector configured as indicated for the collector model in the previous section. With the sky clearness index equal to 0.7 and an average ambient temperature of 23^o C in July, the chart gives 0.38 for the solar fraction. This agrees with the results given in Figure 4.3 for the same machine and collector configuration.

Results for other sky clearness indices and ratios of collector area to nominal capacity are given in Appendix B. From these figures, it can be seen that at higher collector areas, the solar fraction increases. The solar fraction also increases if the average ambient temperature decreases. Again, this is due to a decrease in the cooling

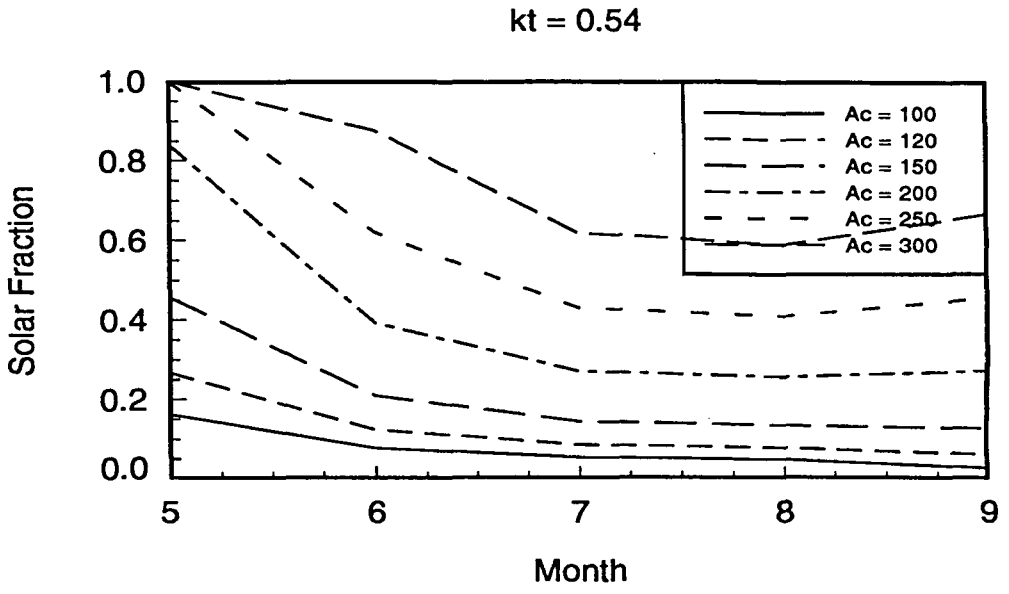

Figure 4.2: Average monthly solar fraction in supplying energy for various collector areas in Ames, Iowa.

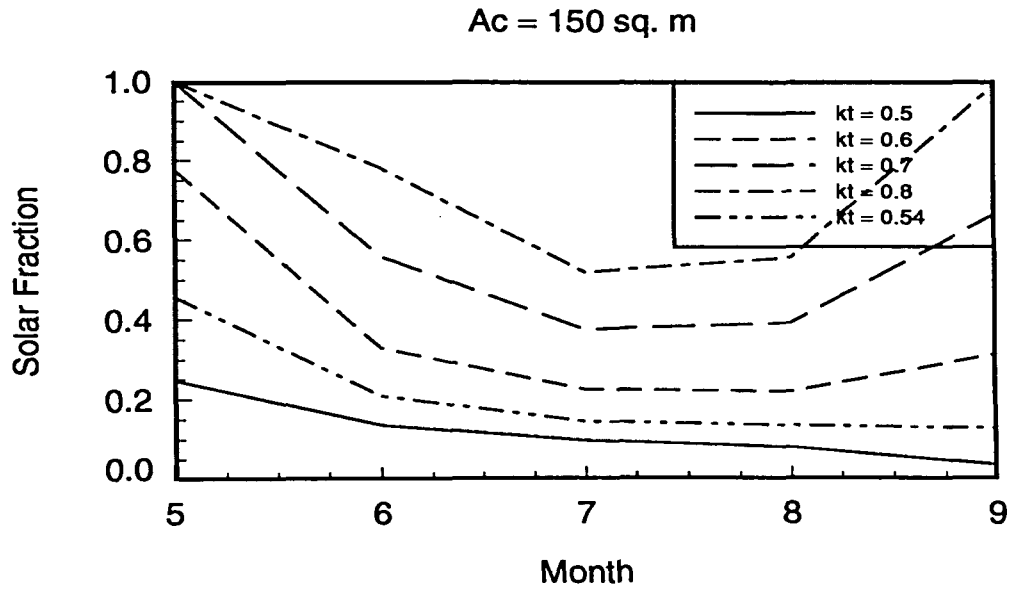

Figure 4.3: Average monthly solar fraction in supplying energy for various sky clearness indices in Ames, Iowa.

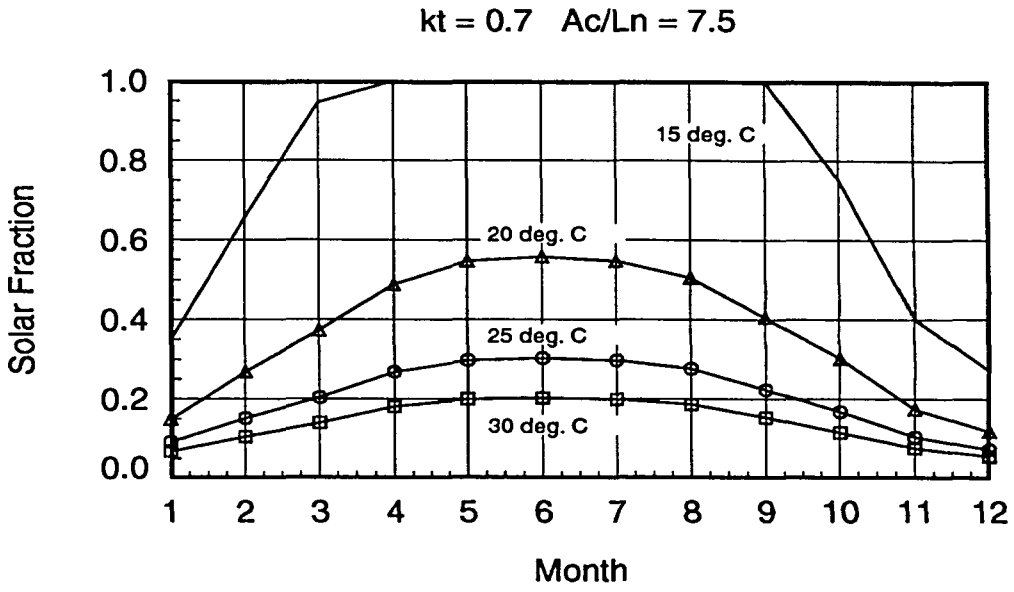

Figure 4.4: Average monthly solar fraction in supplying energy for various ambient temperature.

demand.

An application of these charts for a solar-assisted absorption cooling system located in Alburqueque, New Mexico, is shown for an average sky clearness index of 0.7. By using Figures B.13, B.14, and B.15, and the average ambient temperatures given in Table 4.2, a plot was generated. An example of the chart reading follows: In June, the monthly average ambient temperature in Alburqueque, NM, is 22^o C. For a 20-ton cooling load and 150 m^2 collector area, Figure B.14 gives approximately 0.46 for the solar fraction. For complete results, Figure 4.5 shows the solar fraction for various collector area to load ratios.

From this figure, it can be seen that larger collector areas lead to a higher solar fraction, as expected. Using these results, an economic analysis can determine the optimum configuration of combined solar-assisted absorption cooling. However,

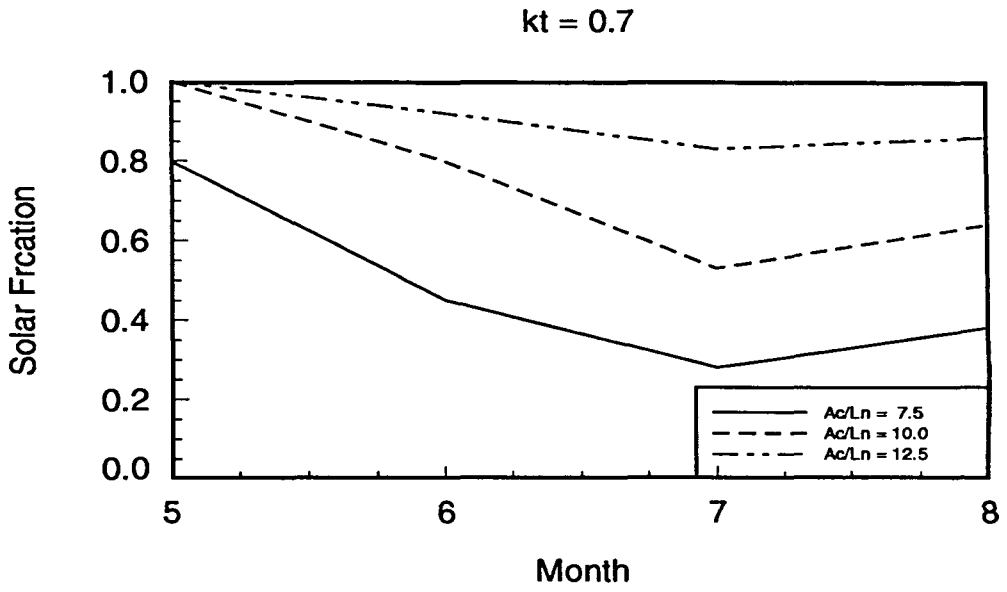

Figure 4.5: Average monthly solar fraction in supplying energy for solar cooling system located in Alburqueque, New Mexico.

due to the difference in the solar time for a different latitude, the actual available solar energy will not be the same as predicted by the charts in Appendix B, which were generated based on latitude (ϕ) = 42.03^o N. So in using the charts as given in Appendix B, a correction should be made on the result. For this purpose, a comparison study for different latitudes has been done, and a typical result can be seen in Figure 4.6.

The comparison was done for latitudes greater than 20^o N. The results show that at the time when the cooling demand is the highest, which occurs in June and July, the solar fraction does not change significantly. However, for other seasons in which the cooling demand is low, there is a slight performance difference due to latitude. Higher latitudes give lower solar fractions. But again, as these differences occur at the time when the cooling demand is low, the results as given in Appendix B might

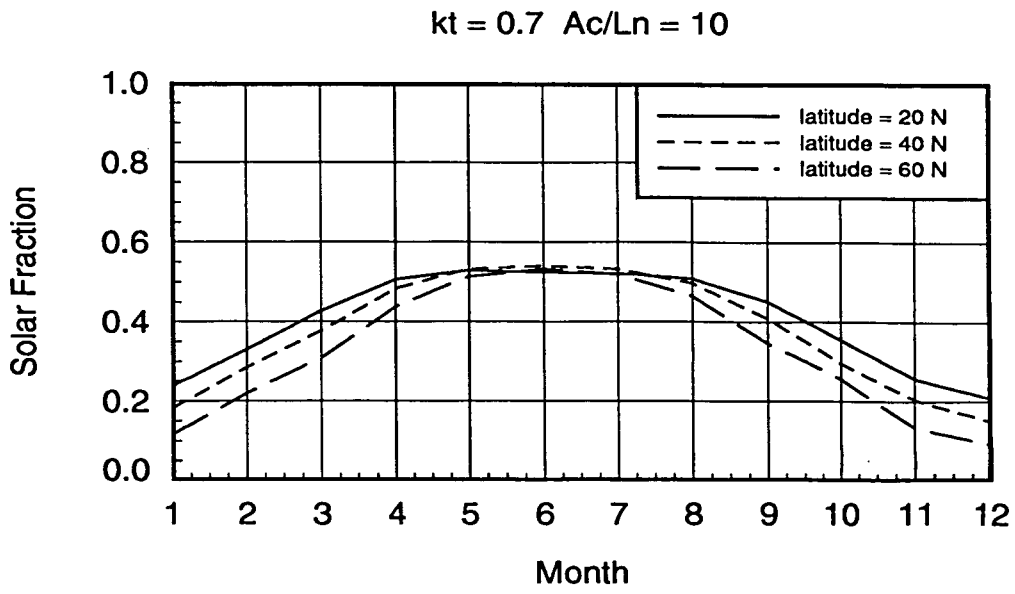

Figure 4.6: Average monthly solar fraction in supplying energy for solar cooling system located in various latitude in northern hemisphere ($\beta = \phi$ - 20). Ambient temperature = 25^o C.

be applied in predicting the solar fraction for the northern hemisphere.

For the southern hemisphere, the charts might be applied by shifting them by six months to satisfy the sign convention on latitude (ϕ) and solar declination. However, the actual results for the southern hemisphere will not be symmetrical with the results for the northern hemisphere. This is due to the fact that there is a variation of the earth-sun distance which leads to variations of extraterrestrial radiation flux in the range of 3 % [2]. This extraterrestrial radiation is the highest in December and January, and the lowest in June and July.

So far, the study of solar-assisted cooling systems has been based on the collector tilted normal to the sun when the cooling load is the highest. Basically, this configuration is intended to capture an optimum solar energy for a cooling demand which occurs only from May to September. However, in other locations, there is a

possibility that cooling demand may occur throughout the year, which means that the variation of the average ambient temperature is small. For these cases, it is recommended that the collector configuraton be arranged so the collector slope (β) is equal to the latitude where the combined collector cooling system is located. With this configuration, the collector system contributes more energy than those systems using a collector slope optimized for largest cooling demands from May to September ($\beta = \phi - 20$). The results for this configuration, which were obtained based on a latitude (ϕ) equal to 20^o N, are given in Appendix C. For the southern hemisphere, the charts should be shifted by six months.

CHAPTER 5. CONCLUSIONS

Summary

A study of several technologies available for using solar energy for cooling has been done. The results show that the energy conversion from the sun to the cooling system has an important role in a cooling system's COP. The facts show that in a vapor compression cooling system, the solar energy must go through several pieces of equipment including the solar collector and a Rankine cycle before this energy can finally be used to drive the vapor compression cooling system. On the other hand, an absorption cooling system uses only a solar collector and a generator. This causes smaller available energy losses compared with other technologies. The results of a literature survey also show that double-effect absorption cooling systems give the highest performance for using solar energy when compared with other technologies. For real application, absorption systems are also commercially available.

To further study the performance of a double-effect $LiBr/H_2O$ absorption cooling, a FORTRAN computer code has been developed. To evaluate the cooling system performance, two objective functions were established: the system performance (COP) and the system cost. The system cost is used as the objective function to determine the optimum design of the system, while the COP is used to evaluate the effects of each variable on the system performance.

A solar collector and hot water storage model were developed. An auxiliary heat exchanger was added to the collector system to supply additional energy when solar energy cannot meet the energy needs of the cooling system. The performance of the combined collector and absorption cooling system is measured by calculating the ratio of the energy supplied by the collector system to the total energy required by the cooling system to meet the cooling demand. Two types of combined collector and cooling system simulations were performed. The first simulation is the study of a solar cooling system located in Ames, Iowa. In this case, the cooling demand was evaluated based on the ambient temperature data available for Ames. To generalize the results, the second simulation was performed for various ambient temperatures, clearness indices, and collector area to load ratios throughout the year. These results allow predictions of the solar fraction for different locations and collector areas.

Conclusion

The system optimization shows that there is an economic optimum heat-transfer area for each heat exchanger. Further study shows that this is a global minimum cost of the system.

The best COPs that could be achieved by changing the heat-transfer areas and the inlet hot water temperature vary between 1.4 and 1.5. Higher COPs of approximately 1.6 were achieved if higher chilled water inlet temperatures or lower cooling water temperatures are used. These conditions are not desirable since higher chilled water inlet temperatures are not useful for cooling, and lower cooling water inlet temperatures are not usually available.

An increase in the cooling water and chilled water mass-flow rates has a beneficial

effect on the system COP. However, the impact on additional system cost should be considered in increasing these mass-flow rates, since greater pump work and capacity are required. On the other hand, for a constant cooling load, the hot water mass-flow rate does not have a significant effect on system COP because the total heat input to the first-stage generator is fixed. Increasing the hot water mass-flow rate simply decreases the temperature difference between the inlet and outlet hot water temperatures.

A review of the reversed Carnot cooling machine as shown in Figure 1.3 shows that theoretically, the COP is an increasing function of the hot water inlet temperature. However, in the actual machine, the trend shown by the reversed-Carnot cooling machine does not apply because of the limited heat-transfer effectiveness of the heat exchangers and the saturation pressure-temperature relations of the working fluids. Also, the operating temperature of the $LiBr/H_2O$ solution is limited due to crystallization.

The performance of a solar-assisted cooling system is shown as the fraction of the total heat input supplied by solar energy. This input depends mainly on the ambient temperature, the sky clearness index, and the system design. At lower ambient temperatures, higher clearness indices, and larger collector areas, the collector system contributes more energy and thus the solar fractions are higher.

Predicting the performance of a specific load of a double-effect $LiBr/H_2O$ absorption cooling system could be done by studying a real machine. This method would be very costly, so using a computer model of the cooling system is an effective way to study the performance of the system. In this study, a computer code has been developed to predict the performance of a double-effect $LiBr/H_2O$ absorption cooling

system. The Newton-Rhapson method used in simulating the system is an effective way to solve the system of equations. For the optimization, the lattice search method was effective in finding the optimal solution.

Future work related to the present study could increase the accuracy of the system model by eliminating some of the assumptions that were made. The system model could be improved by including the pressure drop along the piping, especially the pressure drop from the evaporator to the absorber. Another improvement would be to eliminate the assumption that the total heat transfer coefficients in the absorber and auxiliary heat exchangers were constant. Also, the results of the model should be compared with an actual system to validate the model. Another study could include an optimization of the combined collector and cooling systems.

BIBLIOGRAPHY

[1] *ARI Unitary Directory.* Air-Conditioning and Refrigeration Institute. Arlington, Virginia: Feb. 1990 - July 1990.

[2] Duffie A. John, William A. Beckman. *Solar Engineering of Thermal Process.* New York: John Wiley & Sons. 1991.

[3] Wilbur, P.J., and S. Karaki. *Solar Cooling.* Philadelphia, Pennsylvania: The Franklin Institute Press. 1977.

[4] McNelis, B. "Photovoltaic Refrigeration." In *Solar Air Conditioning and Refrigeration*, edited by A.A.M. Sayigh and J.C. McVeigh, Renewable Energy Series. New York: Pergamon Press. 1992.

[5] Haim, I., G. Grossman, and A. Shavit. "Simulation and Analysis of Open Cycle Absorption System for Solar Cooling." *Solar Energy* 49, no. 6 (1992): 515-534.

[6] Kaushik, S.C., S.M.B. Gadhi, R.S. Agarwal, and R. Kumani. "Modeling and Simulation Studies on Single/Double-Effect Absorption Cycle Using Water-Multi-Component Salt (MCS) Mixture." *Solar Energy* 40, no. 5 (1988): 431-441.

[7] Vliet, G.C., M.B. Lawson, and R.A. Lithgow. "Water Lithium Bromide Double-Effect Absorption Cooling Cycle Analysis." ASHRAE *Transaction* 88, part 1 (1982): 811-823.

[8] Kaushik, S.C., and S.Chandra. "Computer Modeling and Parametric Study of a Double-Effect Generation Absorption Refrigeration Cycle." *Energy Conser. Mgmt.* 25, no. 1 (1985): 9-14.

[9] Won, S.H., H.S. Chung, and H. Lee. "Simulation and Thermodynamic Design Data Study on Double-Effect Absorption Cooling Cycle Using Water-LiBr-LiSCN Mixture." *Heat Recovery System & CHP* 11, no. 2/3 (1991): 161-168.

[10] Won, S.H., and W.Y. Lee. "Thermodynamics Design Data for Double-Effect Absorption Heat Pump Systems Using Water-Lithium Chloride Cooling." *Heat Recovery System & CHP* 11, no. 1(1991): 41-48.

[11] Chinnapa, J.C.V. "Principles of Absorption Systems Machines." In *Solar Air Conditioning and Refrigeration*, edited by A.A.M. Sayigh and J.C. McVeigh, Renewable Energy Series. New York: Pergamon Press. 1992.

[12] Wilkinson, W.H. "What are the Performance Limits for Double-Effect Absorption Cycles?". ASHRAE *Transaction* 93, part 2 (1987): 2429-2441.

[13] Mills, A.F. *Heat Transfer.* Boston, Massachusets: Irwin Inc. 1992.

[14] Hou, M., and S. Tan. "Nucleate Boiling Heat Transfer of Lithium Bromide/Water Solution on a Low Finned Tube." ASHRAE *Transactions* 98, part 2 (1992): 44-50.

[15] Rohsenow, W. M. "Condensation." In *Handbook of Heat Transfer*, edited by Rohsenow, W. M. and Hartnett, J. P. New York: McGraw-Hill Book Company. 1973.

[16] Chun, K. R., and Seban, R. A. "Heat Transfer to Evaporating Liquid Film." ASME *Journal of Heat Transfer*, Nov. (1971): 391-396.

[17] Kern, D. Q. *Process Heat Transfer.* New York: McGraw-Hill Book Company. 1950.

[18] *ASHRAE Handbook - 1985 Fundamentals Volume.* American Society Of Heating, Refrigerating, and Air-Conditioning Engineers. New York: 1985.

[19] Toloukian, Y. S., S. C. Saxena, and P. Hestermans. "Viscosity." *Thermophisical Properties of Matter*, volume 11. New York (1975): 94-96.

[20] Toloukian, Y. S., and Tadashi Makita. "Specific Heat Nonmetallic Liquids and Gases." *Thermophisical Properties of Matter*, volume 6. New York (1970): 102-111.

[21] Irvine, Jr. Thomas F., and Peter, E. Liley. *Steam and Gas Tables with Computer Equations.* New York: Academic Press, Inc. 1984.

[22] Guthrie, K. M., and W. R. Grace & Co. "Capital Cost Estimating." *Chemical Engineering.* March, 24 (1969): 114-142.

[23] Local Climatological Data, Monthly Summary. National Weather Service Office. Des Moines, Iowa. 1993.

[24] Bogatykh, S. A., and I. D. Evnovich. "Investigation of Densities of LiCl, LiBr, and $CaCl_2$ Aqueous Solutions in Relation to Conditions of Gas Drying." *Journal Of Applied Chemistry of the USSR*, volume 38, no. 4. April (1965): 932-933.

[25] Bogatykh, S. A., I. D. Evnovich, and V. M. Sidorov. "Investigation of the Surface Tension of LiCl, LiBr, and $CaCl_2$ Aqueous Solutions in Relation to Conditions of Gas Drying." *Journal Of Applied Chemistry of the USSR*, volume 39, no. 11. November (1966): 2432-2433.

[26] Bogatykh, S. A., and I. D. Evnovich. "A Study of the Viscosities of Aquaeous Solutions of LiCl, LiBr, and $CaCl_2$ Applicable to the Normal Drying Gases." *Journal Of Applied Chemistry of the USSR*, volume 36, no. 8. August (1963): 1808-1809.

[27] Horvath, A. L. *Handbook of Aqueous Electrolyte Solutions.* West Sussex, England: Ellis Horwood Limited. 1985.

[28] Gael, D. Ulrich. *A Guide to Chemical Engineering Process Design and Economics.* New York: John Wiley & Sons. 1984.

[29] Lof, G.O.G. "Desiccant Systems." In *Solar Air Conditioning and Refrigeration*, edited by A.A.M. Sayigh and J.C. McVeigh, Renewable Energy Series. New York: Pergamon Press. 1992.

[30] Stoecker, W.F. *Design of Thermal Systems.* 3rd edition. New York: McGraw-Hill Book Company. 1989.

APPENDIX A. TRANSPORT PROPERTIES CORRELATION FOR $LiBr/H_2O$ SOLUTION

- **Solution densities, ρ ($1.0E^{-3}$ kg/m^3).**

  Source : Reference [24]

  Range : $35 < XW < 62$ (%)

  $25 < T < 100$ (^{o} C)

$$\rho = (R_{11} + R_{12}\,T + R_{13}\,T^2) + (R_{21}\,XW + R_{22}\,XW\,T + R_{23}\,XW\,T^2) + (R_{31}\,XW^2 + R_{32}\,XW^2\,T + R_{33}\,XW^2\,T^2) \quad \text{(A.1)}$$

where

$$\begin{aligned} R_{11} &= 1.0151947 \\ R_{12} &= .00541196137 \\ R_{13} &= -.0000420997653 \\ R_{21} &= .00511794097 \\ R_{22} &= -.000251349547 \\ R_{23} &= .00000182168288 \\ R_{31} &= .000108235093 \\ R_{32} &= .00000266595676 \\ R_{33} &= -.000000019668488 \end{aligned}$$

- **Solution surface tension, τ (N/m)**

Source : Reference [25]

Range : $35 < \mathrm{XW} < 62$ (%)

$25 < \mathrm{T} < 100$ (^{o} C)

$$\tau = \frac{(Z_1 + Z_2 + Z_3 + Z_4)}{1000} \tag{A.2}$$

where

$$\begin{aligned}
Z_1 &= Z_{11} + Z_{12}\ \ln T + Z_{13}\ \ln T^2 + Z_{14}\ \ln T^3 \\
Z_2 &= Z_{21}\ XWS + Z_{22}\ XWS\ \ln T + Z_{23}\ XWS\ \ln T^2 + \\
&\quad Z_{24}\ XWS\ \ln T^3 \\
Z_3 &= Z_{31}\ XWS^2 + Z_{32}\ XWS^2\ \ln T + Z_{33}\ XWS^2\ \ln T^2 + \\
&\quad Z_{34}\ XWS^2\ \ln T^3 \\
Z_4 &= Z_{41}\ XWS^3 + Z_{42}\ XWS^3\ \ln T + Z_{43}\ XWS^3\ \ln T^2 + \\
&\quad Z_{44}\ XWS^3\ \ln T^3
\end{aligned}$$

with

$$\begin{aligned}
Z_{11} &= -.000208260775 \\
Z_{12} &= .206753393 \\
Z_{13} &= 7.919699299999999D-03 \\
Z_{14} &= -.0000992074583 \\
Z_{21} &= 5.29098288 \\
Z_{22} &= -.0300211682 \\
Z_{23} &= -.000484816738 \\
Z_{24} &= .00000646773215 \\
Z_{31} &= -.117104709 \\
Z_{32} &= .000914744042 \\
Z_{33} &= 8.313363030000001D-06
\end{aligned}$$

$$
\begin{aligned}
Z_{34} &= -.000000132192103 \\
Z_{41} &= .000906292879 \\
Z_{42} &= -8.303325100000001D-06 \\
Z_{43} &= -.0000000370912536 \\
Z_{44} &= 8.42621864D-10
\end{aligned}
$$

- **Solution thermal conductivity, k** (W/m K)

  Source : Reference [27]

$$k = \left(\frac{k_W}{.5185}\right) k_{20}\ 1.171 \tag{A.3}$$

  where

  k_W = water conductivity (W/m k) at solution temperature

  Solution conductivity at 20^o C, k_{20} (W/m K) :

$$k_{20} = .5185 + M_L\ (-.018) \tag{A.4}$$

  Solution Molarity, M_L (1/moll) :

$$M_L = 10\ \frac{\left(\frac{\rho}{1000}\right)\ XW}{M_W} \tag{A.5}$$

  Molecular weight of LiBr, M_W (moll) :

$$M_W = 86.84 \tag{A.6}$$

- **Solution dynamic viscosity, μ** (kg/ m s)

  Source : Reference [18]

  Range : $10 < XW < 60$ (%)

  $20 < T < 100$ (^{o} C)

$$\mu = (\mu_1 + \mu_2 + \mu_3 + \mu_4) \tag{A.7}$$

where

$$\begin{aligned}
\mu_1 &= M_{11} + M_{12}\,(\ln T) + M_{13}\,(\ln T)^2 + M_{14}\,(\ln T)^3 \\
\mu_2 &= M_{21}\,(\ln XWS) + M_{22}\,(\ln XWS)\,(\ln T) + \\
&\quad M_{23}\,(\ln XWS)\,(\ln T)^2 + M_{24}\,(\ln XWS)\,(\ln T)^3 \\
\mu_3 &= M_{31}\,(\ln XWS)^2 + M_{32}\,(\ln XWS)^2\,(\ln T) + \\
&\quad M_{33}\,(\ln XWS)^2\,(\ln T)^2 + M_{34}\,(\ln XWS)^2\,(\ln T)^3 \\
\mu_4 &= M_{41}\,(\ln XWS)^3 + M_{42}\,(\ln XWS)^3\,(\ln T) + \\
&\quad M_{43}\,(\ln XWS)^3\,(\ln T)^2 + M_{44}\,(\ln XWS)^3\,(\ln T)^3
\end{aligned} \tag{A.8}$$

with

$$\begin{aligned}
M_{11} &= -5.40616818E1 \\
M_{12} &= 4.97128858 \\
M_{13} &= 1.58585842 \\
M_{14} &= -2.37442221E-1 \\
M_{21} &= 5.50244409E1 \\
M_{22} &= -4.79259739 \\
M_{23} &= -1.59504549 \\
M_{24} &= 2.19310304E-1 \\
M_{31} &= -1.81821995E1 \\
M_{32} &= 1.51866398 \\
M_{33} &= 5.11048515E-1 \\
M_{34} &= -6.90909665E-2 \\
M_{41} &= 1.98152474 \\
M_{42} &= -1.54972955E-1
\end{aligned}$$

$$M_{43} = -5.33582332E-2$$
$$M_{44} = 7.01025763E-3$$

APPENDIX B. CHARTS OF SOLAR COOLING FRACTIONS FOR VARIOUS CONFIGURATIONS WITH $\beta = \phi - 20$

On the following pages, charts of solar cooling fractions for various configurations are presented. The figures are applicable provided that the collector is specified as given in Table 4.1 and $\beta = \phi$ - 20. For each figure, the following legend applies.

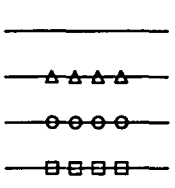

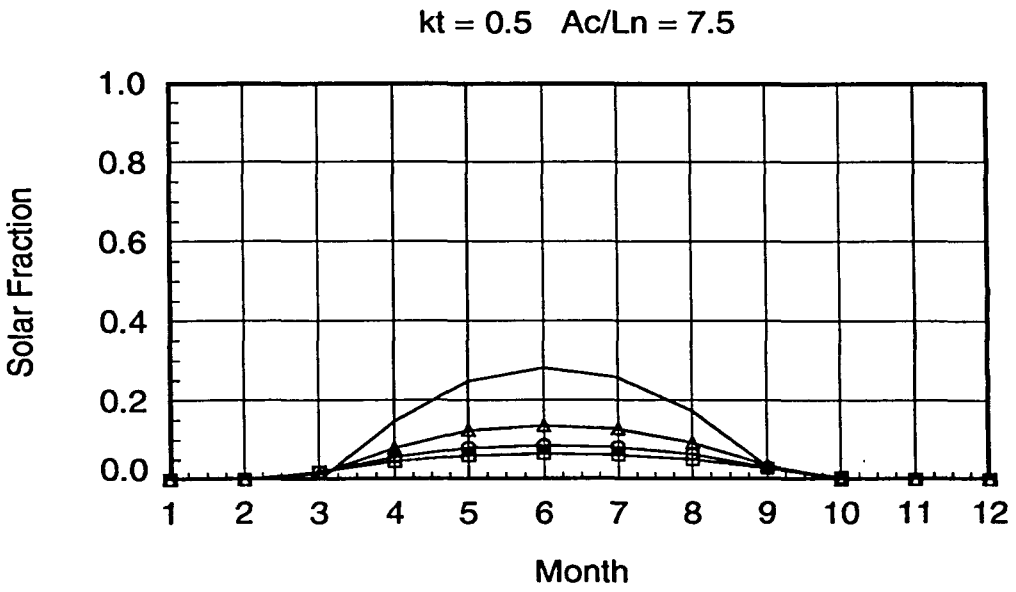

Figure B.1: Average monthly solar fraction for various ambient temperatures for kt = 0.5 and Ac/Ln = 7.5.

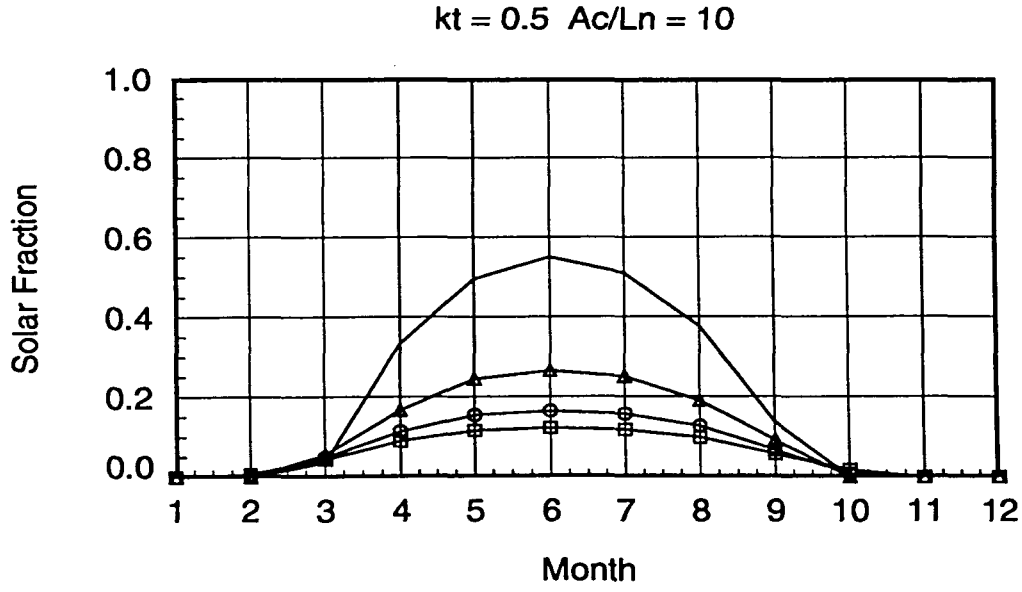

Figure B.2: Average monthly solar fraction for various ambient temperatures for kt = 0.5 and Ac/Ln = 10.

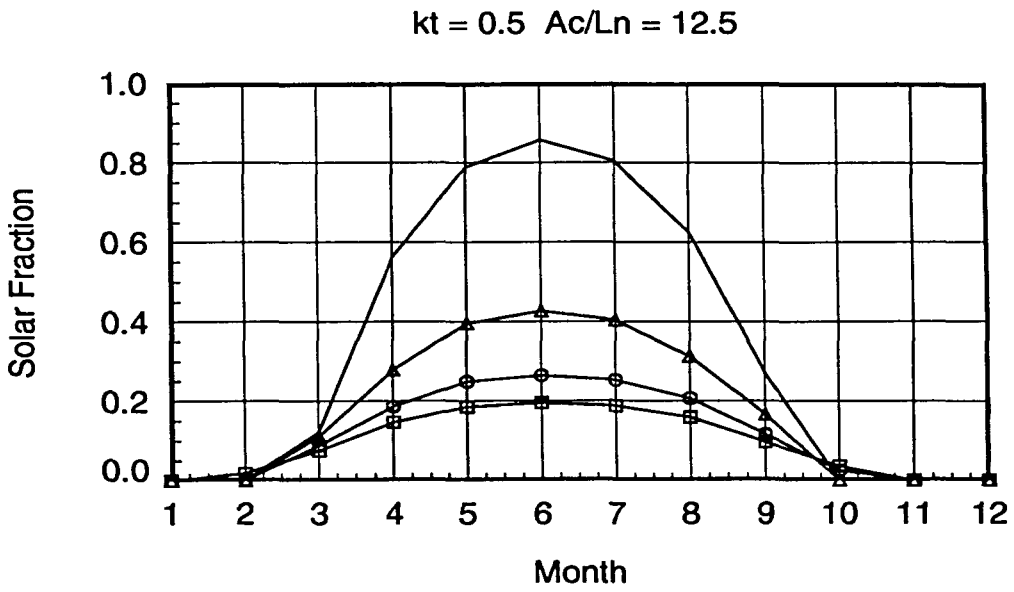

Figure B.3: Average monthly solar fraction for various ambient temperatures for kt = 0.5 and Ac/Ln = 12.5.

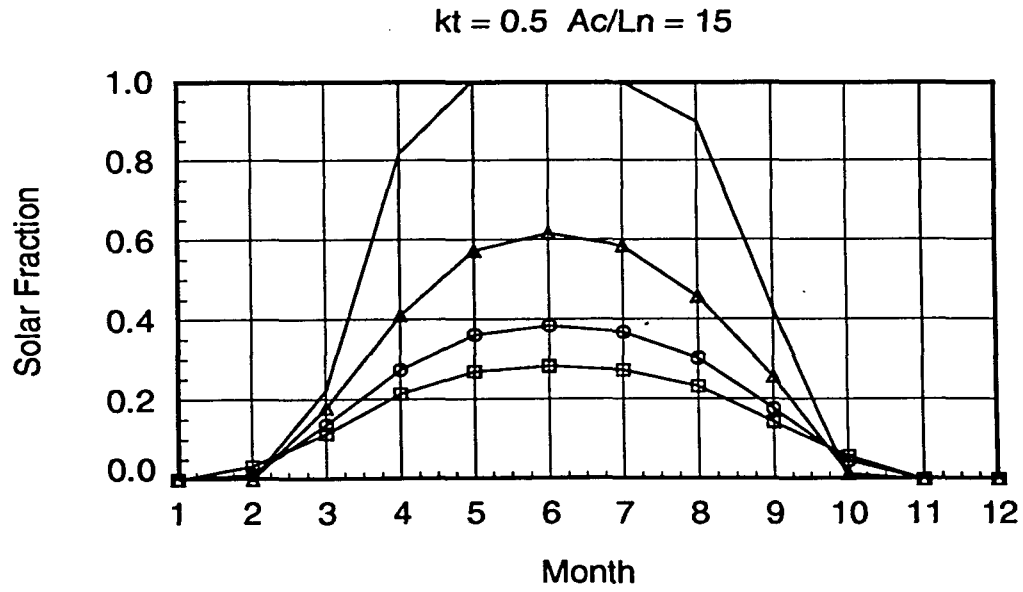

Figure B.4: Average monthly solar fraction for various ambient temperatures for kt = 0.5 and Ac/Ln = 15.

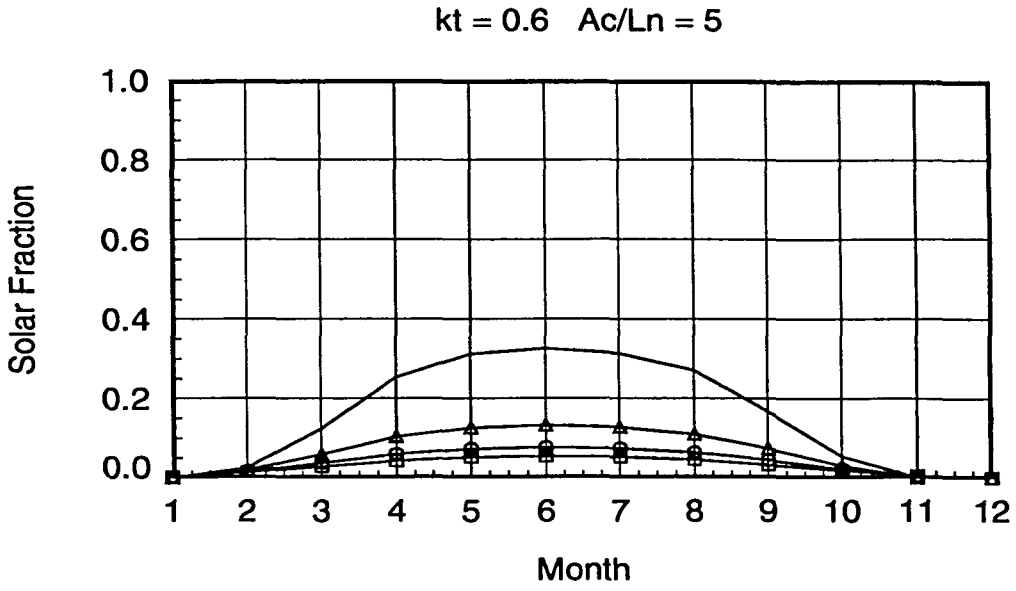

Figure B.5: Average monthly solar fraction for various ambient temperatures for kt = 0.6 and Ac/Ln = 5.

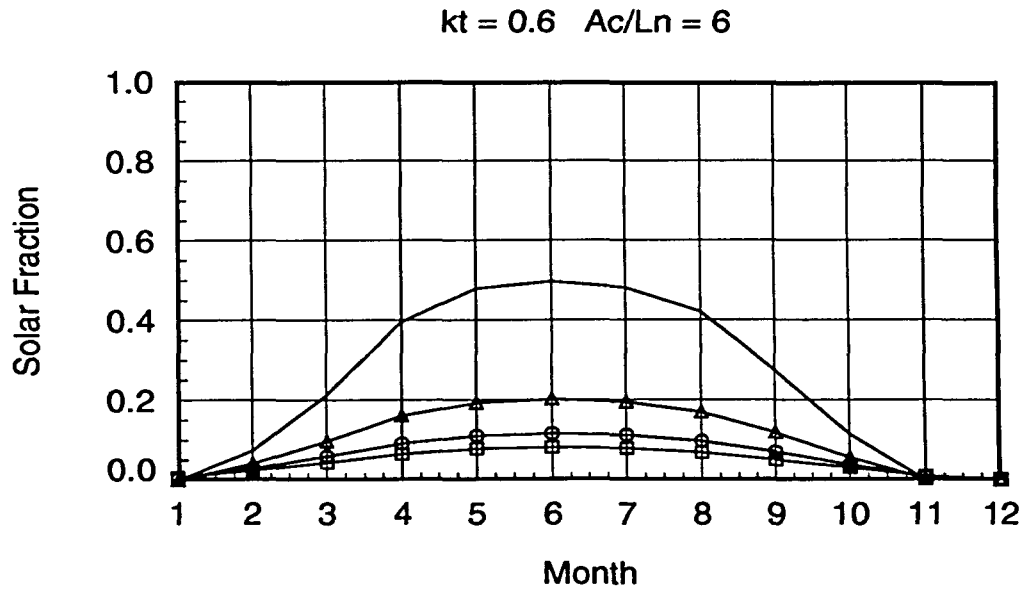

Figure B.6: Average monthly solar fraction for various ambient temperatures for kt = 0.6 and Ac/Ln = 6.

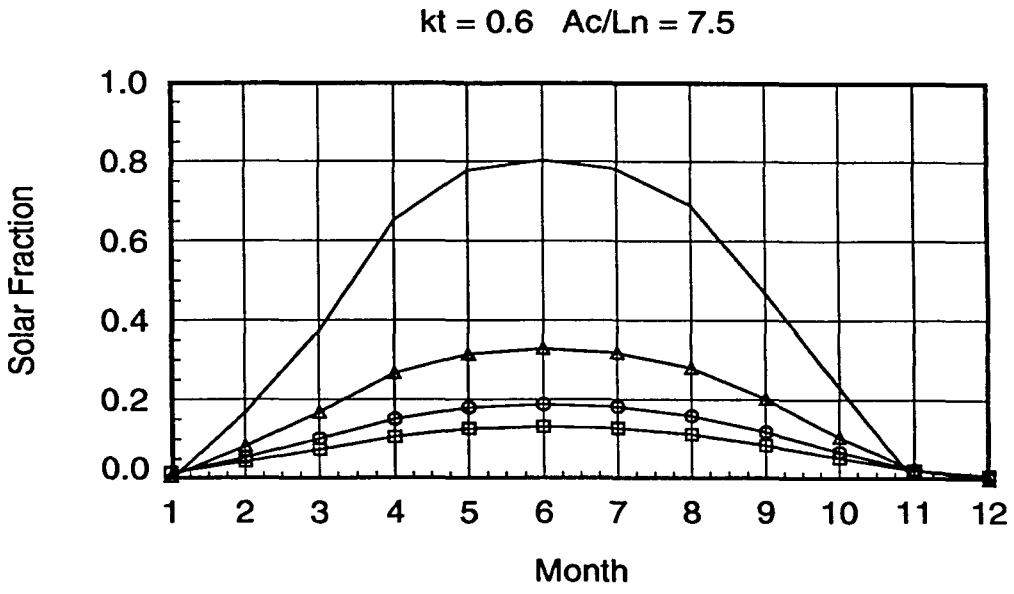

Figure B.7: Average monthly solar fraction for various ambient temperatures for kt = 0.6 and Ac/Ln = 7.5.

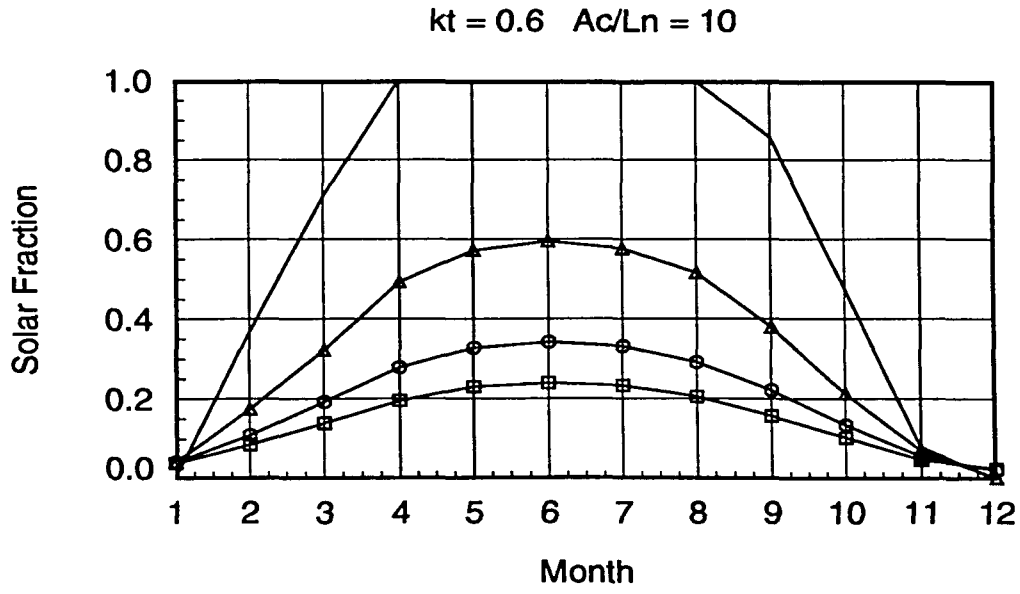

Figure B.8: Average monthly solar fraction for various ambient temperatures for kt = 0.6 and Ac/Ln = 10.

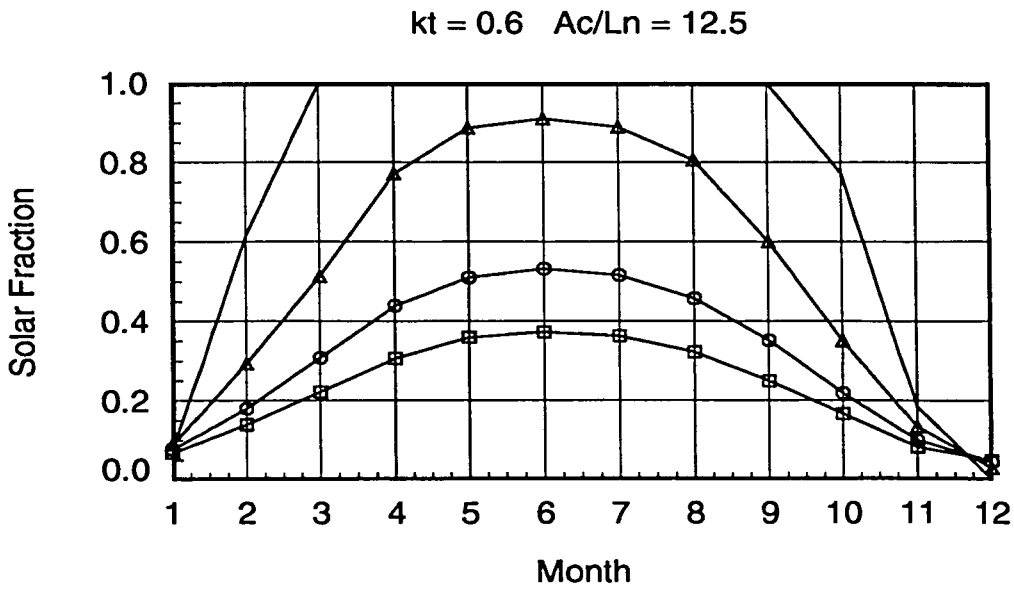

Figure B.9: Average monthly solar fraction for various ambient temperatures for kt = 0.6 and Ac/Ln = 12.5.

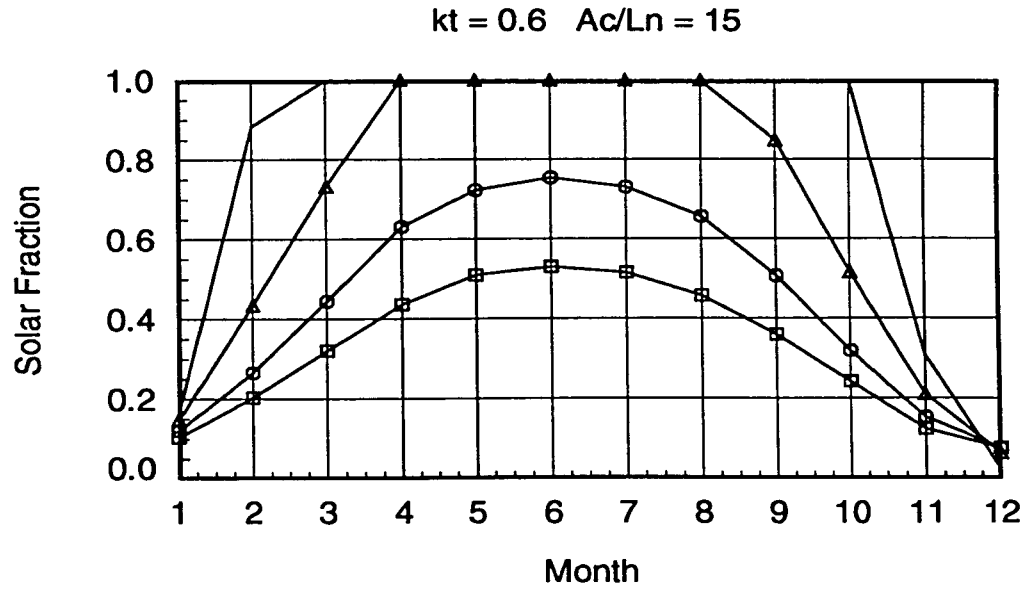

Figure B.10: Average monthly solar fraction for various ambient temperatures for kt = 0.6 and Ac/Ln = 15.

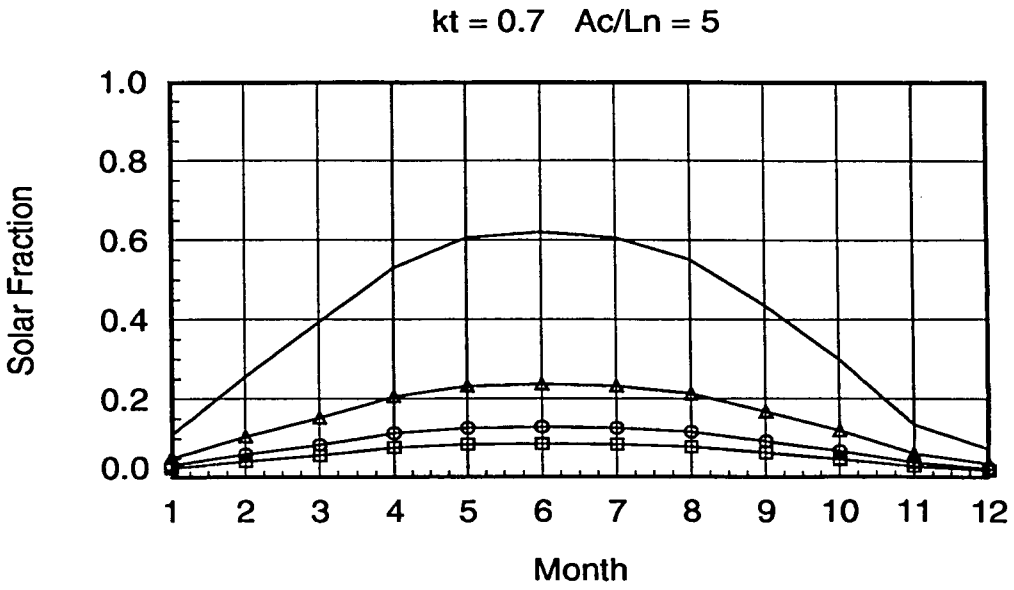

Figure B.11: Average monthly solar fraction for various ambient temperatures for kt = 0.7 and Ac/Ln = 5.

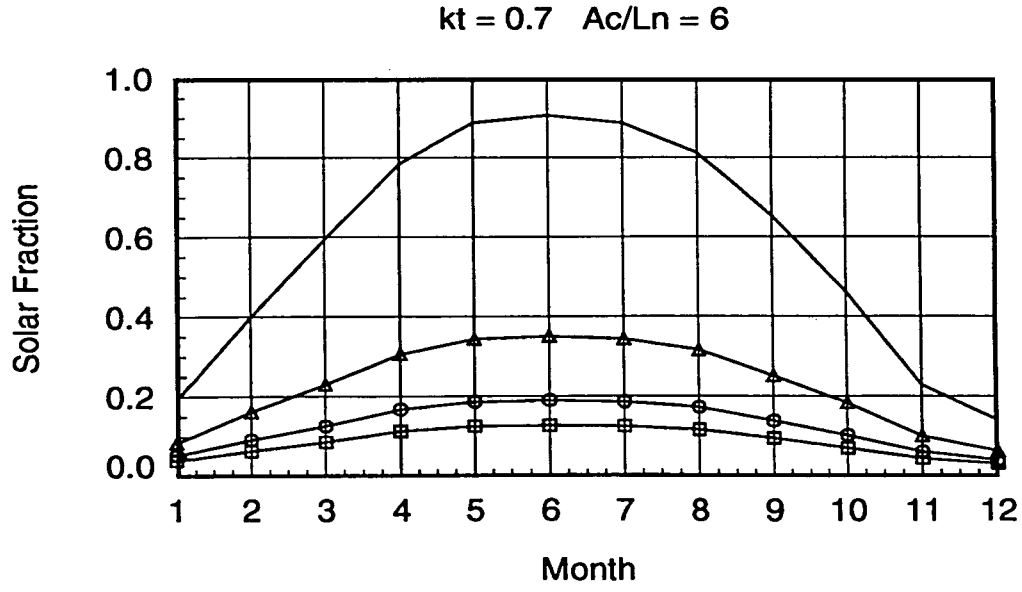

Figure B.12: Average monthly solar fraction for various ambient temperatures for kt = 0.7 and Ac/Ln = 6.

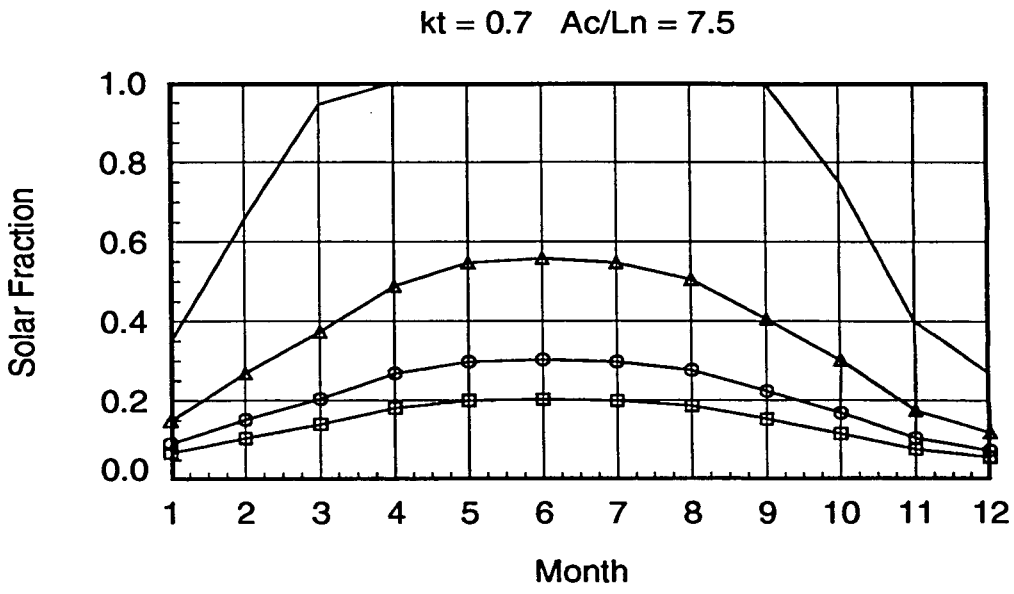

Figure B.13: Average monthly solar fraction for various ambient temperatures for kt = 0.7 and Ac/Ln = 7.5.

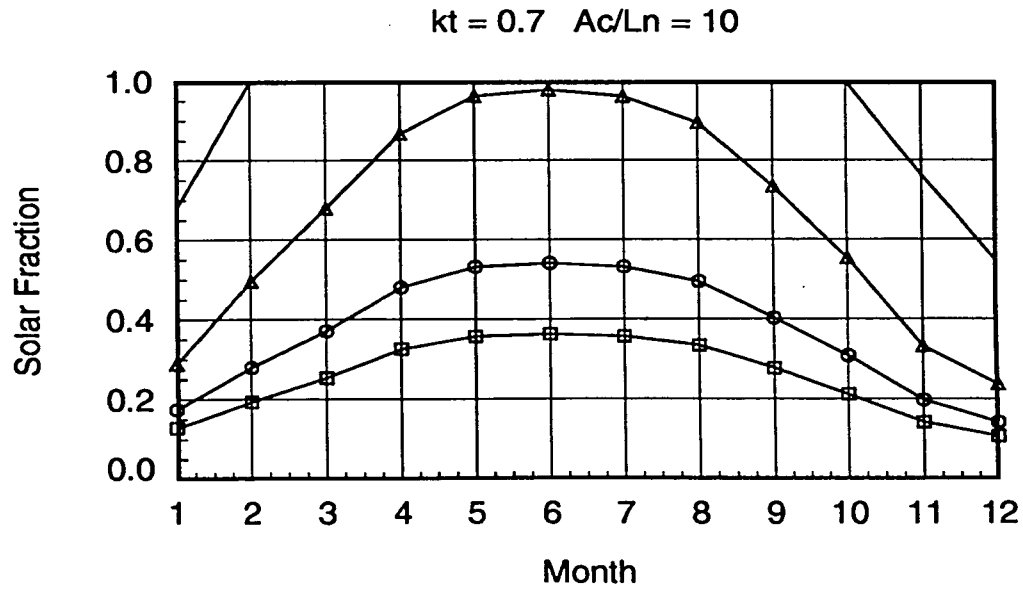

Figure B.14: Average monthly solar fraction for various ambient temperatures for kt = 0.7 and Ac/Ln = 10.

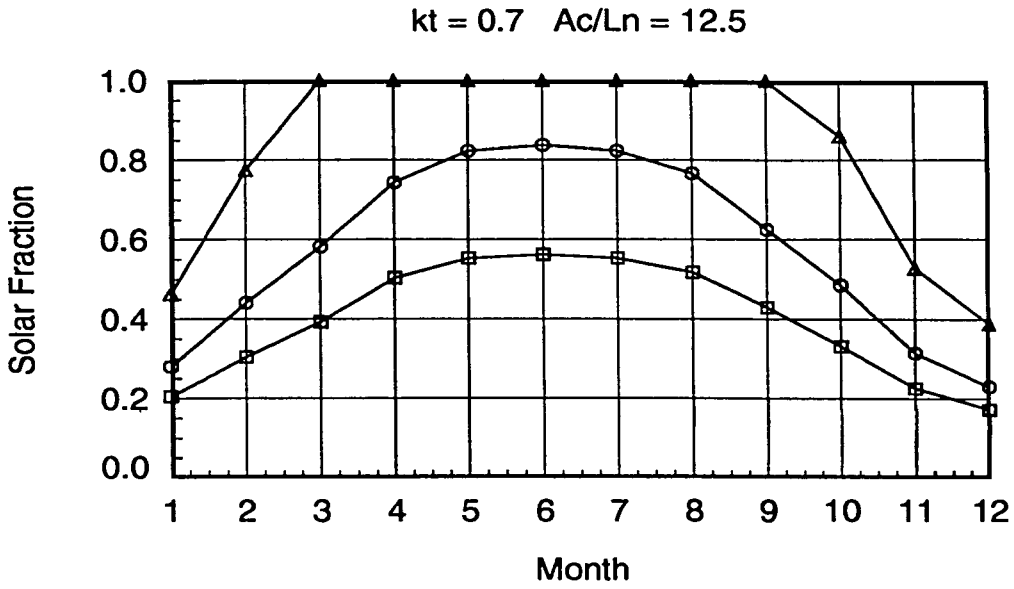

Figure B.15: Average monthly solar fraction for various ambient temperatures for kt = 0.7 and Ac/Ln = 12.5.

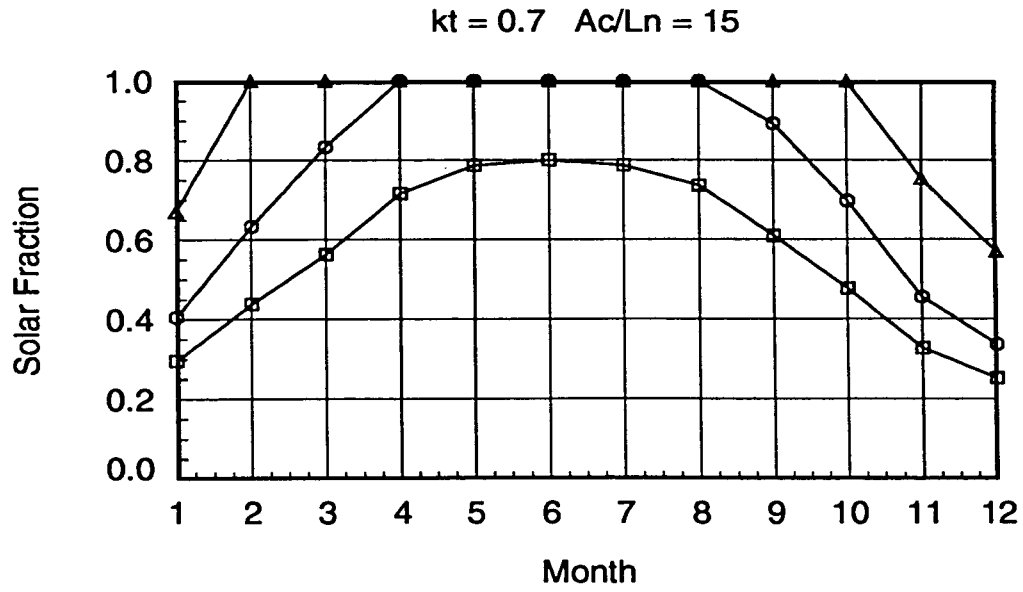

Figure B.16: Average monthly solar fraction for various ambient temperatures for kt = 0.7 and Ac/Ln = 15.

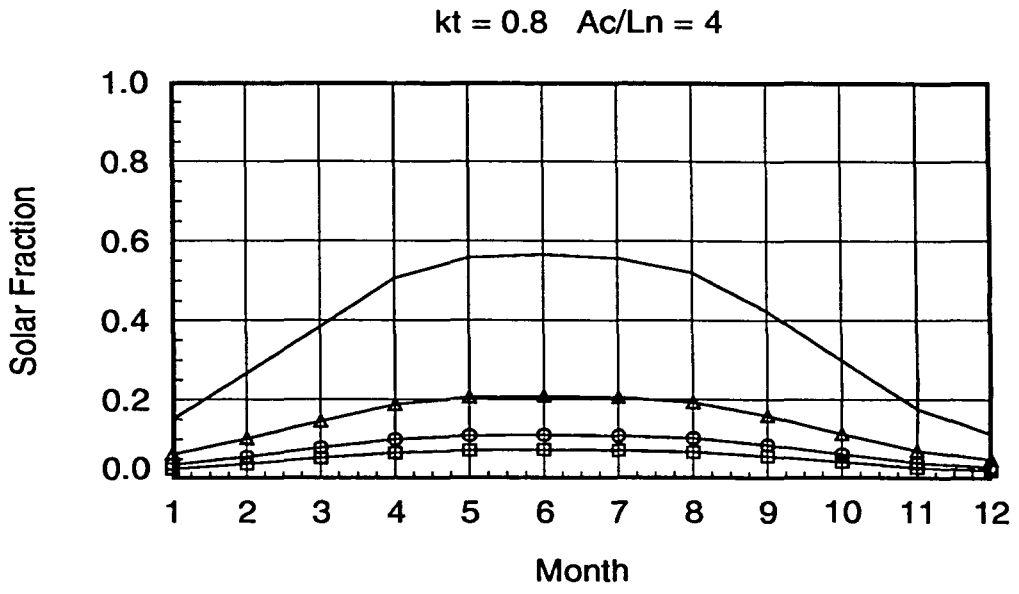

Figure B.17: Average monthly solar fraction for various ambient temperatures for kt = 0.8 and Ac/Ln = 4.

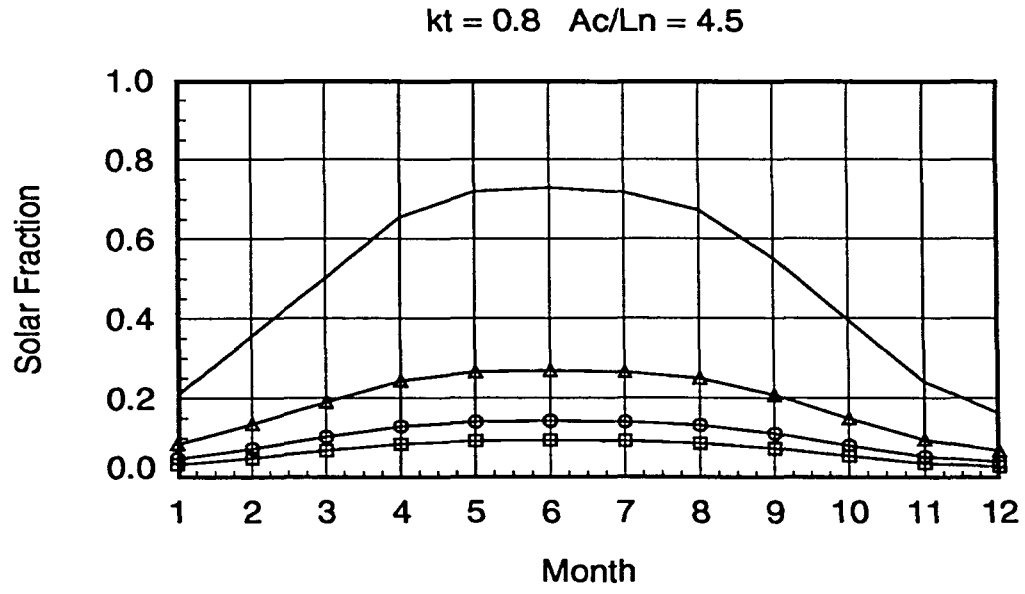

Figure B.18: Average monthly solar fraction for various ambient temperatures for kt = 0.8 and Ac/Ln = 4.5.

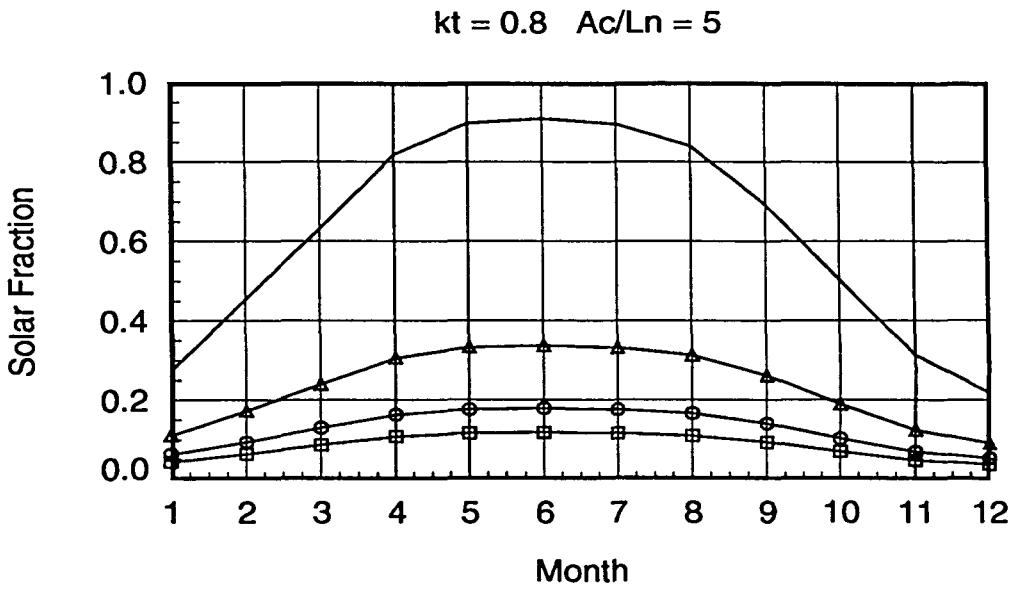

Figure B.19: Average monthly solar fraction for various ambient temperatures for kt = 0.8 and Ac/Ln = 5.

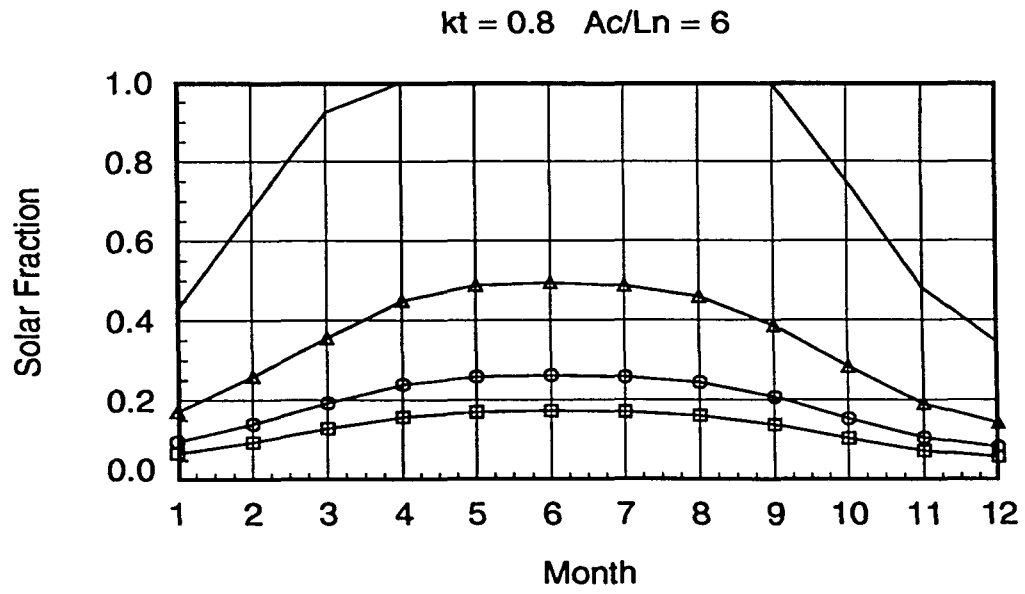

Figure B.20: Average monthly solar fraction for various ambient temperatures for kt = 0.8 and Ac/Ln = 6.

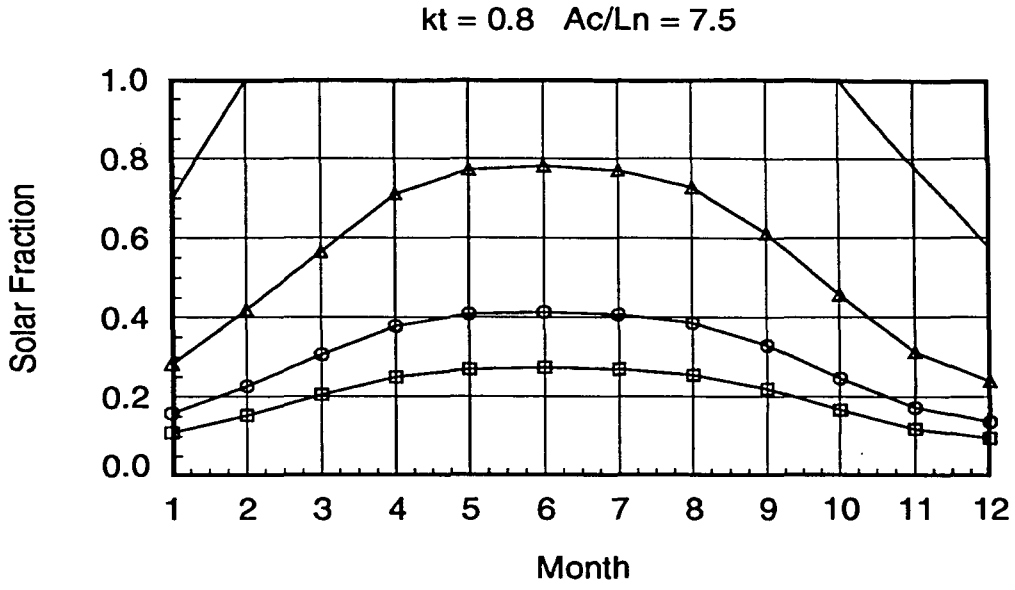

Figure B.21: Average monthly solar fraction for various ambient temperatures for kt = 0.8 and Ac/Ln = 7.5.

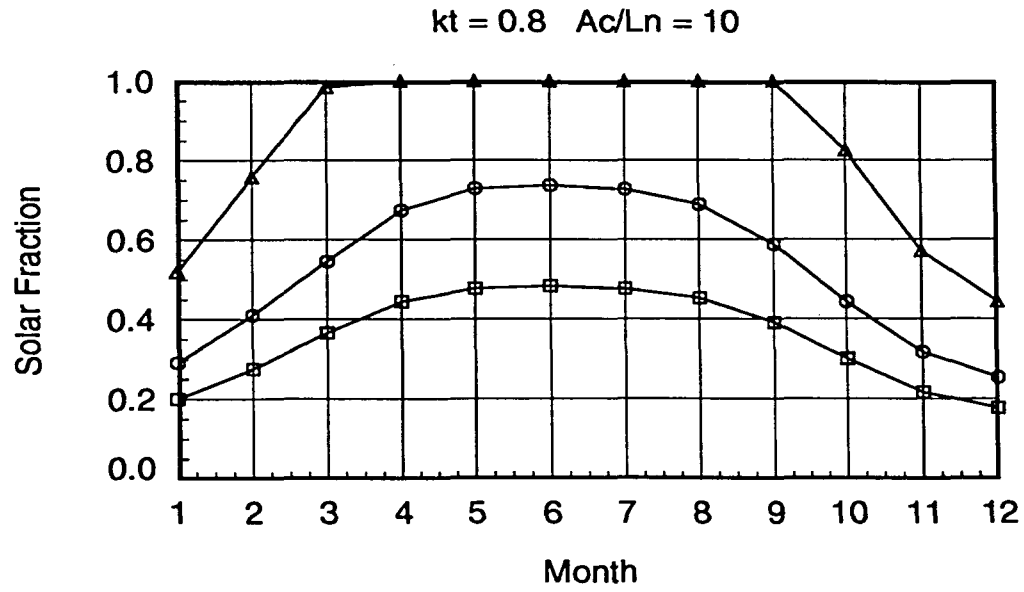

Figure B.22: Average monthly solar fraction for various ambient temperatures for kt = 0.8 and Ac/Ln = 10.

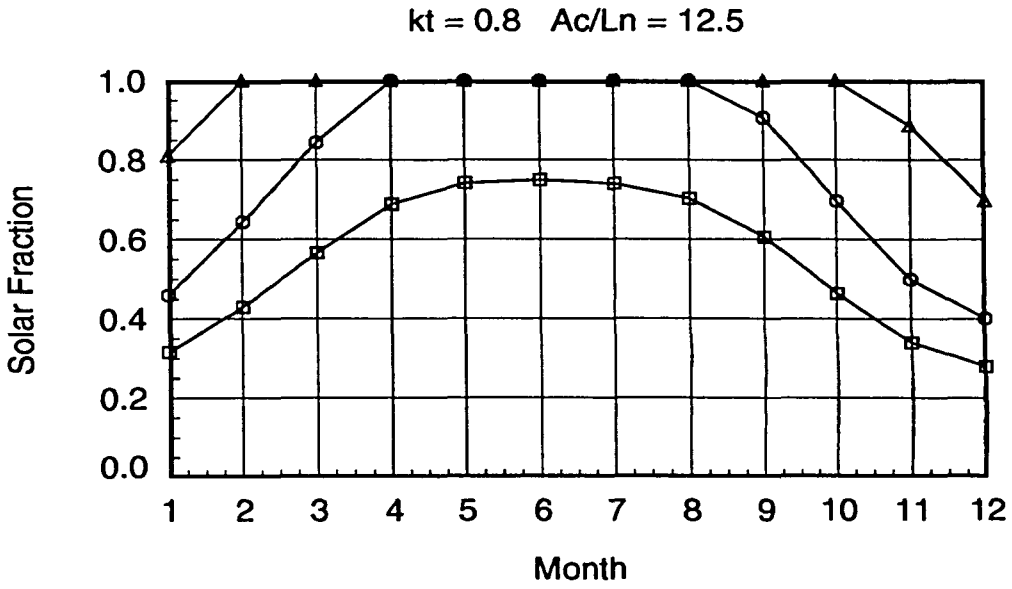

Figure B.23: Average monthly solar fraction for various ambient temperatures for kt = 0.8 and Ac/Ln = 12.5.

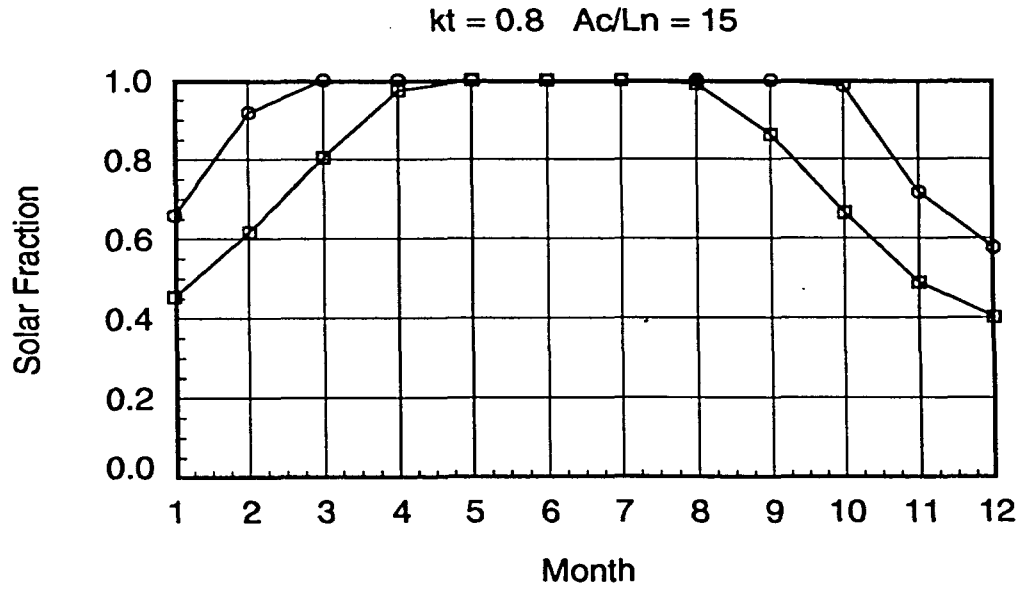

Figure B.24: Average monthly solar fraction for various ambient temperatures for kt = 0.8 and Ac/Ln = 15.

APPENDIX C. CHARTS OF SOLAR COOLING FRACTIONS FOR VARIOUS CONFIGURATIONS WITH $\beta = \phi$

On the following pages, charts of solar cooling fractions for various configurations are presented. The figures are applicable provided that the collector is specified as given in Table 4.1 and $\beta = \phi$. For each figure, the following legend applies.

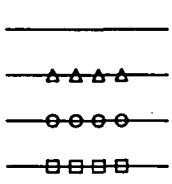

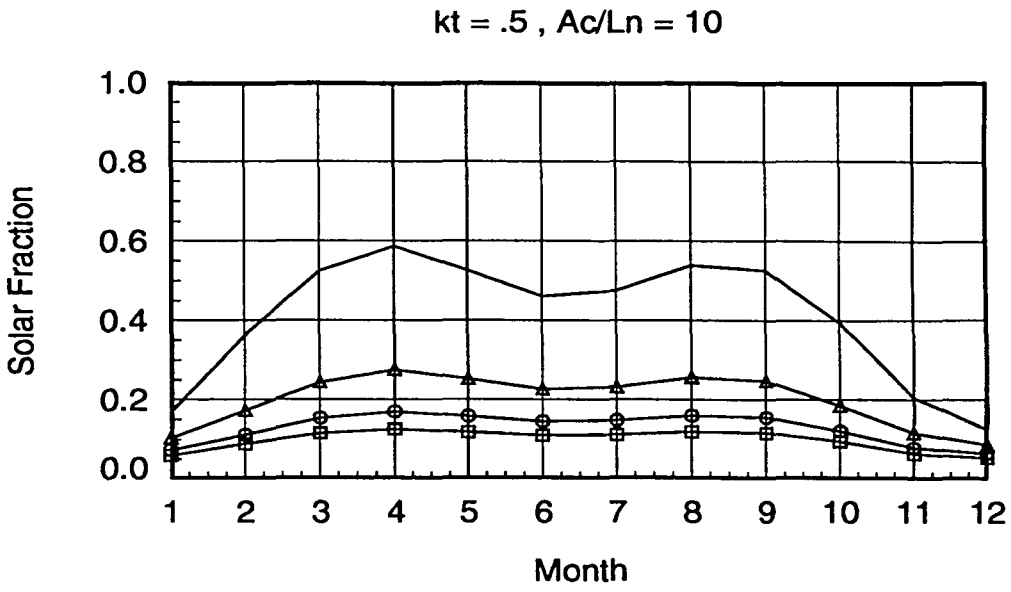

Figure C.1: Average monthly solar fraction for various ambient temperatures for kt = 0.5 and Ac/Ln = 10.

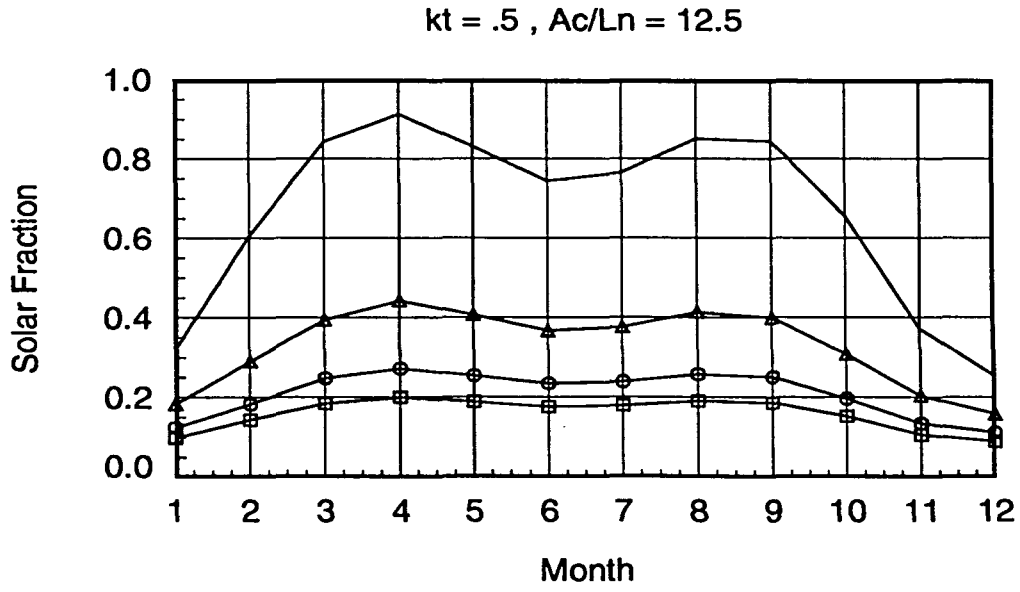

Figure C.2: Average monthly solar fraction for various ambient temperatures for kt = 0.5 and Ac/Ln = 12.5.

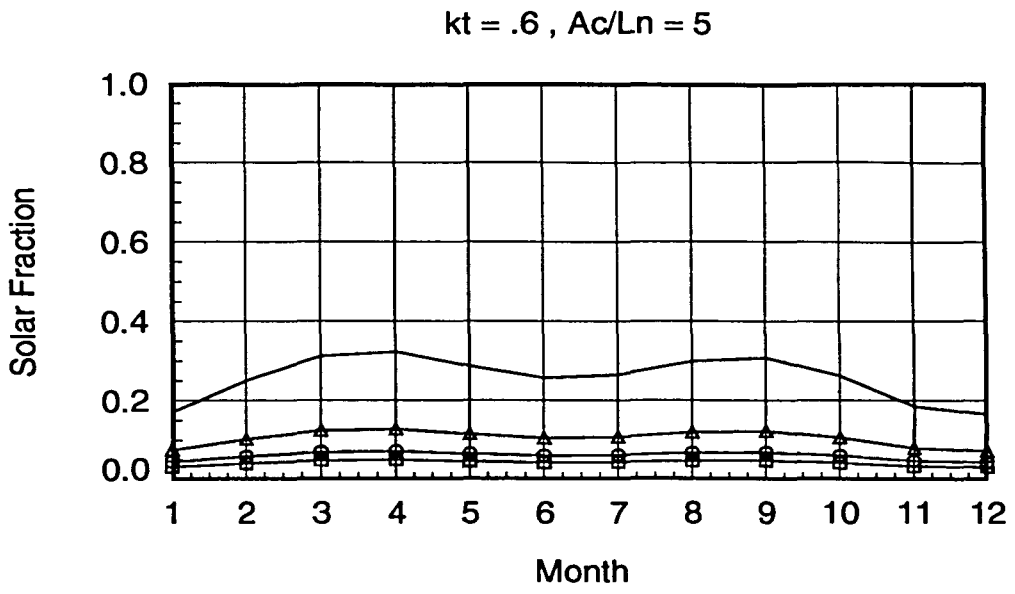

Figure C.3: Average monthly solar fraction for various ambient temperatures for kt = 0.6 and Ac/Ln = 5.

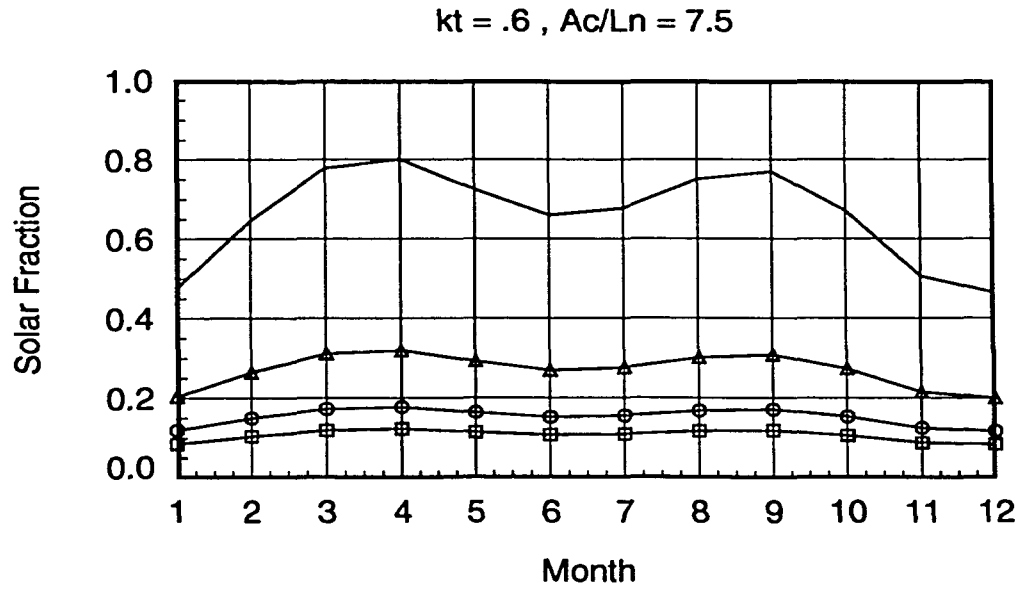

Figure C.4: Average monthly solar fraction for various ambient temperatures for kt = 0.6 and Ac/Ln = 7.5.

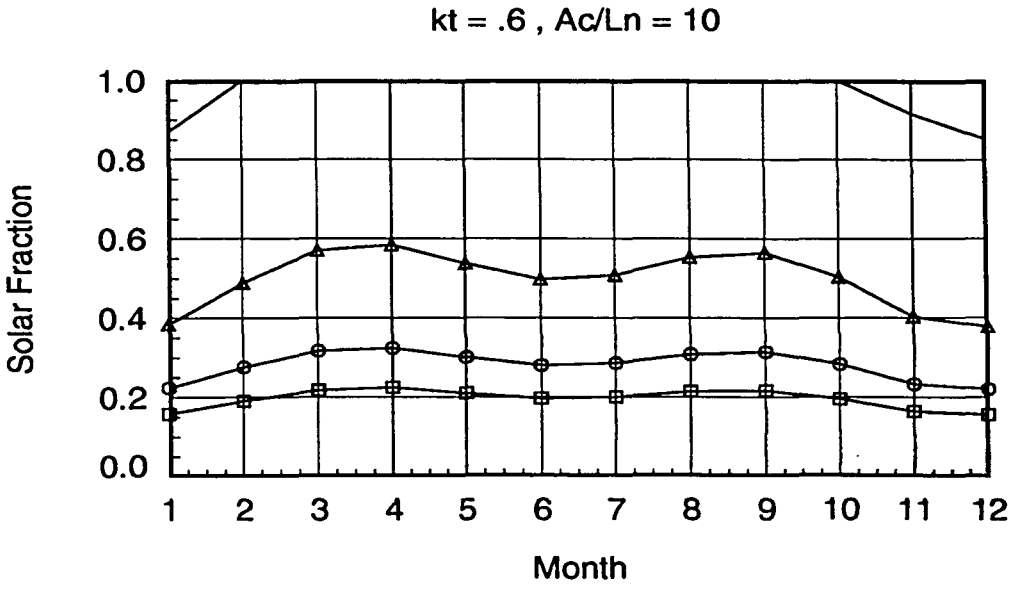

Figure C.5: Average monthly solar fraction for various ambient temperatures for kt = 0.6 and Ac/Ln = 10.

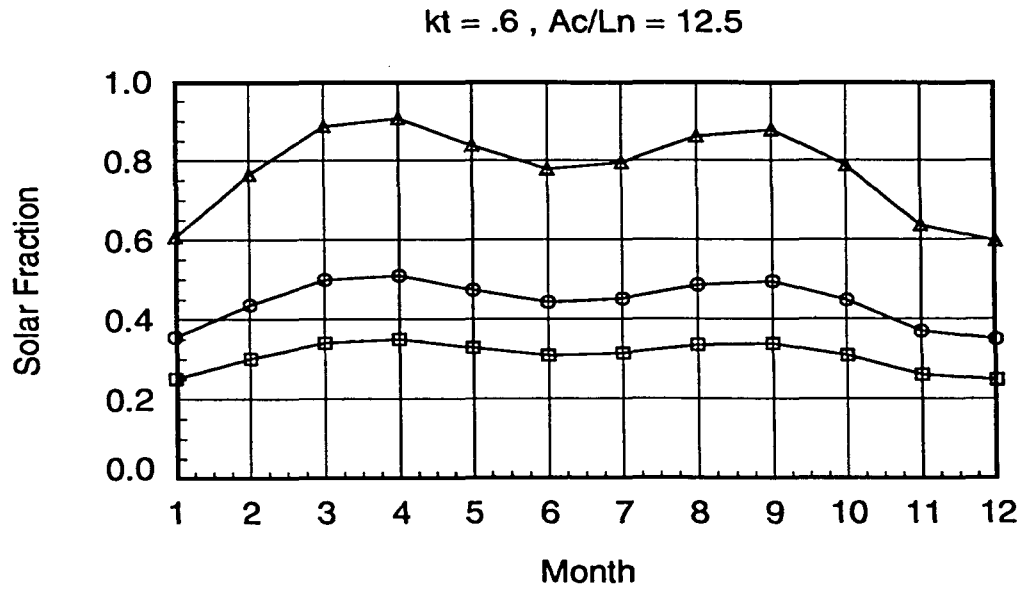

Figure C.6: Average monthly solar fraction for various ambient temperatures for kt = 0.6 and Ac/Ln = 12.5.

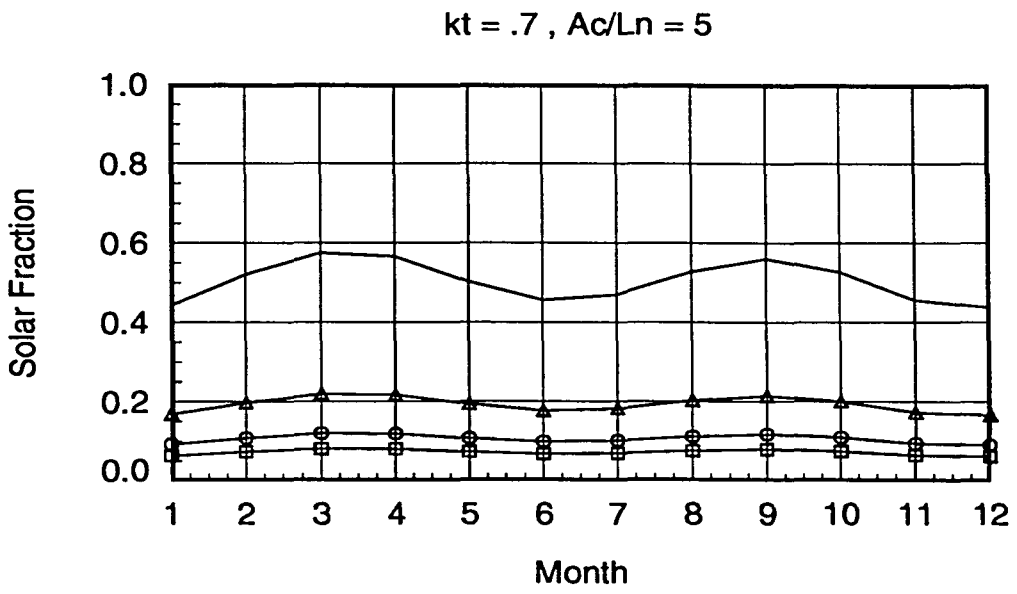

Figure C.7: Average monthly solar fraction for various ambient temperatures for kt = 0.7 and Ac/Ln = 5.

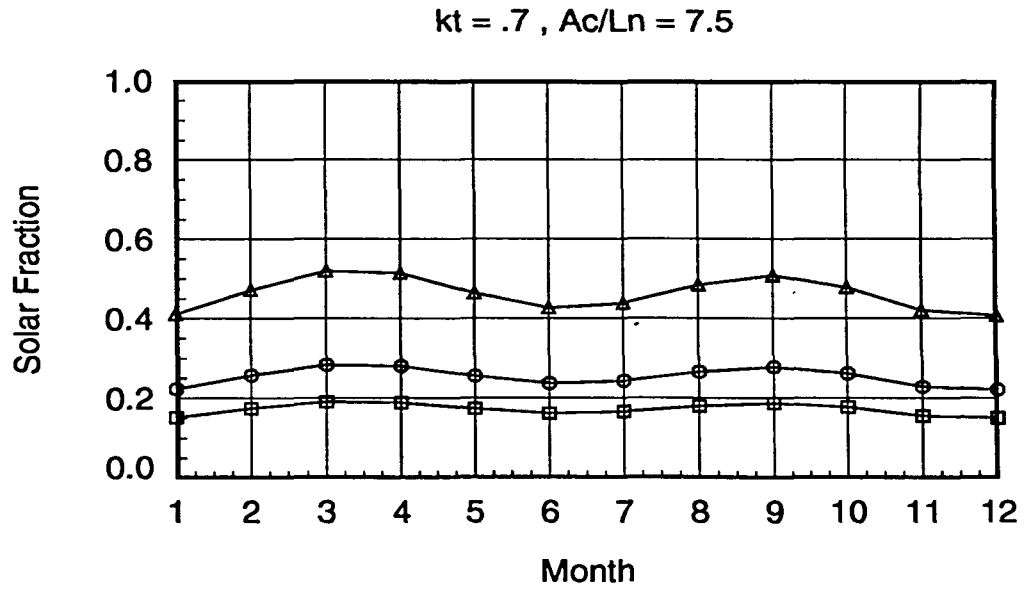

Figure C.8: Average monthly solar fraction for various ambient temperatures for kt = 0.7 and Ac/Ln = 7.5.

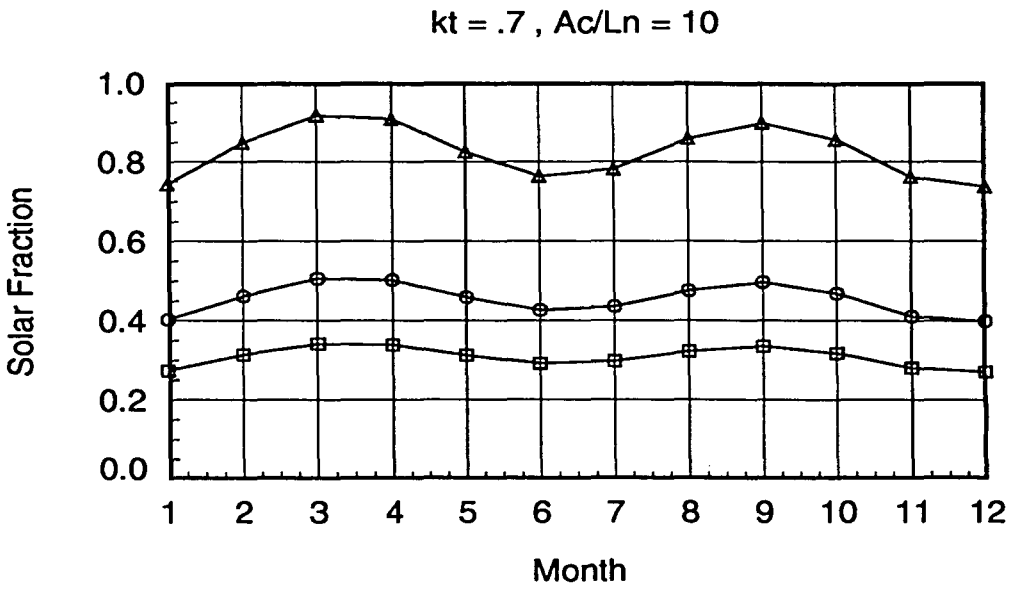

Figure C.9: Average monthly solar fraction for various ambient temperatures for kt = 0.7 and Ac/Ln = 10.

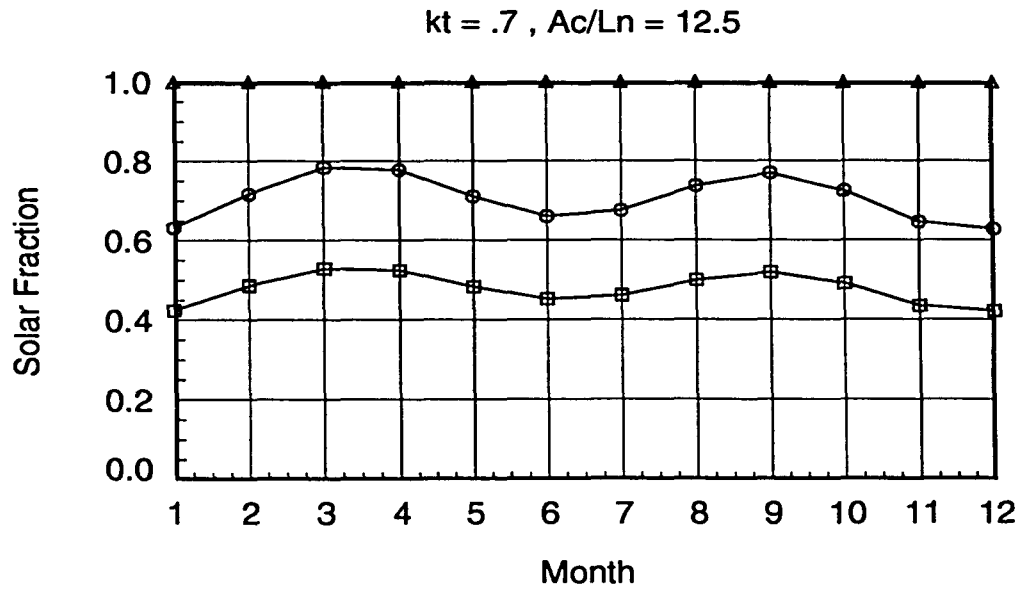

Figure C.10: Average monthly solar fraction for various ambient temperatures for kt = 0.7 and Ac/Ln = 12.5.

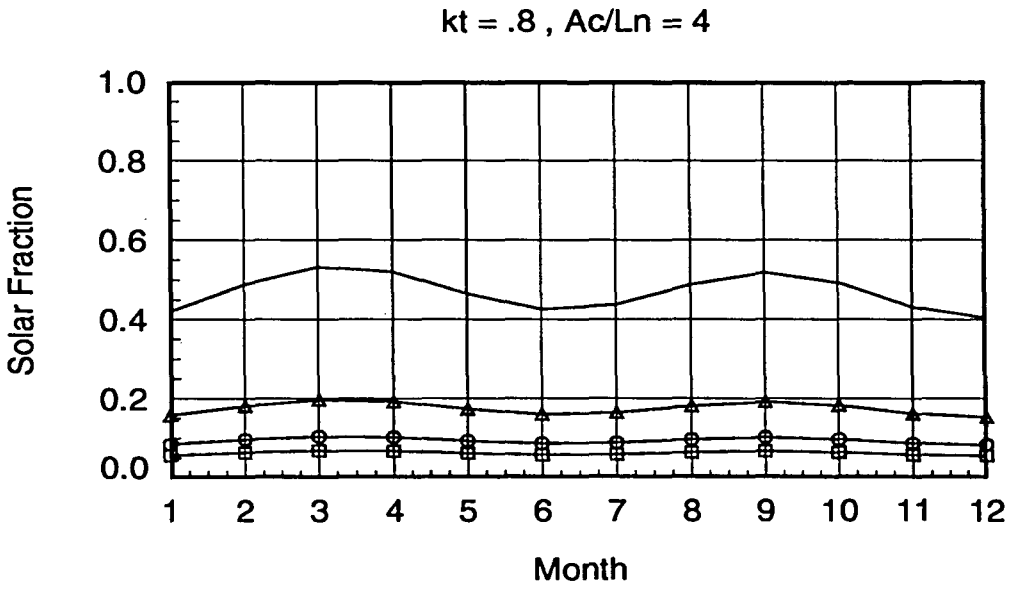

Figure C.11: Average monthly solar fraction for various ambient temperatures for kt = 0.8 and Ac/Ln = 4.

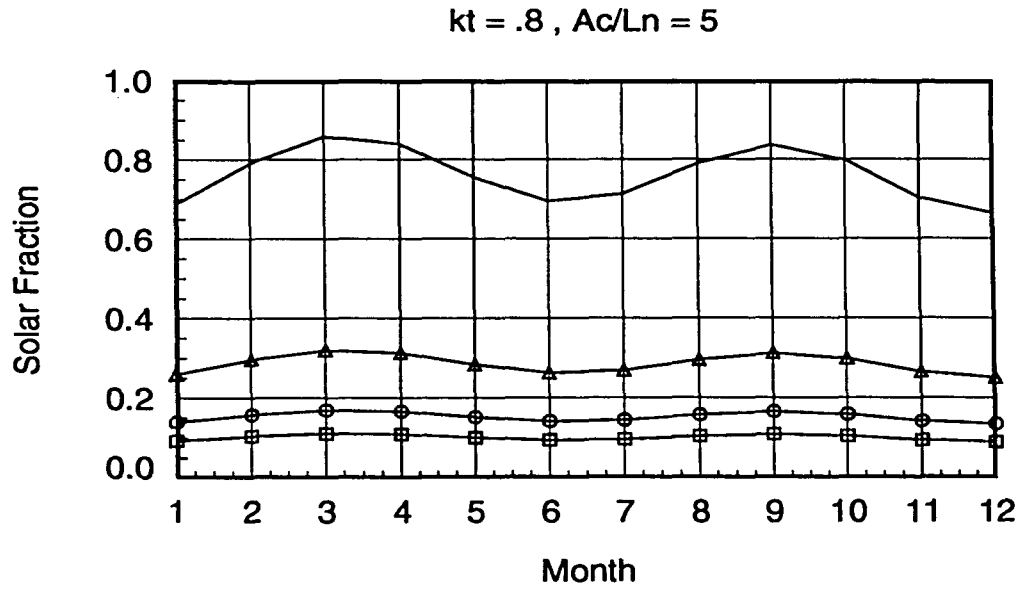

Figure C.12: Average monthly solar fraction for various ambient temperatures for kt = 0.8 and Ac/Ln = 5.

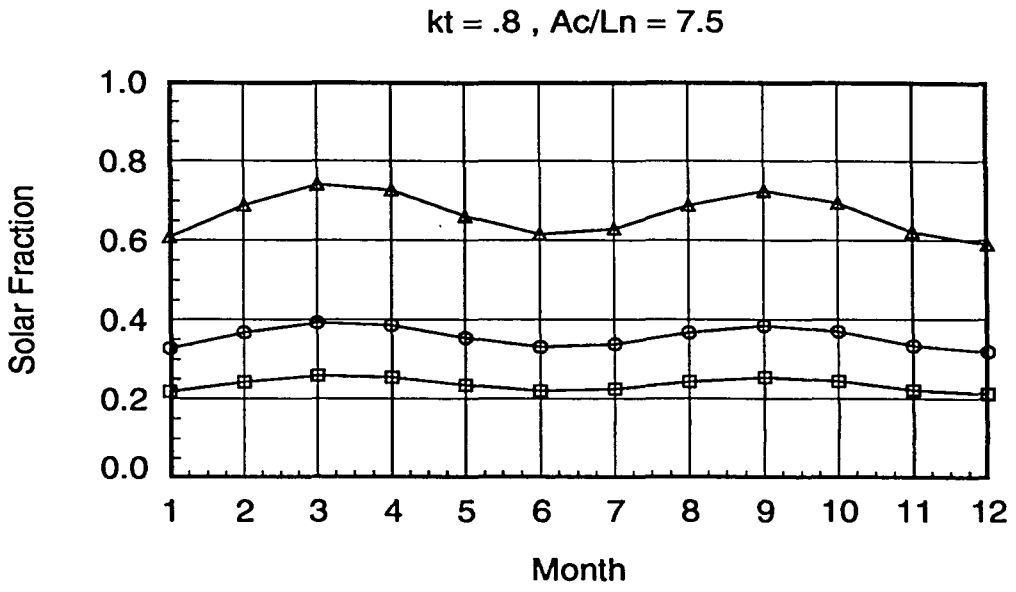

Figure C.13: Average monthly solar fraction for various ambient temperatures for kt = 0.8 and Ac/Ln = 7.5.

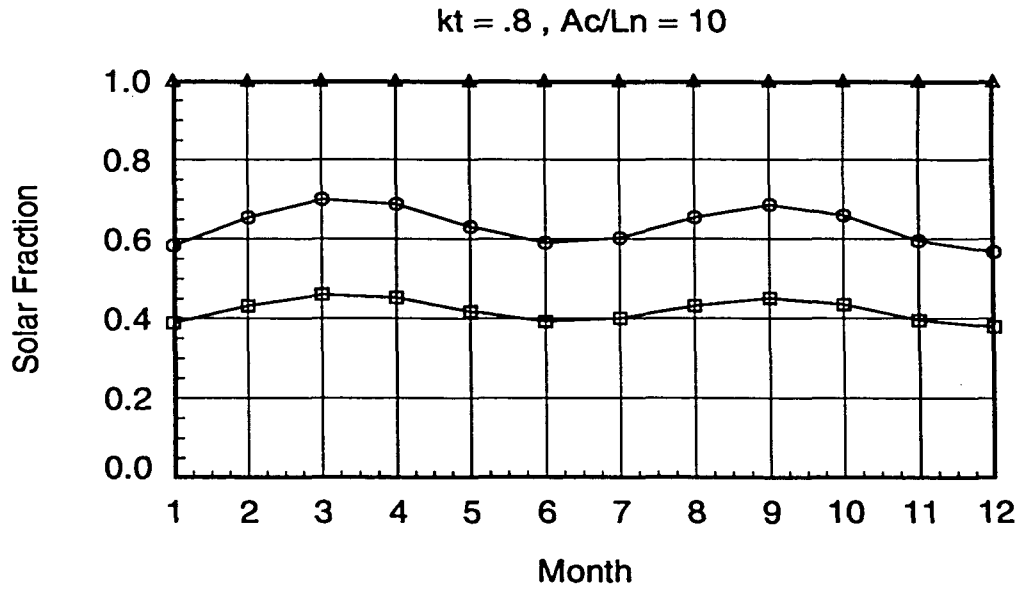

Figure C.14: Average monthly solar fraction for various ambient temperatures for kt = 0.8 and Ac/Ln = 10.

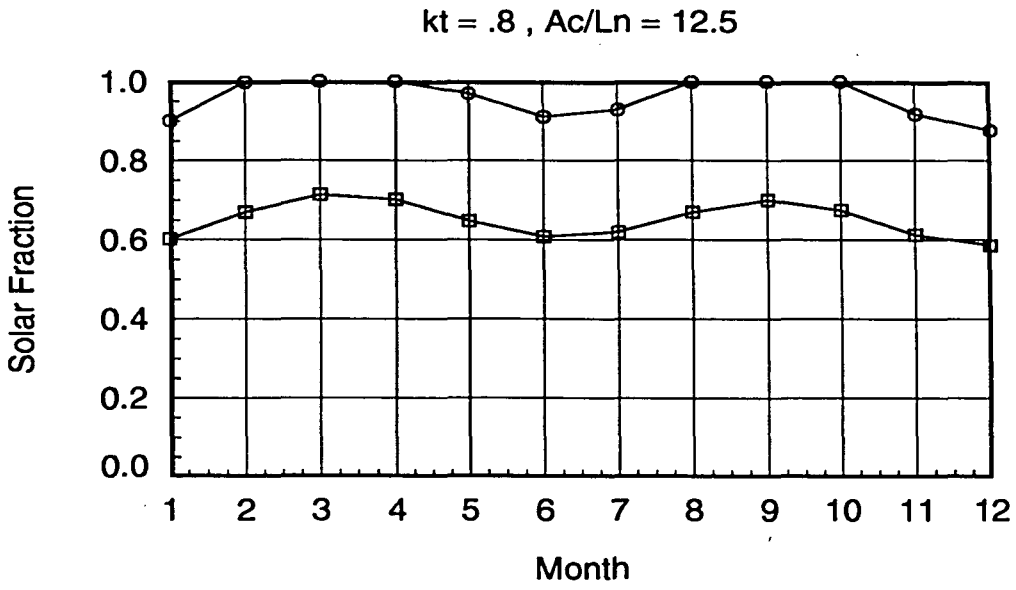

Figure C.15: Average monthly solar fraction for various ambient temperatures for kt = 0.8 and Ac/Ln = 12.5.